Scale-up of Continuous Capacitive Deionization Processes

Scale-up von Prozessen zur kontinuierlichen kapazitiven Deionisierung

Von der Fakultät für Maschinenwesen der Rheinisch-Westfälischen Technischen Hochschule Aachen zur Erlangung des akademischen Grades eines Doktors der Ingenieurwissenschaften genehmigte Dissertation

vorgelegt von

Niklas Köller

Berichter:
Univ.-Prof. Dr.-Ing. Matthias Wessling
Prof. Dr. João Paulo Serejo Goulão Crespo

Tag der mündlichen Prüfung: 16.12.2024

Diese Dissertation ist auf den Internetseiten der Universitätsbibliothek online verfügbar.

Parts of this dissertation have been published. Reproduced with permission from:

Niklas Köller, Lukas Mankertz, Selina Finger, Christian J. Linnartz, Matthias Wessling,
Towards pilot scale flow-electrode capacitive deionization, Desalination, 2023
DOI: 10.1016/j.desal.2023.117096

Niklas Köller, Dustin Roedder, Christian J. Linnartz, Mark Enders, Florian Morell, Patrick Altmeier, Matthias Wessling,
Recovery of nitrate and fluoride salts from stainless steel pickling wastewater with flow-electrode capacitive deionization, Journal of Hazardous Materials Letters, 2025
DOI: 10.1016/j.hazl.2025.100148

Niklas Köller, Mila Perrey, Lantz K. Brückner, Philipp Schäfer, Sebastian Werner, Christian J. Linnartz, Matthias Wessling,
Comparison of current collector architectures for Flow-electrode Capacitive Deionization, Desalination, 2024
DOI: 10.1016/j.desal.2024.117595

Titel: Scale-up of Continuous Capacitive Deionization Processes
Scale-up von Prozessen zur kontinuierlichen kapazitiven Deionisierung

Autor: Niklas Köller

Reihe: Aachener Verfahrenstechnik Series
AVT.CVT - Chemical Process Engineering
Volume: 51 (2025)

Herausgeber: Aachener Verfahrenstechnik
Forckenbeckstraße 51
52074 Aachen
Tel.: +49 (0)241 8095470
Fax.: +49 (0)241 8092252
E-Mail: secretary.cvt@avt.rwth-aachen.de
https://www.avt.rwth-aachen.de/AVT

Volltext verfügbar: 10.18145/RWTH-2025-02126

Acknowledgement

Die folgenden Seiten wären niemals entstanden ohne die unermüdliche Unterstützung und den Einsatz zahlreicher Menschen, denen ich im Folgenden danken möchte.

Zunächst danke ich meinem Doktorvater Prof. Matthias Wessling, für sein Vertrauen in meine Arbeit und alle Freiheiten, die ich in der Zeit an der CVT genießen durfte. Furthermore, I would like to extend my thanks to the second examiner, Prof. João Crespo, for accepting the travel to Aachen without hesitation and for the fruitful discussions during the examination. Außerdem danke ich Prof. Andert für die Leitung der Prüfungskommission.

Die Arbeit an der CVT würde niemals funktionieren ohne die Erfahrung und den tatkräftigen Einsatz von Susanne Offermann, Karin Faensen, Caroline Schmitz, Heike Zander, Sandra Gelbach, Timo Linzenmeier, Justin Gottfried, Jürgen Bougé, Joachim Schornstein, Niklas Bougé, Alexander Lehmann, Regina Hetzel, Melda Cakil, Jutta Friedrich und Sascha Gerhards. Auf ihre Unterstützung konnte ich mich immer verlassen. Susi bei der Organisation von ungefähr allem was organisiert werden musste, Karin, Timo, Justin und Sandra bei unzähligen Analysen, Niklas, Alex, Joachim und Caro bei der Fertigung von Bauteilen für ungezählt viele Membranmodule.

Diese Arbeit wäre nicht möglich gewesen ohne die vorangegangen Arbeiten, die FCDI als Technologie an unserem Lehrstuhl etabliert haben und mich für das Thema begeistert haben. Hier danke ich Alexandra Rommerskirchen und im Besonderen Christian Linnartz für seine Unterstützung und Ratschläge in den letzten mehr als sieben Jahren. Ich danke Hannah Roth für ihre Ratschläge und ihre Motivation in ihrer Zeit als Gruppenleiterin. Weitere Kolleginnen und Kollegen die mich in in den letzten Jahren begleitet haben und mir bei Rückschlägen wie bei Erfolgen zur Seite gestanden haben, waren und sind Morten Logemann, Denis Wypysek, Felix Stockmeier, Matthias Geiger, Berinike Bräsel und Florian Wiesner. Die Zeit im Büro wurde immens aufgewertet durch tolle Kolleginnen und Kollegen wie Dana Kaubitzsch, Kerstin Brökelmann, Junli Hao, Nelson Freire, Felipe Mendes, Lukas Mankertz, Valeria Günther und Christiane Sander. Fast genauso wichtig: die Mittagessen mit der Mensa-Verweigerungsgruppe im DWI, insbesondere Georg Linz, Jens Rubner, Maria Restrepo, Tobias Harhues, Wibke Zängler, Florian Neuhaus und allen anderen.

Auf der fachlichen Seite möchte ich allen Kolleginnen und Kollegen und ganz besonders den Studierenden danken, die die tollen Arbeitsatmosphäre und die Ergebnisse unseres FCDI-Teams ermöglichen. Meine Arbeit wäre im Besonderen niemals möglich gewesen ohne die Beiträge von

Paul Westerfeld, Selina Finger, Jannik Lappeßen, Dustin Roedder, Philipp Schäfer, Bia Brandt, Sebastian Werner, Leon Vahl, Jens Bettmer, Anne Stärk, Tim Haubrich, Lukas Mankertz, Margaux Benit, Lantz Kjell Brückner, Paul Scheffler, Mila Perrey, Carola Jendrzok, Alexander Borgmann, Georg Gert, Jinyang Dong, Florian Petersen, Gregor Gärtner und Simon Bussmann. Lina-Marie Dörfer, Alexandra Bucher und Lillian Büchel danke ich für den Einsatz im Rahmen ihrer Ausbildung und im Falle von Lilli auch darüber hinaus. Es hat mir immer unglaublich viel Spaß gemacht mit euch allen zusammen zu arbeiten. Paul, Lukas und Georg wünsche ich bei ihren Promotionen an der CVT viel Erfolg und genauso starke Unterstützung wie ich sie von ihnen erfahren durfte.

Ich glaube, dass die Arbeitsumgebung an einem Lehrstuhl immer besonders ist, aber es ist trotzdem nicht selbstverständlich dass sich ein solches "Biotop" herausbildet wie an der CVT: ein toller Haufen von bereits genannten und noch mehr ungenannten Menschen, die mich Willkommen geheißen haben und immer wieder ein Gefühl von "Zuhause" gegeben haben. Ich werde euch vermissen, wenn die Reise weiter geht! Ich bin dankbar für die vielen Aktivitäten meist sportlicher Natur, die ich mit Kolleginnen und Kollegen ausüben konnte. Besonders danken möchte ich an dieser Stelle Maria Padligur und meiner Nachbarin/Trainingsparterin/Motivatorin Kristina Baitalow, die nicht nur den Arbeitsalltag lustiger gestaltet haben.

Die letzten Jahre waren manchmal (zu) intensiv, für den dringend benötigen Abstand und den mentalen Support durch Sport, Gespräche, gemeinsames Kochen, Konzertbesuche, Urlaube und vieles mehr danke ich Björn Singelmann, Kirsten Rinke, Ralf Kottenstedde, Jules und Sevinç Genç, Lars und Rahel Heesemann, Larissa Laurini und Lucas Stüwe.

Meiner Familie danke ich ein unglaublich liebevolles Umfeld und für unbedingte Unterstützung in allem was da kam und kommt. Ohne euch wäre auch das hier nicht möglich gewesen. Zum Schluss: Selina, vielen Dank für deinen Rat, deine Geduld und deine Unterstützung.

I have never tried that before,
so I think I should definitely be able to do that.

- Pippi Longstocking, Astrid Lindgren

Contents

Abstract

Clean water, a fundamental human right, remains unattainable in many regions due to scarcity exacerbated by growing populations and climate change. Innovative technologies are required to extract potable water from saline sources and reclaim wastewater from industrial or agricultural processes. Removal of salt ions necessitates energy-intensive approaches. Therefore, developing novel, energy-efficient desalination and salt recycling techniques is imperative. Among these techniques, electrically-driven Flow-electrode Capacitive Deionization (FCDI) stands out due to its continuous operation and energy efficiency, particularly in treating low-salinity feed water.

Despite promising results from laboratory-scale studies using mostly synthetic salt solutions, there has been a critical need to validate the technology's efficacy at larger scales and with real-world feed solutions.

This thesis undertook the scale-up of FCDI technology and deployed it in real-world desalination and salt recycling scenarios while innovating new components and materials to enhance cost-effectiveness. Scale-up involved experiments with various module configurations and current collector architectures. In these experiments, the concentrations of the produced solutions were quantified and used as performance metrics.

A central outcome of this thesis was the development of a stacking concept for FCDI modules at the pilot scale. The concept was evaluated against an established electrically driven desalination technology (Electrodialysis). The specific desalination performance of FCDI modules at the pilot scale was lower than at the laboratory scale, indicating potential for future optimization. Compared to Electrodialysis, FCDI requires more membrane area, resulting in a disadvantage in capital cost. A new current collector architecture was established to reduce the cost of FCDI modules. Finally, a wire mesh sensor was developed, which could be used to investigate and improve FCDI in the future.

The practical application of FCDI in real-world water treatment tasks is crucial for advancing the technology. Only through such applications can the merits and shortcomings of FCDI be understood comprehensively - leading to iterative improvements of the technology. Scale-up is the most crucial step in enabling real-world applications. This thesis provides a roadmap and takes the first steps towards industrial application. Future research should focus on scale-up with novel module concepts and identification of new applications for FCDI.

Zusammenfassung

Sicherer Zugang zu sauberem Trinkwasser, einem menschlichen Grundrecht, ist in vielen Regionen nach wie vor unmöglich. Wasserknappheit und Verteilungsprobleme verschärfen sich durch Bevölkerungswachstum und die Folgen des Klimawandels. Angesichts dieser Herausforderung sind innovative Technologien erforderlich, um Trinkwasser aus Salzwasser zu gewinnen und Abwässer aus industriellen oder landwirtschaftlichen Prozessen aufzubereiten. Die kapazitive Deionisierung mit Fließelektroden (FCDI) als elektrisch getriebenes Verfahren zeichnet sich durch einen kontinuierlichen Betrieb und eine hohe Energieeffizienz aus, insbesondere bei der Behandlung von Wässern mit niedrigem Salzgehalt.

Studien zu FCDI im Labormaßstab zeigen das Potential der Technologie. Zumeist wurden synthetische Salzlösungen verwendet. Nun ist es erforderlich, die Wirksamkeit der Technologie in größerem Maßstab und mit realen Feedlösungen zu validieren.

Im Rahmen dieser Arbeit wurde der Anwendungsmaßstab der FCDI-Technologie auf Pilotmaßstab vergrößert und die Technologie in realen Entsalzungs- und Salzrecyclinganwendungen eingesetzt, gleichzeitig wurden neue Komponenten und Materialien zur Verbesserung der Kosteneffizienz entwickelt. Im Rahmen der Maßstabsvergrößerung wurden verschiedene Moduldesigns und Bauformen für Ladungsübertrager getestet. In den Experimenten wurden die Konzentrationsänderung in den FCDI-Modulen gemessen und zur Charakterisierung der Entsalzungsleistung verwendet.

Ein zentrales Ergebnis dieser Arbeit war die Entwicklung eines Stacking-Konzepts für FCDI-Module im Pilotmaßstab. Das Konzept wurde im Vergleich zu einem etablierten elektrisch-getriebenen Entsalzungsverfahren (Elektrodialyse) bewertet. Die spezifische Entsalzungsleistung der FCDI-Module im Pilotmaßstab war geringer als im Labormaßstab; hier besteht Potential für zukünftige Optimierungen. Im Vergleich zur Elektrodialyse benötigt FCDI eine größere Membranfläche, was zu höheren Investitionskosten führt. Um die Kosten der FCDI-Module zu senken, wurden neue Ladungsübertrager entwickelt. Diese konnten zu geringeren Kosten hergestellt werden und erreichten einen verbesserten Salztransport. Außerdem wurde ein Wire-Mesh Sensor entwickelt, der in Zukunft für die Untersuchung und Verbesserung von FCDI eingesetzt werden kann.

Die Anwendung von FCDI in praxisnahen Wasserentsalzungs- und Salzrückgewinnungsanwendungen ist für die Verbesserung der Technologie entscheidend. Nur durch solche Anwendungen können die Vor- und Nachteile von FCDI umfassend verstanden und iterative Verbesserungen umgesetzt werden. Die Maßstabsvergrößerung ist der wichtigste Schritt, um die Anwendung in der Praxis zu ermöglichen. Diese Arbeit demonstriert die ersten Schritte in Richtung einer industriellen Anwendung. Zukünftige Forschung sollten die Skalierung von neuen Modulkonzepten fokussieren und neue Anwendungsfelder für FCDI erschließen.

1 Introduction

Motivation

Only around $2.5\,\%$ of the earth's total water supply exists in the form of freshwater; the rest is found as seawater or brackish water [Shik2000]. Currently, the growth of the human population and global climate change strain freshwater resources around the world [Kona2020]. More freshwater is needed to sustain the growing population and improve living standards in the near future. At the same time, rising sea levels, intrusion of seawater into groundwater resources in coastal regions, and the accumulation of extreme weather scenarios will likely decrease the amount of freshwater available. As a result, $57\,\%$ of people living on Earth will suffer from scarcity of clean water by 2050. [Meko2016]; [Bore2019] Solutions are found in the desalination of seawater and brackish water. The worldwide capacity for desalination is increasing, helping to reduce water scarcity [Shan2008]; [Jone2019].

In contrast to efforts in the field of seawater desalination, increasing industrial and agricultural activities contribute to water scarcity [Cañe2013]; [Kaus2016]. Wastewater from these applications often contains salts, like chlorides, nitrates, or phosphates. If the total salt concentrations of industrial waters exceed $50\,\mathrm{g\,L^{-1}}$, they are referred to as salt brines. When brines are emitted into the environment, they negatively affect freshwater ecosystems through salinization and eutrophication and strain groundwater resources [Cañe2013]; [Schu2019]; [Bald2013]. The aim should be to reduce the emissions of wastewater or to reduce their salt content. To achieve this, increasingly strict regulations are being implemented

[Fost2019]; [Smit2009]; [Farm2018]. In addition, there is growing interest in closing material cycles and recycling these salts at high concentrations in industry processes. This is especially true for phosphate or lithium salts as a result of limited resources. However, with rising raw materials prices and the arrival of new technologies, this also applies to other salts, such as nitrates. [Driv1999]; [Huka2016]; [Li2019]; [Liu2019]; [Grai1996]; [Xu2002]; [van 2021]

Overall, the situation creates a demand in the industry for processes that can separate salts from an aqueous feed stream (desalination) and increase their concentration in another stream (concentration). Furthermore, since different salts may be present in wastewater, selective desalination, and concentration become important for future water treatment technologies [Luo2018]; [Shoc2022].

Technical Solutions

Various processes for desalination and salt concentration are known today. Elsaid et al. classify these processes as thermal processes, membrane processes, and emerging processes [Elsa2020]. Thermal processes and membrane processes are established on a large scale and are regularly applied for the desalination of seawater or industrial wastewater. Plants that desalinate thousands of cubic meters of water per hour are common. Furthermore, there are several emerging processes in the field of desalination. However, their application is often restrained by the competition of the established processes. Pilot-scale assessment of these technologies is needed to judge their technology readiness [Ahme2021].

An example of an emerging technology is Flow-electrode Capacitive Deionization (FCDI). This process offers continuous capacitive desalination and concentration at low energy demand. All capacitive desalination processes are based on the adsorption of ions to an electrode surface under the influence of an electric field. In FCDI, static electrodes are replaced by flowable solutions of carbon particles, allowing continuous

regeneration [Jeon2013]; [Gend2014]. FCDI was first described in 2013 and has been the focus of growing research interest ever since; the number of academic papers on FCDI is increasing every year [Zhan2021]. However, every new technology eventually has to prove its technology readiness in real-world applications. For desalination processes, scale-up is an important step in this assessment. Even small-scale applications of desalination and concentration in industry are typically on a scale of hundreds of liters per hour, compared to milliliters per hour on the lab scale. Scale-up can lead to the "death" of an emerging technology if it cannot show an economic advantage over established technologies [Fran1996]. However, scale-up should be attempted sooner than later to learn about a technology's actual advantages and disadvantages and to gain valuable feedback for further research.

This thesis draws from this proposition and describes the first steps in the scale-up of FCDI. The goal of this thesis is to document the current state of FCDI research and answer questions that are relevant to scale-up of the process:

- How can the size of FCDI modules be increased from lab scale to pilot scale?
- How can components of FCDI modules be manufactured more efficiently and at a lower cost?
- How can the FCDI process be tailored to real-world salt solutions?
- What is necessary to make FCDI more competitive?

Structure of this Thesis

Before taking the first steps in the direction of FCDI scale-up, an overview of the field is needed. Chapter 2 briefly reviews existing desalination and concentration technologies, before focusing on electro-membrane processes. The fundamental background of ion exchange materials and the electric

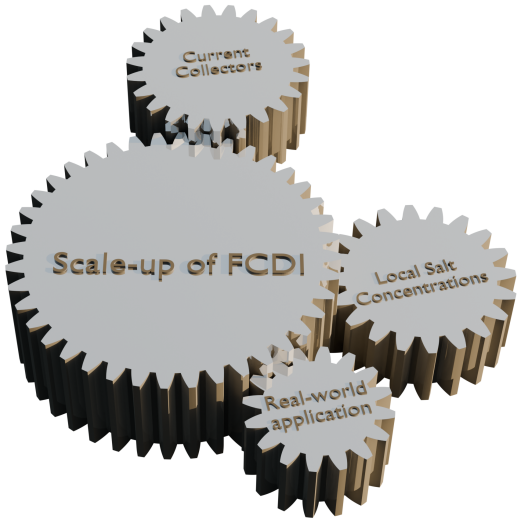

Figure 1.1: Structure of this Thesis visualized by a set of gears.

double layer is explained. The research field of FCDI is introduced, key elements of the FCDI process are discussed, and the most important research methods used in this thesis are presented.

The following chapters focus on specific steps of FCDI scale-up. Fig. 1.1 imagines the scale-up process as a set of gears that need to be set in motion: the main gear at the center is the scale-up of FCDI desalination modules. All research conducted in the field of FCDI so far has been on lab scale, with modules that allow for flow rates of milliliters per hour. The capacity of the process must be increased to make real-world applications accessible to FCDI. Chapter 3 introduces a module concept that reaches a $120\times$ increase in treatment capacity.
The main gear in Fig. 1.1 cannot turn without also turning a set of gears that are placed around it. The first one is labeled "Real-world application". Before expensive large-scale modules are built and tests at pilot scale can be started, it is important to prove that FCDI can operate with a specific salt solution and a specific set of external factors. Chapter 4 describes a way to systematically adapt the FCDI process to a given problem. The treatment of wastewater from stainless steel pickling is used as test case. An outcome from pilot-scale testing detailed in Chapter 4 is that the initial cost of FCDI modules hinders competition with established desalination technolo-

gies such as Electrodialysis.
Chapter 5 shows how the cost of FCDI can be reduced by lowering the cost of material and the labor cost incurred by one of the major components of FCDI modules. A new type of current collector is presented and compared with architectures known from literature. The new current collector shows superior salt transport and is at the same time easier to manufacture at a low cost.
Various research points toward the conclusion that there is still untapped potential in FCDI, but there is a lack of understanding of the fundamental processes that occur in the operation of FCDI [Zhan2021]. Critical information from experiments is missing: the salt transport in an FCDI module can to date only be measured at the inlet and outlet of the module, and the transport within the module itself remains a black box. Modeling is possible, but it always entails assumptions about ion transport and ion storage in flow electrodes that might not accurately describe reality. Thus, it would be highly beneficial to find a way to measure salt concentrations at various points in the FCDI module. This aspect is true for FCDI as well as for other electrochemical membrane processes. Chapter 6 shows a new approach to the measurement of local salt concentrations in the form of wire mesh sensors. A setup is developed, and the first applications of the sensor on lab scale are discussed.
Chapter 7 offers a summary of the work in this thesis and aims to draw conclusions about the future of the FCDI process.

Previous Publication of Results and Content

This thesis's content and results emanate from research conducted under the affiliation and position of the author as research fellow and PhD candidate at RWTH Aachen University. The position is associated with the Chair of Chemical Process Engineering. The author and his co-authors have previously published parts of the results presented in this thesis. Illustrations and text in this thesis are taken from published material in compliance

with copyright regulations. Material from the following research papers and research projects is used:

- N. Köller, L. Mankertz, S. Finger, C.J. Linnartz and M. Wessling, "Towards scale-up of flow-electrode capacitive deionization", *Desalination*, DOI: 10.1016/j.desal.2023.117096
- N. Köller, D. Roedder, C.J. Linnartz, M. Enders, F. Morell, P. Altmeier and M. Wessling, "Recovery of nitrate and fluoride salts from stainless steel pickling wastewater with flow-electrode capacitive deionization", *Journal of Hazardous Materials Letters*, DOI: 10.1016/j.hazl.2025.100148
- N. Köller, M. Perrey, L.K. Brückner, P. Schäfer, S. Werner, C.J. Linnartz and M. Wessling, " Comparison of current collector architectures for flow-electrode capacitive deionization", DOI: 10.1016/j.desal.2024.117595
- BMBF research project, *Nitratkreislaufführung bei der Behandlung von Metalloberflächen durch Nutzung innovativer Techniken, NITREB*, 02WQ1534D, 01.02.2020-31.07.2023
- BMBF research project, *Recycling von industriellen salzhaltigen Wässern durch Ionentrennung, Konzentrierung und intelligentes Monitoring, RIKovery*, 02WV1569, 01.02.2021-31.10.2024

The work comprises data based on the following student theses:

- Selina Finger, Master's thesis, 02.11.2020, *Scale-up configurations for flow-electrode capacitive deionization single modules*
- Dustin Roedder, Master's thesis, 10.02.2021, *Characterization of the Desalination of Nitrate and Fluoride containing wastewater using Flow-electrode Capacitive Deionization*
- Philipp Schäfer, Bachelor's thesis, 26.03.2021, *Flow-Electrode Capacitive Deionization: Design, implementation and examination of a module with a novel membrane-current collector assembly*

- Sebastian Werner, Bachelor's thesis, 01.09.2021, *Elaboration of a continuous production method of membrane-electrode assemblies for a pilot-scale desalination process*
- Leon Vahl, Bachelor's thesis, 23.09.2021, *Measurement and analysis of spatial salt concentration profiles in electrochemical desalination processes*
- Jens Bettmer, Master's thesis, 06.12.2021, *Scale-up of a membrane module for water desalination by capacitive deionization with flow electrodes from laboratory to pilot scale*
- Lukas Mankertz, Master's thesis, 30.09.2022, *From Lab to Pilot: Scale-up of Flow-Electrode Capacitive Deionization via Cell-Pair Stacking of Ion-Exchange Membranes*
- Lantz Kjell Brückner, Bachelor's thesis, 28.02.2023, *Comparison of Current-Collector Architectures for Flow-electrode Capacitive Deionization*
- Mila Perrey, Bachelor's thesis, 16.08.2023, *Flow Channel Geometries for Electrochemical Flow-electrode Capacitive Deionization: A Comparative Analysis*
- Carola Jendrzok, Master's thesis, 29.09.2023, *Development of a new Measurement Setup for the Investigation of Local Salt Concentrations in Desalination Processes utilizing Electrochemical Impedance Spectroscopy including an experimental and simulative Validation*

1

2 Theoretical Background

2.1 Technologies for Water Desalination and Concentrate Recycling

Desalination describes the separation of salts from an aqueous solution. The most prominent application is the production of drinking water from seawater. The concentration of total dissolved solids (TDS) in seawater is around $35.000\,ppm_{TDS}$, and an acceptable concentration for drinking water is $500\,ppm_{TDS}$ [Mill1974]. This is the separation task from which most desalination technologies originate [Elim2011]. This chapter aims to give an overview of the most common desalination technologies before focusing on electro-membrane processes that are closely related to the topic of this thesis. Since water desalination and energy production are closely linked with one another, the energy demand of a desalination process is an important metric. The thermodynamic minimum energy demand for desalination of seawater with a water recovery of $50\,\%$ is $1.06\,\mathrm{kWh\,m^{-3}}$ [Elim2011].

2.1.1 Thermal Processes

There are two main categories of processes for desalination and concentration: thermal processes and membrane processes. Historically, thermal processes were available before membrane processes. They include multi-stage flash (MSF) distillation, multi-effect distillation (MED), vapor compression (VC), and crystallization.

In MSF distillation, seawater is heated to temperatures between 90–$120\,°C$. The heated seawater then passes through a series of flash stages. Each stage has a pressure below the saturation pressure of the seawater at the stage temperature. This causes the seawater to flash (i.e., to boil rapidly). The flashed water vapor is collected and cooled in a heat exchanger. Cold inlet seawater can be used to cool the water vapor. The seawater in the first flash stage boils until the temperature has fallen to the boiling point. The unflashed seawater is passed to the next stage, where the process is repeated at a lower pressure. Thus, the reheating of seawater is omitted. By

using several flash stages, high brine concentrations can be reached. The condensed water vapor typically contains only $2 - 10\,ppm_{TDS}$. Thus, remineralization is necessary for usage as drinking water. The typical energy demand for MSF is $3.5\,kWh$ electrical energy and $12\,kWh$ thermal energy per $1\,m^3$ of diluate. [Khaw2008]; [Elsa2020]

MED has a lower energy demand. Seawater passes through a series of evaporators (so-called effects). In the first evaporator, the seawater is heated by steam. Seawater at its boiling point is sprayed onto a surface for evaporation. The liquid fraction after evaporation is given to the next evaporator, which is heated by the vapor formed in the first evaporator. MED can be operated at temperatures below $70\,°C$ with an energy demand of $1.5\,kWh$ of electrical energy and $6\,kWh$ of thermal energy per $1\,m^3$ of diluate. [Elsa2020]

Mechanical vapor compression (MVC) and crystallization are typically used at feed concentrations higher than seawater concentration ($35.000\,ppm_{TSD}$). So-called salt brines can be side products from industrial processes or concentrates produced in seawater desalination. The goal in the treatment of aqueous brines is zero-liquid discharge (ZLD), indicating that all water should be recycled. Brine concentration is often based on MVC [Elsa2020]. A brine stream is heated, and water vapor is generated. The vapor is mechanically compressed, leading to higher temperatures and pressures. The vapor is then fed to a heat exchanger, where the vapor condenses. The thermal energy can be used to pre-heat the brine stream. The brine stream is circulated. [Schw2018]
MVC can be used to concentrate brines up to around $250.000\,ppm_{TDS}$ [Tong2016]. This is still below the solubility limit of some salts (e.g., solubility limit of sodium chloride $360.000\,ppm$). The concentrate can be treated further in a brine crystallizer. A crystallizer is essentially a brine concentrator with the ability to separate salt crystals from a brine solution. The circulating brine stream enters the crystallizer at an angle, generating a vortex similar to a hydrocyclone. Water evaporates, and the solubility limit of the salts is exceeded, leading to the formation of salt crystals. The salt

crystals are separated from the solution in the vortex and drop to the bottom, where they are drawn out of the crystallizer. Crystallization generates high-purity salt crystals that can be recycled and used in industrial processes. [Bost1996]

2.1.2 Membrane Processes

All thermal separation processes depend on the evaporation of water (the main component in seawater) to remove salts whose feed concentration is typically only around $3\,\%$ of a seawater solution by mass. More energy-efficient options for desalination and concentration are membrane processes that do not require evaporation of water. The most prominent membrane process for desalination is Reverse Osmosis (RO). This process was enabled by the invention of a stable cellulose acetate membrane by Loeb and Sourirajan in 1962 [Loeb1962]. Another important step came with the invention of interfacial polymerization for RO membranes by Cadotte [Cado1985]. Once established as a large-scale process, RO slowly began to take over the desalination market. In 2000, the total volume of diluate produced by RO was equal to the total volume produced by thermal processes. Since 2000, the installed capacity of RO plants has increased exponentially, whereas the capacity of thermal processes has only increased slightly. In 2019, $69\,\%$ of diluate was produced by RO [Jone2019]. The energy demand for seawater desalination with an RO system is in the range of 3–$5\,\mathrm{kWh\,m^{-3}}$ of diluate produced [Kim2019]. Compared to thermal processes, this is closer to the thermodynamic minimum of $1.06\,\mathrm{kWh\,m^{-3}}$. Although RO is used primarily for the desalination of seawater or brackish water, it can also be used to treat industrial wastewater [Gree2009]; [Bóda2003]. In RO, mechanical pressure is used to reverse naturally occurring osmosis. When two solutions with different concentrations of solutes are separated by a membrane that is permeable to the solvent but not the solutes, the concentrations equalize due to water transport from the lower concentrated solution to the higher concentrated solution. The lower concentrated solution exerts pressure on the membrane, the so-called osmotic

pressure. RO starts with two feed solutions with the same concentration (e.g., seawater). Higher pressure is applied to one solution by pumping. If the pressure is high enough, water crosses the membrane. Thus, the concentrations start to change: a diluate and a concentrate are formed. The osmotic pressure between the diluate and the concentrate rises and counteracts RO. For this reason, high pressures are necessary to operate RO. [Bake2004]

$$\Delta\Pi_{D,C} = (1 + \alpha(\nu - 1)) \cdot RT \cdot (c_C - c_D) \tag{2.1}$$

The osmotic pressure difference between two solutions can be calculated on the basis of van't Hoffs law. Eq. 2.1 shows that the pressure difference $\Delta\Pi_{D,C}$ between concentrate and diluate depends on the concentrations in diluate c_D and concentrate c_C. R is the ideal gas constant, T is the temperature. α and ν describe the dissociation of the salt; α is the degree of dissociation and ν is the stoichiometric coefficient of dissociation, describing the numbers of ions that result from the dissociation of one salt molecule. For a complete dissociation ($\alpha = 1$) of a salt consisting of one anion and one cation (e.g., sodium chloride) $\nu = 2$, the term reduces to $\Delta\Pi_{D,C} = 2RT \cdot (c_C - c_D)$. The diluate concentration c_D in RO is often negligible. $\Delta\Pi_{D,C}$ then only depends on the concentration reached on the concentrate side and the temperature. [Meli2007]

For a typical seawater concentration of $35.000\,ppm_{TDS}$ and a water recovery of $50\,\%$, c_C reaches $70.000\,ppm_{TDS}$, resulting in an osmotic pressure of $\Delta\Pi_{D,C} \approx 59\,\text{bar}$ [Dave2018]. Since RO was developed for seawater desalination, the maximum pressures are around $80\,\text{bar}$, which is high enough to overcome $\Delta\Pi_{D,C}$ [Dave2018]; [Frit2007]. So-called high-pressure RO (HPRO) can reach up to $150\,\text{bar}$, or in extreme cases up to $200\,\text{bar}$, rendering it applicable to industrial brines with salt concentrations higher than seawater [Dave2018]; [Raut2000]. To achieve ZLD or produce pure salts, RO or HPRO can be coupled with thermal processes such as MVC or brine crystallization [Tong2016].

RO was developed for seawater desalination, where the required ion re-

jections are high. In RO, only water can permeate through the membrane. All ions are rejected to a high degree due to size exclusion. Thus, selectivity between different salts is not possible with RO. For certain applications, membranes with lower rejections and higher water fluxes are of interest. These membranes are commonly known as Nanofiltration (NF) membranes [Bake2004]. In NF, the rejection depends both on size exclusion and charge exclusion [Bake2004]. Multivalent ions are typically rejected to a higher degree as a result of Donnan exclusion caused by the (mostly negative) charge of the membrane material [Scha1998]. Monovalent ions pass through the membrane, which enables the separation of monovalent and bivalent salts. The pressures for NF are generally between 3–30 bar. NF has proven useful for applications where selectivity between salts or between salts and an organic component is desired. [Meli2007]

2.1.3 Electro-membrane Processes

RO and NF are pressure-driven processes in which the bulk phase permeates preferentially through the membrane while the solutes are retained. Membrane processes that instead directly remove ions from the bulk phase can be more energy efficient, especially at low ion concentrations [Gene2021]. Additionally, they typically require less pre-treatment of the feed solution. So-called electro-membrane processes feature ion-exchange membranes (IEMs, see Chapter 2.2) and use an electric field as the driving force for ion transport. In addition to the energy advantage at low concentrations, these processes can employ the inherent selectivity of IEMs [Luo2018].

Electrodialysis (ED) is the most common electro-driven membrane process. Two electrodes (anode and cathode) are placed on either side of a stack of IEMs. The IEMs are arranged in an alternating pattern: an anion-exchange membrane that allows the passage of anions is followed by a cation-exchange membrane that allows the passage of cations. The feed solutions flow through membrane spacers between the IEMs. An electric current is applied to the electrodes, and two electrochemical reactions

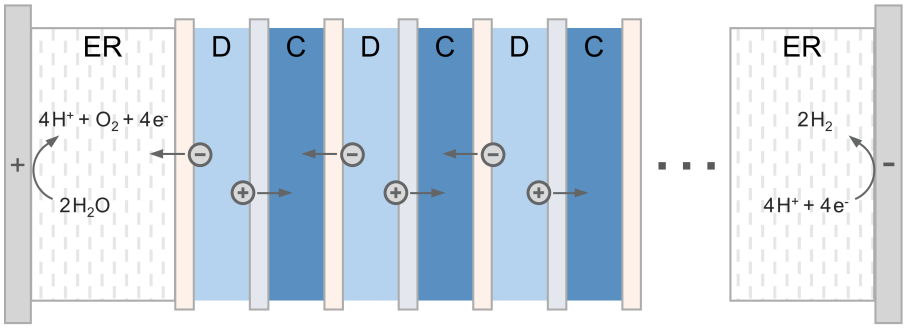

Figure 2.1: Ion transport in an ED module. Due to the arrangement of AEMs and CEMs diluate (D) and concentrate (C) channels are formed. Splitting of water into oxygen and hydrogen is a typical redox reaction at the surface of the electrodes in the electrode rinse (ER) solution.

(anode: oxidation, cathode: reduction) occur. The reactions convert the electric current of the external circuit into the movement of ions in the cell. Due to the arrangement of the IEMs, half of the feed solution channels lose their anions and cations to the neighboring channels, which gain ions from both sides. This way, diluate channels and concentrate channels emerge. Typically, the feed solutions are not in direct contact with the electrodes. Instead, a third feed solution is used as a so-called electrode rinse solution in which the electrochemical reactions occur. This solution is circulated around the cell from one electrode to the other. A typical ED module is shown in Fig. 2.1.

The conversion of an electric current to an ionic current in the cell is not perfect. Current efficiencies are typically below 90 %; the additional current is lost as overpotential for the electrochemical reactions [La C2018]; [Kim2017]; [Sun2022]. ED is an established process in industry that can be easily scaled by stacking up to 500 membranes in a plate-and-frame membrane module [Camp2018]; [Stra2004]. ED is more energy-efficient than RO at low salt concentrations; however, at seawater concentrations, RO is more efficient [Pate2021]; [Gene2021]. The lower efficiency and higher cost of IEMs compared to RO membranes lead to a small share of ED in the worldwide desalination capacity. Especially for seawater desalination, where high capacities are needed, ED is not competitive [Pate2021].

However, ED has several advantages that make it valuable for application

in industrial brine treatment. Because the ions and not the water move across the membrane, ED does not have to overcome the osmotic pressure of the solution. This means that high concentrations (that are impossible with classical RO) can be reached and that ED can replace technologies such as HPRO or MVC. Typically, multi-stage ED processes are used, and the concentrate can be used as feed to a crystallization unit. This enables the application of ED in the context of ZLD or salt recycling. High pressures and phase changes are omitted, leading to a lower energy demand than MVC. [Sun2022]; [Yan2019]; [Jian2014]. Work by Zhang et al. highlights the advantages of ED in brine treatment: they used a three-stage process with monovalent selective IEMs in the first stage to treat RO concentrate. This enables the production of a sodium chloride (NaCl) brine with a relatively high purity and a concentration high enough for subsequent crystallization. [Zhan2017]
Furthermore, ED allows better control over fouling and scaling than RO. In so-called Electrodialysis Reversal, the polarity of an ED stack is changed at regular intervals, allowing the removal of colloid material and precipitations from the membrane surfaces [Stra2004]. Thus, the feed pre-treatment requirements for ED are lower than for RO [McGo2014].

Capacitive desalination processes can be even more energy efficient than ED. Here, no reactions take place at the electrodes. Instead, ions move in the electric field, forming electric double layers (see Chapter 2.3) at the electrode surfaces. Capacitive deionization (CDI) has been known since the 1960s and has received increasing attention through the integration of IEMs into the process in Membrane Capacitive Deionization (MCDI) [Ande2010]; [Oren2008]; [Pora2013]; [Suss2015]; [Ahme2018]. MCDI cannot be used for high salt concentrations, but it is beneficial for the desalination of brackish waters or as a polishing step. So far, there are only a few applications of MCDI on a pilot or industrial scale [Xing2020]. More information on Capacitive Deionization and MCDI is given in Chapter 2.4 after the theoretical foundations of IEMs and the electric double layer are introduced.

In summary, there are several different processes for desalination and salt concentration. In many applications, membrane processes are replacing thermal processes because of improved energy efficiency. The demand for seawater desalination is expected to increase worldwide due to population growth and climate change. From today's technological perspective, membrane processes (especially RO) will mainly satisfy this demand. In the future, thermal processes will only be used for seawater desalination in places where enough energy is readily available. Treatment of industrial brines will increase in the future as a result of regulatory demand and limited resources [Tong2016]. This leaves a niche for membrane processes like ED, which can deal with high salt concentrations and offer selectivity between different salts. Younger technologies such as MCDI offer distinct advantages over ED in specific cases and have the potential to further reduce the energy demand for desalination and concentration.

2.2 Ion-exchange Membranes

Ion-exchange membranes (IEMs) are an integral part of electro-driven membrane processes, since they allow the separation of a feed solution into a diluate and a concentrate. IEMs are a particular form of ion-exchange material. These are any materials that allow the replacement of ions in a solution with different ions of the same charge. Some naturally occurring materials (e.g., zeolites in soil) can act as ion exchangers. The first synthetical zeolites for ion exchange were developed at the beginning of the 20th century. They were used to remove potassium from sugar juices and to soften water. Today, the most common ion-exchange materials are based on cross-linked polystyrene with different functional groups and are used in different applications (e.g., ion chromatography, water softening, and preparation of ultrapure water). [Zago2007]; [Kuma2013]

IEMs are effectively ion-exchange resins in the form of a thin film [Stra1995]. They typically consist of a polymer matrix with charged fixed groups. Only counterions with a charge opposite to that of the fixed groups

can pass the membrane, while co-ions with the same charge as the membrane are rejected [Xu2005]. Ceramic IEMs exist, but polymeric IEMs dominate the market and are widely used in electrochemical processes [Link2001]; [Chen2023]. They can be divided into anion-exchange membranes (AEMs) and cation-exchange membranes (CEMs). AEMs contain positively charged chemical fixed groups (e.g., $-NH_3^+$, $-NRH_2^+$, $-NR_3^+$) and allow anions to pass through the membrane. Cations are rejected. CEMs contain negatively charged fixed groups (e.g., $-SO_3^-$, $-COO^-$, $-PO_3^{2-}$) that allow passage of the cations. The exclusion of co-ions from the IEM matrix due to fixed groups of the same charge is known as Donnan exclusion [Donn1911]; [Stra1995].

Research on IEMs dates back to the fundamental work of Ostwald in the 1890s and Donnan in the 1910s [Ostw1890]; [Donn1911]. Meyer and Strauss were the first to suggest a separation process based on the alternating arrangement of IEMs [Meye1940]. However, technical realization at the time was difficult due to the lack of membranes with suitable characteristics. Developing stable, selective IEMs with low electrical resistance was necessary to enable ED as an industrial process. Breakthrough research in this field was conducted by Juda and McRae at Ionics Inc. and Winger et al. at Rohm and Haas [Juda1950]; [Wing1953]. Another milestone was the development of Nafion® material for CEMs by the company DuPont. These membranes have found applications in chlor-alkali electrolysis, fuel cells, and electrolyzers.

Today, IEMs are indispensable for processes in water treatment and for electro-membrane processes at the center of a new low-carbon economy, e.g., water electrolysis for hydrogen production, chlor-alkali electrolysis or CO_2 reduction [Chen2023]. Electrodialysis is the primary water treatment process that utilizes IEMs, but it also finds a multitude of different applications in chemical or food industries. Bipolar membranes consisting of an anion-exchange layer and a cation-exchange layer have been researched since the 1950s and have found application mainly in the production of acids and bases from salt solutions [Fril1956]; [Naga1977];

[Pärn2021]. Due to the variety of applications that depend on IEMs, they are researched extensively. The main goals are to make IEMs cheaper, lower their electrical resistance, improve their stability, and reduce the fouling propensity [Jian2021].

In many processes, counterion selectivity is an essential characteristic of IEMs [Luo2018]. Ion transport through membranes is a complex topic; only a basic overview is given here. The research on monovalent selective IEMs that block multivalent counterions is summarized in reviews by Sata et al. [Sata2000]; [Sata2002]. The transport rate of counterions through a membrane depends on the concentration in the bulk liquid, the mobility of the ions, and the ion-exchange selectivity [Luo2018]; [Stra2004]. The mobility of ions is influenced by the size of ions and their hydrated radii. Larger hydrated radii slow ion transport. Ion-exchange selectivity is caused by electrostatic interactions between the counterions and the fixed ions in the membrane. Ions with higher valency generally have a higher ion-exchange selectivity [Stra2004]. Building on the work of Sata et al. and Strathmann et al., Luo et al. give ranking orders for the transport of ions through AEMs and CEMs (with fixed sulfonic groups) [Sata2000]; [Stra2004]; [Luo2018]:

$$AEMs: I^- > NO_3^- \approx Br^- > NO_2^- > Cl^- > SO_4^{2-} > F^- \tag{2.2}$$

$$CEMs: Ba^{2+} > Sr^{2+} > Ca^{2+} > Mg^{2+} > H^+ > Cu^{2+} \approx Zn^{2+} \approx Ni^{2+} > K^+ > Na^+ > Li^+ > Fe^{3+} \tag{2.3}$$

In this thesis, selectivity between NO_3^- and F^- is important for the real-world application of FCDI in Chapter 4. As shown in Eq. 2.2, NO_3^- is preferentially transported when both ions are present in a solution.

2.3 Electric Double Layer

The term Electric Double Layer (EDL) describes a phenomenon at the boundary between electrodes and an electrolyte solution. Under the influence of the electric field, oppositely charged ions (counterions) from the electrolyte solution accumulate on the electrode surface. The regions of excess charge balance each other so that the interfacial layer as a whole is

electrically neutral. [Bock2000]

Different models were introduced to describe the EDL. The first EDL model by Helmholtz dates back to 1853 [Helm1853]. In this model, the counterions at the surface fully neutralize the surface charge of the electrode. Thus, the electric field is restricted to a monolayer at the surface. The monolayer of anions at the surface of an anode and the potential predicted by the Helmholtz model are shown in Fig. 2.2 (a). The potential Ψ decreases linearly from its initial value at the surface ($x = 0$) to zero within the width of the monolayer ($x = x_h$). This first model neglected the diffusion and thermal movement of the ions in the electrolyte, which play an important role in boundary layer processes [Bock2000]; [Wang2011]. Gouy and Chapman, independently from each other, developed a different EDL model (GC model) [Gouy1910]; [Chap1913]. Their model accounts for the motion of ions by diffusion. The counterions are attracted to the electrode surface but at the same time expelled due to the thermal movement [Pora2013]. This movement leads to the formation of a diffuse boundary layer. The potential within this layer is described by Eq. 2.4 [Bock2000].

$$\Psi(x) = \Psi_0 \cdot exp^{-\kappa \cdot x} \tag{2.4}$$

The GC model is shown in Fig. 2.2 (b). The concentration of counterions decreases with increasing distance from the electrode surface and the potential Ψ decreases according to Eq. 2.4. The GC model assumes a continuous charge distribution, thus disregarding the molecular nature of the ions in the electrolyte solution. This leads to problems in systems with high surface potential Ψ_0 and high ion concentration. For such a system, the GC model predicts ion concentrations in proximity to the surface, which are impossible in reality, because ions are not ideal point charges but have a radius and cannot be closer to the surface than their radius [Bard2000]. Stern solved this problem by combining the Helmholtz and the GC model. In the so-called Gouy-Chapman-Stern (GCS) model, the EDL consists of two different regions: a thin double layer (Stern layer) at the surface and a diffuse GC layer [Pora2013]. The potential predicted by the GCS model is shown in Fig. 2.2 (c). In the Stern layer, the de-

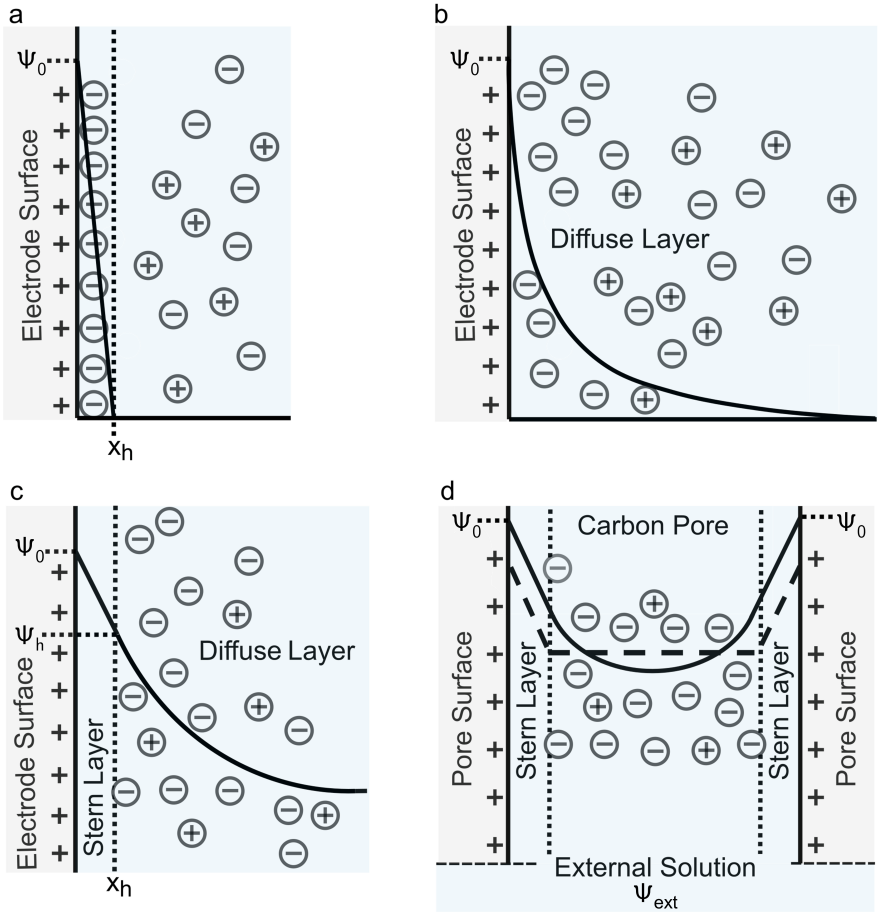

Figure 2.2: (a) Helmholtz model: the positive charge of the electrode is compensated by a monolayer of anions at the electrode surface. (b) Gouy-Chapman model with a diffuse layer at the electrode. (c) Gouy-Chapman-Stern model with Stern plane at distance x_h. (d) Modified Donnan model for overlapping EDLs in micropores. The depiction of (c) and (d) is adapted from [Bies2014].

crease of the potential is linear. In the diffuse layer starting at the distance x_h, the potential is characterized by Eq. 2.4. The GCS model has been used in the description of Capacitive Deionization systems [Bies2009a]; [Bies2009b]. It assumes that EDLs can extend freely into the solution. This assumption creates issues in systems with microporous carbon electrodes. The micropores have a size range similar to that of the diffuse layer of the EDLs, suggesting that the EDLs within the micropores are highly overlapping. To account for this, Biesheuvel et al. developed a new model based on the Donnan model to describe the ion concentration in the micropores [Bies2011]. They called this the "modified Donnan (mD)" model, since they included a Stern layer at the surfaces of the microp-

ores and a term for the chemical attraction that occurs in an uncharged system. The mD model is shown in Fig. 2.2 (d). The figure shows the different behavior of the potential in the pore space. Contrary to the GCS model, the potential in the mD model does not decrease to the level of the external solution. The mD model gives a good representation of the ion storage in micropores and is today mostly used for modeling of EDLs in literature [Hemm2015]; [Romm2018]; [Romm2020a]; [Shi2023].

2.4 Capacitive Deionization

Capacitive Deionization (CDI) is a desalination process that utilizes an electric current to remove ions from a feed solution. CDI is based on the Electric Double Layer (EDL) principle introduced in Chapter 2.3. Research on CDI began in the 1960s with the work of Blair, Murphy, Arnold, and Caudle [Blai1960]; [Arno1961]; [Murp1967]. Today, CDI has been applied by researchers on a pilot plant scale and has been commercialized by companies like Voltea Inc., Dallas [Welg2005]; [Moss2013]; [Xing2020].

A CDI desalination module, in its simplest form, consists of two electrodes with a large specific surface area facing each other so that an electric field can be built up. The surface area is provided by highly porous materials, mostly activated carbon. The operation of a CDI module usually begins with a desalination step: a feed solution is pumped into the module and flows between the two electrodes. A voltage is applied to the electrodes, and the ions in the feed solution start to move in the electric field, as shown in Fig. 2.3 (a). The anions move to the anode, and the cations move to the cathode, where they are stored in the EDLs at the electrode surfaces. The ion concentration at the module outlet is lower than the concentration at the inlet. Eventually, the EDLs at the electrode surfaces are saturated and cannot store more ions. Thus, the outlet concentration starts to increase again. A regeneration step is necessary to release the ions from the EDLs. This can be done by reducing or reversing the voltage. In the regeneration step, the ions are transferred from the electrode surfaces into the bulk liquid, and

a solution with a higher concentration is generated. [Ahme2018]

The two operation steps render the process ideally reversible as long as no chemical reactions occur, allowing CDI modules to have a long lifetime and require little maintenance [Pora2013]. However, the two steps also lead to discontinuous diluate output, which is a major disadvantage of the process [Oren2008]; [Pora2014]. Furthermore, during the regeneration step, oppositely charged ions move into the EDLs at the surface. This unwanted transport (in Fig. 2.3 (a) shown with dashed arrows) reduces the storage capacity of the EDL and leads to longer regeneration times.

The problem of unwanted charge transport during regeneration can be solved by introducing ion-exchange membranes (IEMs) to the process. As described in Chapter 2.2, IEMs allow either cations or anions to pass. Thus, they can effectively prevent the transport of oppositely charged ions into the carbon matrix during regeneration. An anion-exchange membrane (AEM) is placed at the surface of the anode, and a cation-exchange membrane (CEM) is placed at the surface of the cathode. During desalination, anions can pass through the AEM and adsorb in the carbon matrix. During regeneration, they are expelled and pass through the AEM back into the solution. However, cations can no longer adsorb at the anode during the regeneration step, as the AEM prevents them from entering the carbon matrix. The application of membranes to a CDI module was first described in a patent by Andelmann [Ande2004]. This form of CDI was called Membrane Capacitive Deionization (MCDI) and was studied by different groups of researchers, all reporting an enhancement in the salt removal capability [Lee2006]; [Li2008]; [Zhao2012]. The desalination and regeneration steps of MCDI are shown in Fig. 2.3 (b).

However, the problem of discontinuous output of CDI persisted. An interesting solution to this problem was offered by Porada et al. in 2012. They used conductive rods with a thin porous carbon electrode layer at the surface (some rods were also fitted with membranes), which were alternately dipped into a freshwater and a brine compartment. When the rods were dipped into the freshwater compartment, the potential was ap-

plied so that the ions could be stored in the EDLs of the rods. The potential was turned off in the brine compartment, allowing the ions to migrate back into the bulk solution. The researchers stated that this setup could be scaled up and eventually lead to continuous output from a CDI or MCDI system [Pora2012].

However, the breakthrough in continuous capacitive deionization technology came in 2013 with the development of Flow-electrode Capacitive Deionization (FCDI) [Jeon2013]. Here, flow electrodes are used to facilitate the parallel adsorption and desorption of ions to the electrodes. The desorption step can occur in a second FCDI module as shown in Fig. 2.3 (c), or the two modules can be combined in a single module with a diluate and a concentrate channel as shown in Fig. 2.3 (d). FCDI is described in more detail in the next chapter.

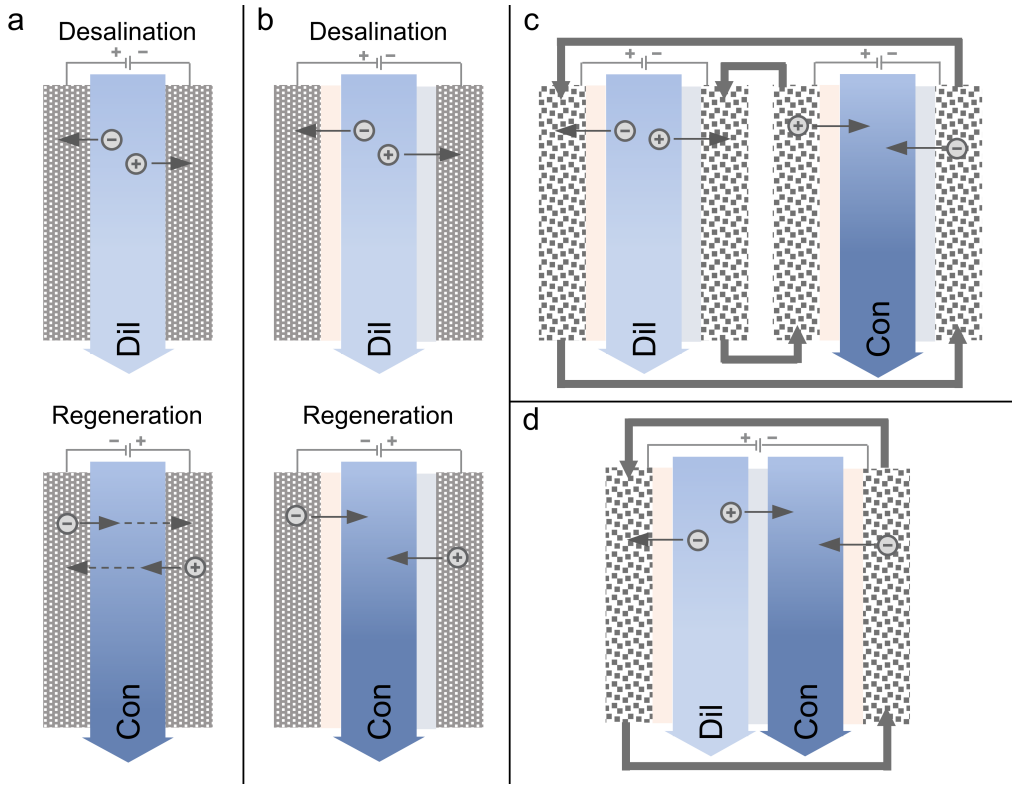

Figure 2.3: Operating principle of capacitive deionization processes. (a) CDI module during desalination and regeneration. Adsorption of oppositely charged ions during regeneration is shown by dashed arrows. (b) MCDI module during desalination and regeneration. (c) FCDI in a two-module setup with desalination occurring in the left module and concentration in the right module. (d) FCDI in a single-module setup with an AEM-CEM-AEM module configuration.

2.5 Flow-electrode Capacitive Deionization

Continuous capacitive deionization was presented by Jeon et al. in 2013 [Jeon2013]. They replaced the static electrodes in MCDI with flow electrodes and termed the process Flow-electrode Capacitive Deionization (FCDI). In the past ten years, this process has attracted growing academic interest [Zhan2021].

In FCDI, the pumpable flow electrodes enable simultaneous desalination and regeneration of the electrode material. Regeneration can be performed in a second module as shown in Fig. 2.3 (c). Desalination is done in the first module, while flow electrode regeneration (and concentration of the feed solution) occurs in the second module [Gend2014]. In this case, each module consists of three compartments: the spacer channel for the feed solution and two flow electrode channels. Two IEMs per module are needed, one AEM and one CEM. Rommerskirchen et al. used a single-module layout in which desalination and concentration occur in the same module as shown in Fig. 2.3 (d). With this layout, they showed the applicability of FCDI for high salt concentrations, rendering FCDI a valuable addition to existing processes for treating industrial wastewater with high salt concentrations [Romm2015]; [Romm2020b].

In a single-module FCDI setup, two feed solutions enter the module and are separated by one IEM. Two additional IEMs are used on the other side of the two solutions to separate them from the flow electrodes. Thus, less material is used in a single-module setup. While a two-module setup needs four current collectors and four IEMs, a single-module setup only needs two current collectors and three IEMs. All work presented in this thesis is conducted with a single-module FCDI setup. An overview of the integral parts of the FCDI process is shown in Fig. 2.4 and discussed in the following sections.

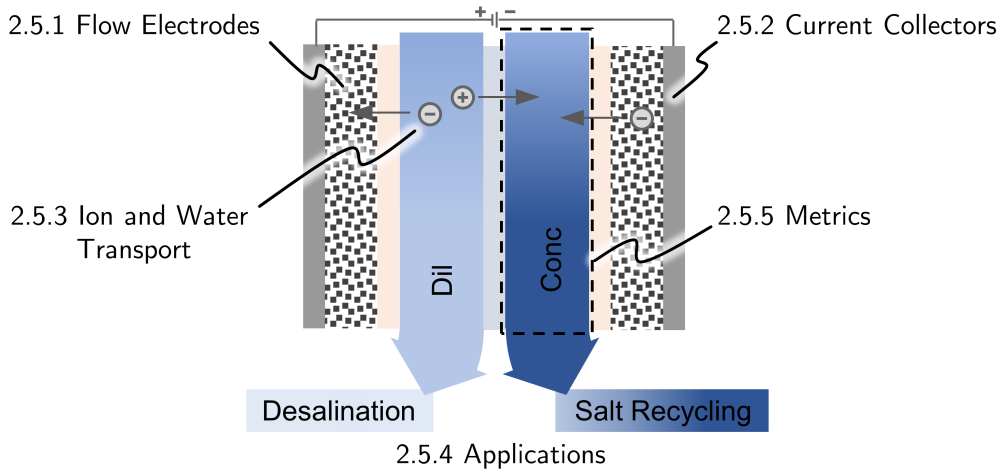

Figure 2.4: Overview of key elements of key elements of the FCDI process that are discussed in the following sections.

2.5.1 Flow Electrodes

Flow electrodes are a crucial component of FCDI. Electrodes consisting of active materials in a flowable liquid are also known from other processes, such as redox-flow batteries (RFBs). RFBs store energy in dissolved redox pairs. These components are electrochemically active and undergo redox reactions at the electrodes [Wang2013]. However, in FCDI, the flow electrodes must not participate in electrochemical reactions. The inertness of the flow electrodes is an important prerequisite for the successful operation of FCDI. Instead, flow electrodes need to provide a large surface area for the adsorption of ions. This is achieved by suspending particles with a large specific surface area in a liquid. Such flow electrodes (or slurry electrodes) have been known since the work of Kastening et al. [Kast1988]; [Kast1997]. They used activated carbon particles to carry charges from an electrode to a reactor. Presser et al. applied slurry electrodes to energy storage in a concept called an electrochemical flow capacitor [Pres2012].

The particles in flow electrodes are charged by contact with static current collectors and by the formation of charge percolation networks [Hatz2017]. The charge causes the ions to move to the surfaces of the porous particles, where they are stored in the electric double layer (see Chapter 2.3).

In early FCDI research, flow electrodes with suspended activated carbon particles were used [Jeon2013]; [Gend2014]; [Pora2014]. Not only were activated carbon flow electrodes known from the work of Kastening et al., activated carbon is also mainly used as electrode material in CDI. In the past ten years, work on flow electrodes has been a significant part of FCDI research [Zhan2021]. Some researchers focused on a better understanding of charge transfer in flow electrodes [Hatz2017]; [Dixi2019]; [Loha2019]; [Padl2024]. Other researchers investigated different carbon-based materials [Hatz2015]; [Tang2019]; [Fola2022]. Flow conditions and mass loadings were investigated in simulations and experimentally [Romm2019]; [Heid2021].

Generally, mass fractions of the particles in the flow electrodes are limited at $\sim 25\,wt\%$, due to the increase in viscosity and the risk of clogging. Several publications deal with the enhancement of flow electrodes through the modification of carbon-based particles or conductive additives (e.g., carbon black). These materials can improve the conductivity and capacity of flow electrodes. [Hatz2015]; [Xu2017]; [Yang2017]; [Tang2019]; [Akuz2020]; [Wang2021b]; [Hwan2021]; [Fola2022]; [Wang2022]; [Zhan2023]; [Yan2023]. The actual contribution of capacitive storage to ion removal in FCDI is the subject of debate, since Ma et al. found that suspensions of carbon black particles with low surface area but high conductivity outperformed regular flow electrodes based on activated carbon [Ma2020b]. The charge transfer from the current collectors to the flow electrode particles can also be enhanced with organic redox couples, like benzoquinone/hydroquinone. However, these redox mediators pose the risk of contamination of the product water [Ma2016]. Non-toxic redox mediators such as iron salts might be better suited for freshwater applications [Frei2024]. In so-called intercalation materials, ions can be stored in interstitial sites in a crystal lattice. These materials can be used in CDI (the system is then sometimes referred to as battery desalination) [Xu2020]; [Sing2019]. Some researchers have also used these materials in flow electrodes [Chan2019]; [Xu2021c].

Optimization of flow electrodes also needs to take into account the effect of the electrolyte. The conductivity of the particle suspension is low, mainly if no conductive additives are used. To increase the conductivity, salts are added to flow electrodes as background electrolytes. To avoid contamination, salts that are also present in the feed solutions should be used. Concentrations should be tailored to avoid increased water cross-over due to osmosis (see Chapter 2.5.3) [More2018].

Although flow electrode engineering is an integral part of FCDI research, this thesis is more concerned with the scale-up of FCDI modules. Thus, the same activated carbon is used in all experiments; the mass fraction is kept constant at $15\,wt\%$, and only electrolyte concentrations are adapted to the specific separation task. However, the FCDI current collectors and modules presented in this thesis could be used with any optimized flow electrode system to harvest benefits such as improved conductivity or increased charge capacity.

2.5.2 Current Collectors

Current collectors are elements used in different electrochemical cells. They are typically used to establish electrical contact between the electrode (at which the electrochemical reaction occurs) and the external electrical circuit [Ito2012]; [Zhu2021]. Current collectors for flow electrode processes differ from those used in other applications such as fuel cells or batteries. Because the electrode is not a solid but a suspension of particles, current collectors typically feature a flow channel to guide the flow electrode through the electrochemical cell.

The contact resistance between the particles and the current collector significantly influences the overall resistance to charge transfer, as demonstrated by simulations [Heid2021]. After being charged, the particles attract ions, which are stored in the electric double layer at the particle surface. Dennison et al. conducted a study on an electrochemical flow capacitor to examine how resistance and conductance are affected by the channel

depth and flow rate. They found that approximately 40 % of the cell's resistance originated from fixed resistances of current collectors and the interfacial resistance between the current collector and the flow electrode. Furthermore, they emphasized the interdependence of flow electrode composition and module design [Denn2014]. This highlights the importance of current collectors for the FCDI process.

To date, the investigation of FCDI has primarily been conducted at a laboratory scale. However, when attempting to scale up the process, the significance of current collectors becomes increasingly apparent. Unlike ED, where additional IEMs can be added between the electrodes to scale up the system, this approach is not feasible for FCDI as it would result in the accumulation of resistances and potentially require an increase in electrode voltage, which could surpass the threshold for water splitting (see Chapter 3) [Zhan2021]. Therefore, alternative methods are required for scale-up. An approach proposed by Cho et al. involves using a porous three-dimensional lattice structure that allows the flow of both the flow electrode and feed solutions [Cho2017]. Such three-dimensional current collectors were also used in the form of metal meshes or foams [Zhan2022a]; [Zhan2024]. Another demonstration by He et al. achieved scale-up through a tubular FCDI module [He2021]. However, most researchers use plate- and frame-type modules for FCDI scale-up. In this case, stacking, similar to ED modules, can be employed. However, in FCDI, not only do IEMs need to be stacked but the flow-electrode channels and current collectors must also be repeated. Consequently, current collectors bear a resemblance to bipolar plates utilized in electrolyzers or fuel cells.

Graphite plates are commonly used as current collectors in FCDI. They meet all necessary criteria: they are electrically conductive, chemically inert in salt solutions, can be easily machined, and are not too expensive. However, they are not suitable for stacking. The graphite is brittle and susceptible to breaking; thus, thick plates are needed to achieve mechanical stability. Furthermore, machining the flow channels does cause significant costs. For these reasons, alternative current collector architectures have

been investigated in the past. Xu et al. used so-called membrane-current collectors (MCCs) in which a titanium mesh is combined with the ion-exchange membrane [Xu2021b]; [Xu2021a]. Chen et al. coated graphite current collectors with polyaniline to reduce surface roughness and ohmic resistance at the interface between the current collector and the flow electrode [Chen2022]. Li et al. used additional carbon felts in their modules and achieved a 63 % increase in salt removal rate [Li2024]. In the past, our group has developed membrane-electrode assemblies (MEAs), in which the IEM is hotpressed to a carbon fiber fabric (CFF) [Linn2020]. In this case, the membrane and the current collector are combined in a single part, with the CFF acting as functional reinforcement. Thus, thinner membranes could be used. Chapter 3 of this thesis deals with the implementation of MEAs in a pilot-scale FCDI module. Chapter 5 deals with the comparison of graphite plates and MEAs with a newly developed current collector.

2.5.3 Ion and Water Transport

FCDI depends on the movement of ions in an electric field between the current collectors. However, ion transport also always entails water transport due to the hydration shells of the ions that are moved. Hydration shells form as a result of the dipolar nature of the water molecules and cluster around the charged ions. [Stra2004] The number of water molecules in the hydration shell varies for different ions [Impe1983]. As discussed in Chapter 2.2, the hydration shell influences the transport of ions through IEMs. Ions with larger hydrated radii are typically less mobile and thus less likely to cross the IEM. This is an important factor in the selectivity of IEMs between ions of equal charge [Luo2018].

Generally, water transport counteracts the desired desalination/concentration in FCDI. Ions move from diluate to concentrate. The water that is transported with the ions leads to a lower concentration in the concentrate and a higher concentration in the diluate. Furthermore, water transport across IEMs can also occur due to osmosis. If there is a concentration difference between the solutions on either side of an IEM, water will cross from the

solution with the lower concentration to the solution with the higher concentration. The difference in osmotic pressure between two solutions can be calculated with Eq. 2.1. Water transport can be influenced by the ion-exchange membranes used [Pora2018].

In FCDI, the extent of osmotic water transport is different for a single-module setup than for a two-module setup. In a two-module setup, each feed solution only comes into contact with the flow electrodes; therefore, if the electrolyte concentration in the flow electrode is correctly set, osmotic water transport between the feed solutions and the flow electrodes can be minimized. In a single-module setup, the feed solutions come into contact not only with the flow electrode but also with each other. Since the goal of the FCDI process is to increase the concentration in one solution and decrease the concentration in the other, there will always exist a concentration difference that leads to osmotic water transport. This becomes a problem at high concentration differences, i.e., if the aim is to completely remove salt from the diluate feed stream or if high concentration factors are demanded on the concentrate side.

2.5.4 Applications

Since the first mention of FCDI in 2013, the process has been applied to a multitude of possible applications. In theory, FCDI can be used in the same applications as CDI or ED. Most researchers use sodium chloride solutions at seawater or brackish water concentrations to test FCDI modules [Chun2020]. Some examples of other applications are given in Table 2.1. This overview is not comprehensive, but showcases the variety of problems that can be approached with FCDI.

Most researchers focus on applications with low salt concentrations, which could also be treated with CDI. Rommerskirchen et al. showed that FCDI can also be used to target high salt concentrations [Romm2020b]. They conducted experiments with feed solutions that were in the range of industrial brines ($60\,g_{NaCl}/L$ and $120\,g_{NaCl}/L$). These are concentrations in which

Application	Feed Solution	Source
Ammonia recovery	$20\ \frac{mg_N}{L}\ NH_4Cl$	[Fang2018]
Nitrate Removal, Ammonia recovery	*Synthetic groundwater*	[Sun2023]
Phosphorus removal	$50-150\ \frac{mg_P}{L}\ NaH_2PO_4$	[Zhan2020a]
Fluoride removal	$500-1500\ \frac{mg}{L}\ NaCl + 5\ \frac{mg}{L}\ NaF$	[Jian2022]
Heavy metal removal	*Synthetic groundwater*	[Ma2019]
Heavy metal removal	$650\ \frac{mg}{L}\ Na_2SO_4 + 240\ \frac{mg}{L}\ CuSO_4$	[Zhan2020b]
Heavy metal removal	$250-1000\ \frac{mg}{L}\ KCl + 3\ \frac{mg}{L}\ Cr(VI)$	[Dong2021]
Lithium extraction	$1-100\ \frac{mg}{L}\ LiCl$	[Ha2019]
Brackish water softening	$2000\ \frac{mg}{L}\ NaCl + 0.15\ \frac{mg}{L}\ CaCl_2$	[He2018]

Table 2.1: Examples of FCDI applications from literature.

FCDI no longer competes with CDI, but mainly with technologies such as High-pressure Reverse Osmosis or Electrodialysis (see Chapter 2.1). So far, the research on FCDI applications has been done on lab scale. The amount of desalinated or concentrated solutions is typically in the range of milliliters to liters. It is important to bring the FCDI process from the lab scale to an industrially applicable scale to compare it to other established technologies. An overview of concepts and designs for scale-up is given in Chapter 3.

2.5.5 Metrics for FCDI

For every technology in development, it is important to define a uniform set of metrics that are used to compare the performance of the process. In the field of Capacitive Deionization, most research groups use the metrics described by Suss et al. and Hawks et al. [Suss2015]; [Hawk2019]. These metrics are commonly understood by other researchers. The metrics can also be applied to FCDI.

In this thesis, Current Efficiency (CE) and Average Salt Transport Rate (ASTR) are used to evaluate the results from FCDI desalination/concentration experiments. If not stated otherwise in the Experimentals section of a chapter, potentiostatic experiments are conducted with a voltage of $1.2\,V$ at the current collectors, and feed solutions with concentrations of

$c_F = 60\,\mathrm{g\,L^{-1}}$ sodium chloride (NaCl) are used for diluate and concentrate. CEs are calculated according to Eq. 2.5 with the valence of the salt z_{salt} ($z_{salt} = 1$ in the case of NaCl), the Faraday constant F, and the number of cell pairs n_{cp}. The current I is the average current in the sampling time and M_{salt} is the molar mass of the salt used in the experiment. The salt mass flux $\Delta\dot{m}_{salt}$ can be calculated through a mass balance around the concentrate or diluate channels. These mass balances are decoupled from each other by the flow electrode compartment. Typically, the results of these independent mass balances will vary. Thus, individual CEs for diluate and concentrate are calculated and averaged. The same procedure is applied to the average salt transfer rate (ASTR), calculated according to Eq. 2.6. The average salt mass flux is divided by the active membrane area installed in the modules $A_{mem,tot}$. This has the advantage that, once the salt mass flux for an application is known, the necessary membrane area can be calculated directly from the ASTR.

$$CE = \frac{z_{salt} \cdot F \cdot \Delta\dot{m}_{salt}}{n_{cp} \cdot I \cdot M_{salt}} \tag{2.5}$$

$$ASTR = \frac{\Delta\dot{m}_{salt}}{A_{mem,tot} \cdot M_{salt}} \tag{2.6}$$

Although CE and ASTR are generally understood in the field of work, a comparison to the work of other researchers remains complicated due to the variety of salts and feed concentrations used in the experiments. A lower feed concentration leads to lower conductivity in the FCDI cell and lower currents. This shows the need for a widely agreed standardized experiment to compare the performance of different modules.

The aim of an FCDI experiment is often to reach certain concentrations on the diluate and concentrate side. For this reason, outlet concentrations normalized by the feed concentration c_F are also included in the evaluation. These values directly show whether a certain target (e.g., desalination to $c = 0.1 c_F$) was reached. Normalized concentrations are accessible metrics that are also easy to communicate to people outside the CDI research community. However, normalized concentrations must be treated carefully,

due to the water transport that occurs in conjunction with ion transport (see Chapter 2.5.3). Some simple examples can be used to show the impact of water transport on normalized concentrations: a simplified FCDI experiment (E01) is run with $c_{F,D} = c_{F,C} = 60\,\mathrm{g\,L^{-1}}$. Both feed flow rates are set to $1\,\mathrm{mL\,min^{-1}}$. Outlet flow rates and concentrations are given in Tab. 2.2. The values are not taken from experiments, but they are chosen realistically. A normalized diluate concentration of $c_D/c_{F,D} = 0.5$ is reached. Intuitively one would assume a concentration degree of $c_C/c_{F,C} = 1.5$. However, this is not the case. Due to the significant water transport across the ion-exchange membranes, the normalized concentration of the concentrate is lower ($c_C/c_{F,C} = 1.33$). Results like these are always found in experiments.

		Feed		Output					
		Conc.	Flowrate	Conc.	Flowrate	c/c$_F$	$\lvert\Delta\dot{m}_{NaCl}\rvert$	Current	CE
		$[g/L]$	$[mL/min]$	$[g/L]$	$[mL/min]$	$[-]$	$[mg/min]$	$[A]$	$[-]$
E01	D	60.00	1.00	29.79	0.79	0.50	36.34	1.00	1.00
	C	60.00	1.00	79.90	1.21	1.33	36.34	1.00	1.00
E02	D	60.00	1.00	12.81	0.71	0.21	50.88	1.40	1.00
	C	60.00	1.00	86.09	1.29	1.43	50.88	1.40	1.00
E03	D	60.00	1.00	13.94	0.65	0.23	50.88	1.40	1.00
	C	60.00	1.00	82.40	1.35	1.37	50.88	1.40	1.00

Table 2.2: Evaluation of the normalized concentration c/c_F in three thought experiments.

Now, a second FCDI experiment (E02) is conducted with the same feeds and an increased current of $I = 1.4\,\mathrm{A}$. The flow rates and concentrations at the outlet are adjusted so that all mass balances are in check and $CE = 1$. The ratio of water transport to ion transport is kept constant. The resulting $|\dot{m}_{NaCl}|$ is $40\,\%$ higher than in the initial example. The normalized diluate concentration is $57\,\%$ lower than before ($c_D/c_{F,D} = 0.21$), but the normalized concentrate concentration is only slightly improved ($c_C/c_{F,C} = 1.43$). This shows that with more ion transport, the perceived "imbalance" shown in E01 increases. In reality, the effect would be even more severe, since the ratio of water transport to ion transport would increase in the second experiment because of osmosis. In example E03 this ratio is increased by $20\,\%$.

Now $c_C/c_{F,C}$ is only slightly higher than in E01. This is an extreme case, but effects like this do happen in reality: Chapter 4 shows that $c_C/c_{F,C}$ can decrease with increasing voltage due to the competitive transport of two different salts. Overall, the thought experiments highlight that in a system with significant water crossover, normalized outlet concentrations should be evaluated carefully and the analysis of an FCDI experiment cannot be based on concentration differences alone.

2.6 Analytical Methods

The main method for the analysis of FCDI modules are desalination and concentration experiments, as described in Chapter 2.5.5. In these experiments, conductivity measurements are used to obtain online data. Ion chromatography is used to measure the ion concentration of samples taken during experiments. In ion chromatography, the samples flow through a column filled with an ion-exchange resin. Different species of ions interact more strongly with the resin and take more time to pass through the column. Therefore, the conductivity at the outlet of the column is time-dependent with peaks for individual ion species. The peaks in the chromatogram can be used to calculate the concentrations of different species of ions. [Smal2013]
An in-situ method for the characterization of the FCDI or other electrochemical cells is Electrochemical Impedance Spectroscopy (EIS). EIS can be combined with wire mesh sensors (WMS), leading to locally resolved measurements. In this thesis, this approach is used in Chapter 6. Therefore, EIS and WMS are described in the following sections.

2.6.1 Conductivity

Ohm's law describes the relation between resistance R, voltage V and current I as given in Eq. 2.7. The reciprocal of R is called the conductivity G [Schm2012]. The resistances depend on the distance d and the cross-

sectional area A used for the measurement. Thus, the specific resistances ρ and conductivities κ can be calculated.

$$R = \frac{U}{I} = \frac{1}{G} \tag{2.7}$$

$$\rho = R \cdot \frac{A}{d} \tag{2.8}$$

$$\kappa = G \cdot \frac{d}{A} \tag{2.9}$$

The conductivity of an electrolyte depends on the concentration. Conductivity measurements are often used to determine salt concentrations. Solutions with a higher salt concentration generally have a higher conductivity. The equivalent conductivity κ_{eq} is obtained by dividing the conductivity by the molar concentration c_M and the charge of a considered ion z. The total specific conductivity of a solution with different dissolved ions can be calculated as the sum of the individual specific conductivities and the conductivity of pure water κ_{water} (see Eq. 2.11).

$$\kappa_{eq} = \frac{\kappa}{c_M \cdot z} \tag{2.10}$$

$$\kappa = \sum z_i \cdot c_{M,i} \cdot \kappa_{eq,i} + \kappa_{water} \tag{2.11}$$

The Kohlrausch law given in Eq. 2.12 is an empirical correlation of molar conductivity and molar concentration for low concentrations of strong electrolytes (e.g., sodium chloride). κ_∞ is the molar conductivity at infinite dilution (i.e., in a situation without interaction between individual ions), and k is a coefficient that depends on the type of ions in solution. [Schm2012]; [Bech2018]

$$\kappa_{eq}(c_M) = \kappa_\infty - k \cdot \sqrt{c_M} \tag{2.12}$$

2.6.2 Electrochemical Impedance Spectroscopy

Electrochemical Impedance Spectroscopy (EIS) is a technique that can be used to characterize electrochemical systems. In this chapter, EIS is briefly introduced. For an in-depth explanation of the method, the reader of this

thesis is referred to standard literature (e.g., Bockris - Modern Electrochemistry). Impedance is the resistance to an alternating current in an electrical circuit. In the case of potentiostatic EIS, a sinusoidal alternating potential is applied to an electrochemical cell, and the resulting alternating current responses are measured. The impedance Z is determined by calculating the time-dependent ratio of voltage and current.

$$Z = \frac{V(t)}{I(t)} = \frac{V_0 \cdot sin(\omega t)}{I_0 \cdot sin(\omega t + \phi)} \tag{2.13}$$

The radial frequency ω is calculated as $\omega = 2\pi f$ with the frequency f. V_0 is the peak voltage and I_0 the peak current. [Bock2000]

Using Euler's notation, Eq. 2.13 can be reformulated to:

$$Z = \frac{V(t)}{I(t)} = Z_0 \cdot exp^{j\phi} = Z_0 \cdot (cos(\phi) + jsin(\phi)) = Z' + jZ'' \tag{2.14}$$

Z' represents the real part, the resistance to a current flow, and Z'' represents the imaginary part, the capability to store electrical energy. A geometric visualization of the impedance is given in the so-called Nyquist plot in Fig. 2.5 (a) [Wang2021a]. The imaginary part $-Z''$ is plotted over the real part Z'. The result is a vector of length $|Z|$ and the angle of phase shift ϕ.

During an EIS measurement, the voltage frequency is adjusted within a wide range, typically spanning multiple orders of magnitude. The impedances at these various frequencies are measured and represented in a Nyquist plot. This allows the creation of an equivalent circuit model for the electrochemical cell being tested. An equivalent circuit model consists of basic components that can be connected in parallel or in series. Two such components are shown in Fig. 2.5 (b) and (c). The resistance, denoted as Z_R, contributes only a real part to impedance and is not affected by measurement frequency. On the other hand, the ideal capacitor exhibits a frequency-dependent impedance given by $Z_C = \frac{1}{j\omega C}$. The phase shift of the capacitor is $-90°$, with the impedance becoming infinitely large at low frequencies and infinitely small at high frequencies. [Bock2000]
There are more complex components that can be used to build equivalent

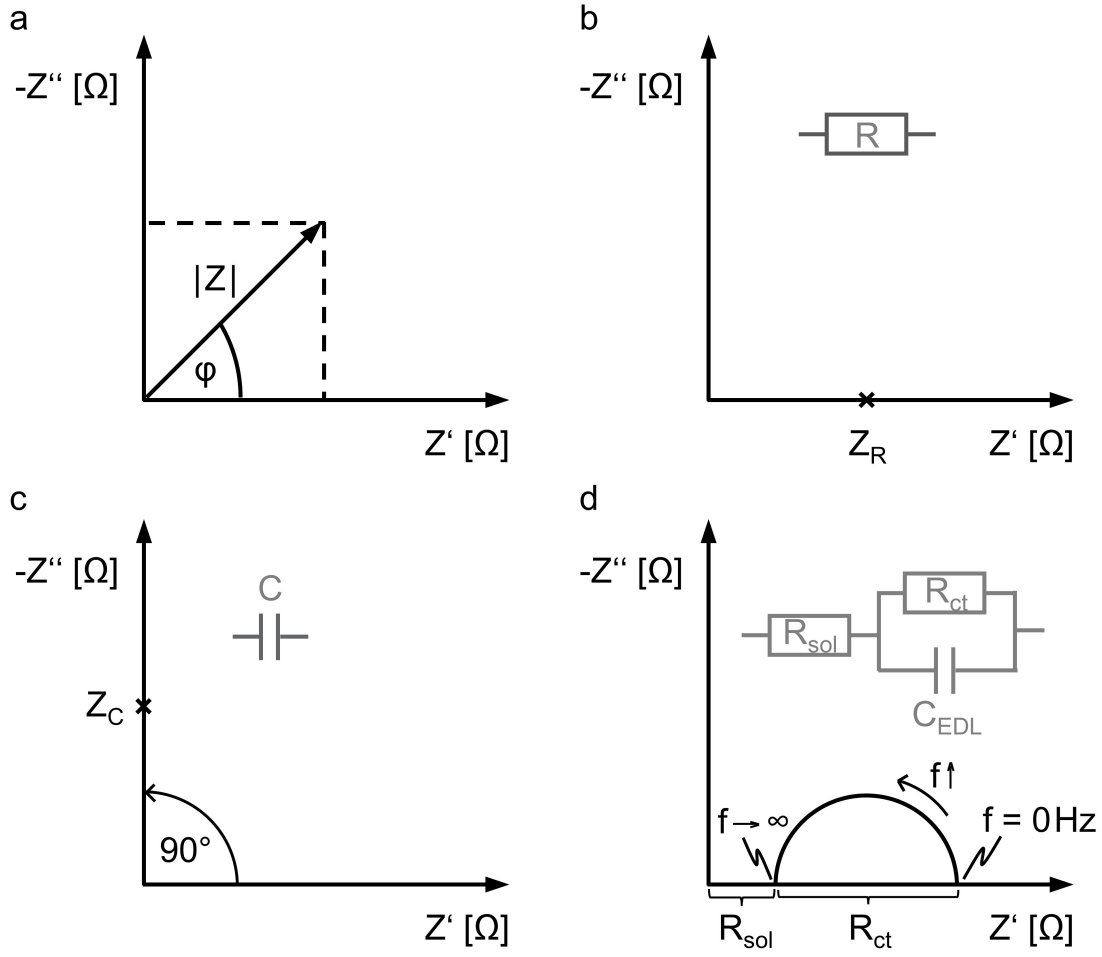

Figure 2.5: Impedance shown in a Nyquist plot. (a) General concept of EIS visualized by a vector with the length $|Z|$ and the angle of phase shift ϕ. (b) Impedance of a single resistance R. (c) Impedance of a single capacitance C. (d) Impedance of a Randles circuit with the solution resistance R_{sol} the charge transfer resistance R_{ct} and the double layer capacitance C_{EDL}.

circuit models. However, a more detailed description of these elements would go beyond the scope of this thesis.

When electrical components are connected, Kirchhoff's laws apply: in a series connection, the impedance of two components is equal to the sum of their impedances. In a parallel connection, the impedance of two components is equal to the reciprocal of the sum of the impedances of the circuit elements.

The Randles circuit, shown in Fig. 2.5 (d), is a simple equivalent circuit of an electrochemical cell with an interface between electrodes and an

electrolyte. It comprises a parallel connection of the resistance R_{ct} and the capacitor C_{EDL}. Additionally, this combination is connected in series with a second resistance R_{sol}. R_{ct} is the charge transfer resistance of the electrode-solution interface, R_{sol} is the solution resistance, and C_{EDL} is the capacitance of the electric double layer (EDL, see Chapter 2.3) [Krau2007]. The behavior of the two resistances in the Randles circuit is frequency-independent. At low frequencies, the capacitor has an infinitely large impedance. The current follows the path of least resistance, flowing through the resistance R_{ct}. The total impedance is the sum of R_{sol} and R_{ct}. At high frequencies, the impedance of the capacitor becomes infinitely small. The current follows the path of the capacitor. Thus, the total impedance is the impedance of the resistance R_{sol}.

EIS has often been used to investigate slurry electrodes [Hoyt2018]; [Pete2015]; [Denn2014]. Rommerskirchen et al. and Kim et al. used EIS to investigate FCDI modules [Romm2019]; [Kim2023]. The current collectors are used as electrodes for the EIS measurement, and an equivalent circuit model comprising all membranes and fluids is developed. The influence of flow electrode composition, activated carbon particle size, and flow rate on the FCDI process can be investigated. The results allow a comparison of flow electrodes and operating conditions. However, the measurements always describe the entire FCDI cell and not individual fluid streams in the cell. To achieve this, wire mesh sensors can be applied to FCDI.

2.6.3 Wire Mesh Sensors

Wire Mesh Sensors (WMS) are a tool for the investigation of moving multiphase flows. WMS typically consist of two planes of wires arranged in a grid (see Fig. 2.6 a). These grids consist of a minimum of two wires, a transmitter electrode and a receiver electrode. Usually, these wires are positioned in two planes that are rotated $90°$ relative to each other. The number of wires used in literature ranges from 8×8 to 128×128. The distance between the planes is usually between $0.35\,\mathrm{mm}$ and $3\,\mathrm{mm}$, while the wires within the planes are placed between $0.5\,\mathrm{mm}$ and $15\,\mathrm{mm}$ apart from

each other. Smaller distances between the wire electrodes improve local resolution.
The grid is placed in a liquid flow (or a two-phase flow), and the resistances or capacitances at the crossing points between individual wires are measured. This enables a local resolution of the measured quantity. Switching between measurement points is typically achieved with a fast multiplexer circuit. Thus, time-resolved measurements are possible by performing multiple measurements successively. [Vela2015]

WMS were first described in a patent by Johnson and were used to measure the fraction of water in oil by determining the conductivity of the fluid [John1987]. Different geometries of WMS are described in literature (e.g., radial, planar, µWMS) [Klie2008a]; [Ito2011]; [Dams2009]. In planar WMS, the grids are replaced by flat electrodes in the form of printed circuit boards (PCBs), which offer a wider range of designs. Ito et al. used a so-called µWMS for measurements in a narrow rectangular channel. The wires are placed parallel to the liquid flow or on both sides of the liquid flow. This configuration creates a non-intrusive sensor mesh that is better suited for measurements in thin channels [Ito2011].

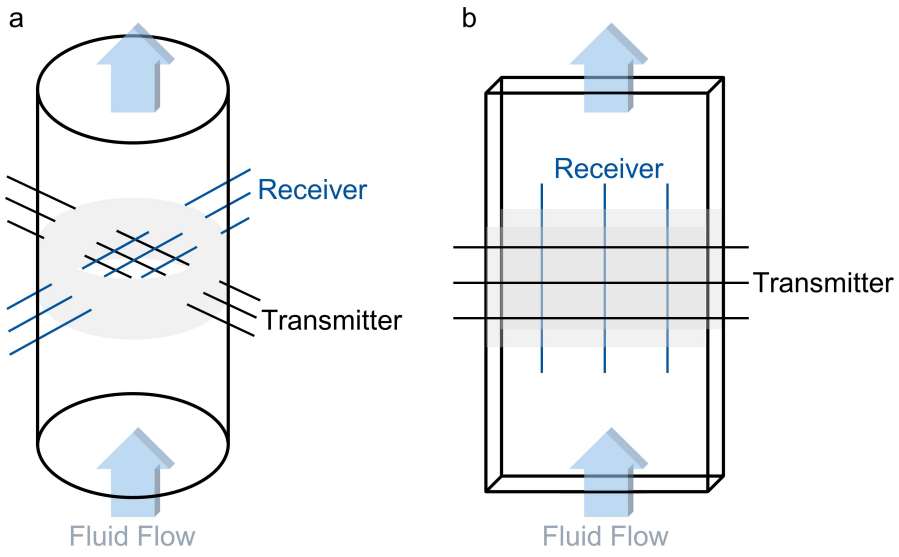

Figure 2.6: (a) Typical radial WMS used in pipes (adapted from [Vela2015]). (b) µWMS used in narrow channels (adapted from [Ito2011]).

WMS are mainly used for the evaluation of gas-liquid flow, because of the

large difference in conductivity between gases and liquids. The size and velocities of gas bubbles in a liquid flow can be evaluated [Vela2015]. However, the technique can also be applied to liquid-liquid flow (e.g., oil in water) [Silv2007]; [Rodr2011]. Höhne et al. and Kliem et al. used WMS to investigate the mixing of two coolant streams. They used a sodium chloride solution as a tracer in one of the coolant streams and investigated the conductivity during mixing [Höhn2006]; [Klie2008b]. This is the only application in literature where a salt concentration is measured with WMS.

Although WMS have shown good agreement with established methods and can be used in various applications, they do have some limitations. A drawback is the invasive characteristic of most WMS geometries, caused by the wires occupying sections of the fluid's cross-sectional region [Vela2015]. This can result in a pressure drop or changes in fluid velocity. To minimize this effect, the wire diameter should be as small as possible while still being able to resist the drag forces of the flow. Another drawback is the temperature-dependency of the measurements. When the fluid's temperature changes, its conductivity also changes, and the results differ. To account for this, it can be useful to implement temperature sensors near the WMS crossing points to record temperature data, which can then be included in the evaluation of the results [Mane2003]. Placing mesh crossing points too close to each other can result in cross-talk between sensors, affecting the accuracy of the measurements [Vela2015]. In this thesis, WMS are used to measure local and time-dependent salt concentrations in a spacer channel.

2

3 Scale-up of Flow-electrode Capacitive Deionization

Parts of this chapter have been published as:

Niklas Köller, Lukas Mankertz, Selina Finger, Christian J. Linnartz, Matthias Wessling

Towards pilot scale flow-electrode capacitive deionization, Desalination, 2023

DOI: 10.1016/j.desal.2023.117096

3.1 Introduction

Flow-electrode Capacitive Deionization (FCDI) is a rather young technology, and its industrial application is still pending. So far, the technology readiness level (TRL) of FCDI can be described as Level 4 - the technology is thoroughly validated in a laboratory environment [Mank2009]. First scale-up approaches towards TRL 5 are described in the literature: most approaches use plate-and-frame type modules with stacked units similar to Electrodialysis (ED) [Ma2020a]; [Yang2016]. ED is described in more detail in Chapter 2.1. Xu et al. introduced an assembly of a membrane and a current collector for FCDI [Xu2021b]; [Xu2021a]. Novel module concepts were also investigated: He et al. demonstrated the possibility of a tubular module [He2021]. Kim and co-workers introduced a three-dimensional system with a honeycomb structure [Cho2017]; [Choo2019]. It is difficult to compare the treatment capacity of these systems due to differences in experimental parameters. However, the highest feed flow rates are $40\,\mathrm{mL\,min^{-1}}$, and the total amount of salt removed is well below $100\,\mathrm{mg\,min^{-1}}$. Zhang et al. remarked in their review on FCDI that there is still a lack of systems with a treatment capacity of up to $100\,\mathrm{L\,d^{-1}}$ [Zhan2021]. To increase the scale of FCDI, a layout for a stacked plate-and-frame module is developed and tested.

3.1.1 Module Layout

For plate-and-frame-type FCDI modules with flat IEMs, components of ED modules (especially membranes and spacers) can be used. In previous work by our group, we investigated different approaches to stack plate and frame modules in FCDI with a membrane cross-section of $40\,\mathrm{cm^2}$ [Linn2022]. This work is used as a reference to evaluate the scale-up presented in this Chapter. The membrane area is first increased from $40\,\mathrm{cm^2}$ (lab scale) to $320\,\mathrm{cm^2}$ (pilot scale). Then a stacking concept is used to further increase the total membrane area. The approach typically used in ED is the stacking of many cell pairs between two working electrodes. This is

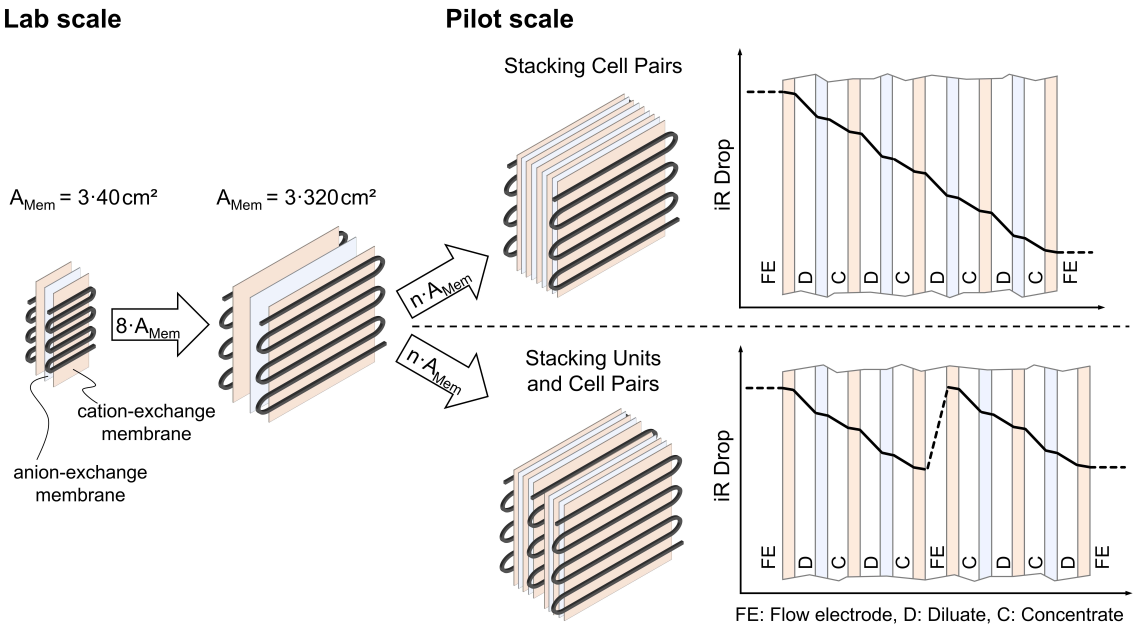

Figure 3.1: Roadmap for FCDI scale-up: First, the active membrane area A_{Mem} is increased from 40 cm^2 to 320 cm^2. Then stacking is used to reach the pilot scale. The higher ohmic iR drop in the upper stacked system with four cell pairs leads to lower currents between the current collectors. This can be avoided by adding a second stacking unit instead.

not feasible for FCDI: the resistance of the repeating cell pairs becomes too high and the current across the cell decreases [Pate2020]. The problem is visualized in Fig. 3.1 which shows two modules with the same number of diluate and concentrate channels. In the upper module, this is achieved with four cell pairs, leading to a higher ohmic iR drop and smaller currents available for ion transport. In ED, this problem is negligible, as the voltage at the electrodes can be increased to values of 400 V to gain high currents. This is impossible for FCDI since faradaic reactions must be avoided, and therefore the electrode voltage should be kept below 1.23 V. Instead, the entire cell pair with the flow electrode channels must be repeated ("stacking units"), as shown in the lower module in Fig. 3.1.

Here, stacking of cell pairs is employed together with stacking units. The Stacking Units (SUs) are independent FCDI cells that share one flow electrode. Each stacking unit (SU) comprises two cell pairs (CP). This was found to be the optimal number of cell pairs at which high current efficiencies are still possible [Ma2020a]; [Linn2022]. Fig. 3.2 shows the resulting

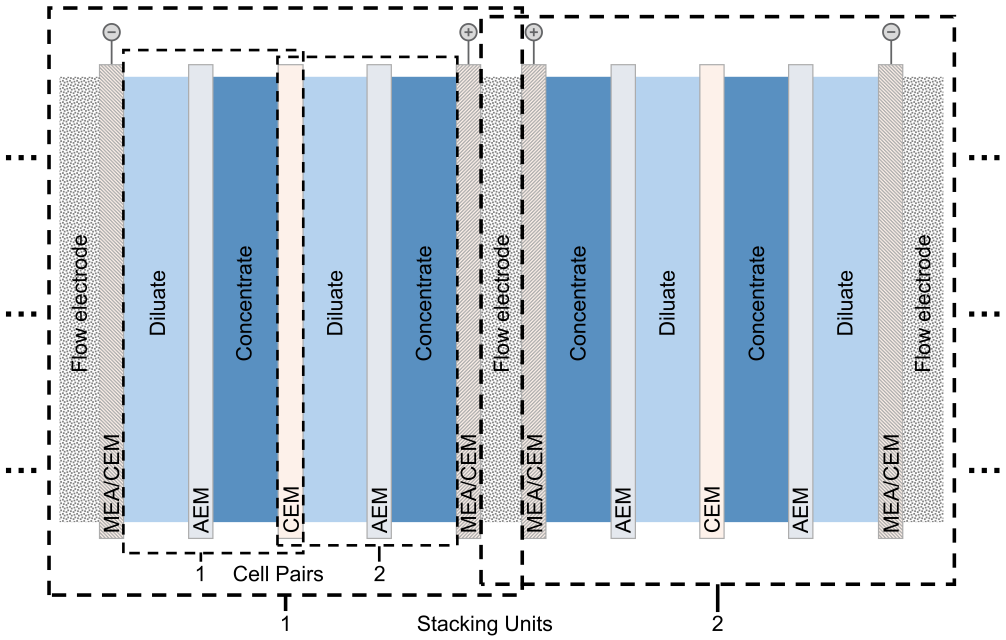

Figure 3.2: Stacking of an FCDI module with membrane-electrode assemblies (MEAs), anion-exchange membranes (AEMs) and cation-exchange membranes (CEMs). Each stacking unit consists of two cell pairs. The neighboring stacking units share the flow electrode channel in the middle.

stacking concept. One CP consists of a diluate and concentrate channel separated by an anion-exchange membrane (AEM). One cation-exchange membrane (CEM) is shared with the neighboring CP. Each SU comprises two flow electrode channels shared with the neighboring SUs. This is enabled by two-sided flowfields, similar to bipolar plates in fuel cells or electrolyzers. All flow electrode channels in a stack are connected parallel to each other. The main advantage of this stacking concept in comparison to a parallel connection of multiple FCDI modules is that less endplates are needed. This approach uses only two endplates for up to 20 stacking units, instead of two endplates per module. Membrane-electrode assemblies (MEAs) are used to transport the current to the flow electrodes. MEAs are a combination of a cation-exchange membrane (CEM) with a carbon fiber fabric acting as a current collector (see Chapter 2.5).

3.1.2 Comparison to Electrodialysis: a Thought Experiment

As described above, the use of SUs is necessary to enable FCDI scale-up. However, this leads to a disadvantage in the comparison of FCDI with ED. Summarized briefly, fewer ions are transported with the same current because fewer channels are involved in the transport of current between the electrodes. This can best be explained with a thought experiment. Fig. 3.3 shows an FCDI module based on the stacking concept described above and an ED module with the same number of membranes. The FCDI module consists of 3 SUs with 2 CP each. This leads to a total of 6 diluate channels and 6 concentrate channels. The ED module with 15 membranes has seven diluate and seven concentrate channels. This thought experiment aims to compare the currents that are used for ion transport in both modules. For this, it is helpful to compare the equivalent circuits drawn in Fig. 3.3. The equivalent circuit of the FCDI module is a parallel connection of three resistances with the value R_1. The ED module is characterized by a single resistance R_2. Importantly this is a macroscopic model for operation with direct current. For the thought experiment, we assume that all IEMs (including MEAs) have the same resistance $R_{Mem} = 0.12\,\Omega$. All diluate channels have the resistance $R_{Dil} = 0.4\,\Omega$ and all concentrate channels have the resistance $R_{Conc} = 0.3\,\Omega$. Resistances of the flow-electrode are neglected since it is assumed that charge transfer occurs directly at the MEA surface. The resistance of the electrode rinse solution in the ED module is also neglected. Eq. 3.1 and Eq. 3.2 show the calculation of R_1 and R_2.

$$R_1 = 5 \cdot R_{Mem} + 2 \cdot R_{Dil} + 2 \cdot R_{Conc} = 2.0\,\Omega \tag{3.1}$$

$$R_2 = 15 \cdot R_{Mem} + 7 \cdot R_{Dil} + 7 \cdot R_{Conc} = 6.7\,\Omega \tag{3.2}$$

We now assume that both modules are operated at a total current of 1.8 A. Thus, the voltage between the MEAs in the FCDI module is 1.2 V, and a current of 0.6 A flows through all stacking units. In the ED module, the total current of 1.8 A flows through all seven CPs. Because overpotentials at

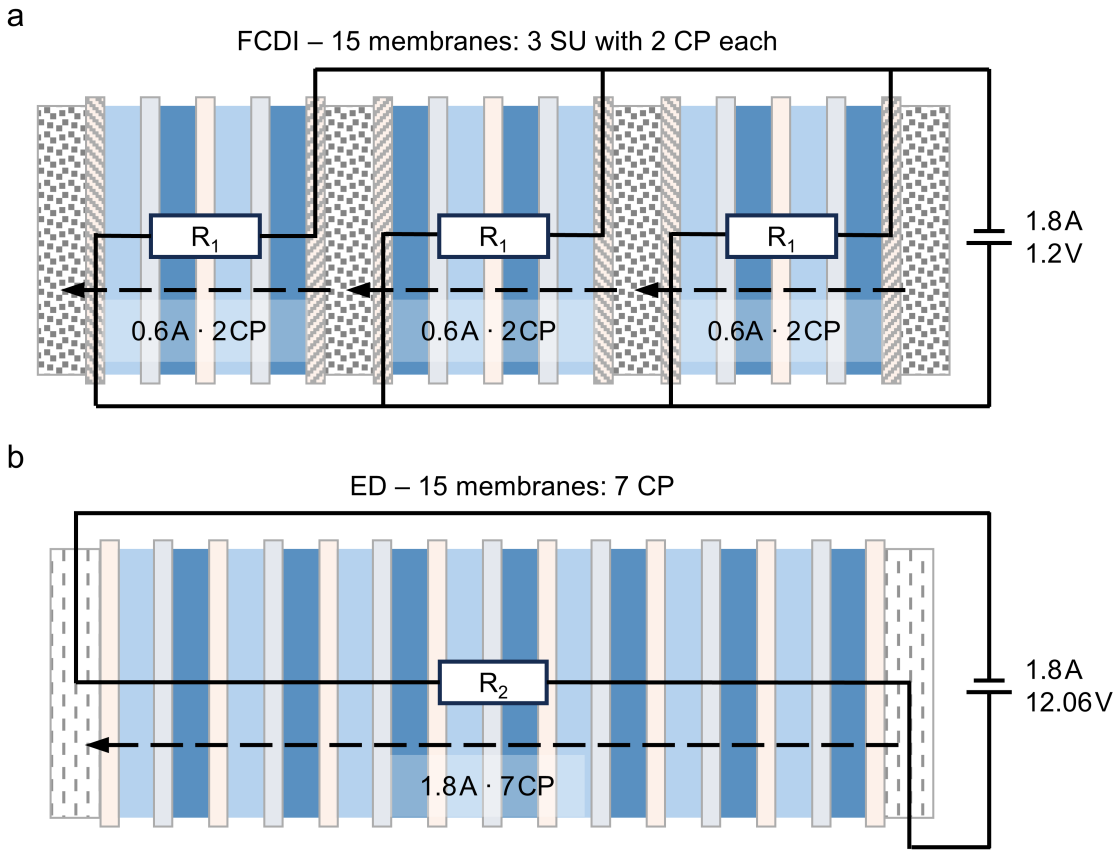

Figure 3.3: (a): Stacked FCDI module with 15 membranes operated at 1.8 A and 1.2 V. The module can be described as a parallel connection of three resistances with the value R_1. (b): Stacked ED module with 15 membranes operated at 1.8 A and 12.06 V. This module can be represented by a single resistance R_2.

the electrodes are neglected, the total voltage of the ED module is 12.06 V. The main question of this thought experiment is how many ions can be transported with the currents in the two modules. Generally, an electric current I leads to a molar ion flow of $\dot{n} = I/F$ with the Faraday constant F. For a single CP and for a monovalent salt, this means that I/F cations and I/F anions are transported from the diluate to the concentrate. However, if I is transported across multiple CPs, the total amount of ions transported is multiplied by the number of CPs. Therefore, more ions are transported with the same current. This is the reason why cell pair stacking is so efficient for ED. However, higher voltages are necessary to drive the current across the higher resistance of multiple CPs. Higher voltages at the electrodes render this form of stacking difficult for FCDI, as shown in Fig. 3.1. In the

thought experiment, we can calculate the total salt transport $\dot{n}_{FCDI}$ and $\dot{n}_{ED}$ for a monovalent salt. For the FCDI module, the current of $0.6\,\mathrm{A}$ acts on two CPs. This happens three times in parallel. For the ED module, the current of $1.8\,\mathrm{A}$ acts on seven cell pairs.

$$\dot{n}_{FCDI} = \frac{0.6\,\mathrm{A}}{F} \cdot 2 \cdot 3 = 37\,\mu\mathrm{mol\,s^{-1}} \tag{3.3}$$

$$\dot{n}_{ED} = \frac{1.8\,\mathrm{A}}{F} \cdot 7 = 131\,\mu\mathrm{mol\,s^{-1}} \tag{3.4}$$

The total salt transport achieved with the ED module at the same total current is around $3.5\times$ higher than with the FCDI module. Because both modules use the same number of membranes, a greater ion flux per membrane area is achieved. A given separation task can be achieved with ED with a lower number of membranes, resulting in a lower investment cost for the module.

However, the energy demand is also higher. In the thought experiment, the power required for the FCDI module is $P_{FCDI} = 1.8\,\mathrm{A} \cdot 1.2\,\mathrm{V} = 2.16\,\mathrm{W}$, which leads to a specific energy demand of $E_{FCDI} = 0.06\,\mathrm{J\,\mu mol^{-1}}$. The power required for the ED module is $P_{ED} = 1.8\,\mathrm{A} \cdot 12.06\,\mathrm{V} = 21.71\,\mathrm{W}$, which leads to a specific energy demand of $E_{ED} = 0.17\,\mathrm{J\,\mu mol^{-1}}$, a factor of 2.87 higher than E_{FCDI}. In praxis, E_{ED} would be even higher due to overpotentials at the electrodes. For an increased number of membranes (e.g. 100 membranes), $\frac{\dot{n}_{ED}}{\dot{n}_{FCDI}} \approx 3.74$ and $\frac{E_{ED}}{E_{FCDI}} \approx 2.82$.

This thought experiment shows the theoretical advantages and disadvantages of FCDI stacking. However, it is necessary to build a stacked module to compare it with ED in a real-world process. This chapter aims to describe the stacked module and test it. In general, this study and the data below aim to (a) establish a methodology and metrics to compare performance at different scales and (b) quantify the limiting factors and performance losses that occur when the new FCDI desalination and concentration concept is taken from a small scale to an industrially applicable scale.

3.2 Experimental

3.2.1 FCDI Modules

Three FCDI modules were built and tested in experiments with $60\,g\,L^{-1}$ sodium chloride (NaCl) feed solutions. All modules are based on the single-module layout [Romm2015]. The modules are designed to fit ion-exchange membranes with an active membrane area of $320\,cm^2$ (ED-320 membranes, Fumatech BWT GmbH). First, two modules with two stacking units were built to investigate the scale-up from modules with ED-40 membranes used in previous studies. One module was built with current collectors made from graphite plates (A320 GP 2 SU), and the other with membrane-electrode assemblies (A320 MEA 2 SU). Each stacking unit consists of two cell pairs (i.e., two diluate channels and two concentrate channels). The order of membranes in each cell pair is CEM-AEM-CEM. The fabrication of membrane-electrode assemblies (MEAs) is described by Linnartz et al. [Linn2020]. For the MEAs, no freestanding IEMs are necessary. Therefore, $30\,\mu m$ thin FKS-30 membranes (Fumatech BWT GmbH) were used. Furthermore, $10\,mm$ wide rims at the outer edges of the MEAs were fitted with copper tape with conductive adhesive (ET 1181, 3M Corporation) to lower the electrical contact resistance of the external wires to the MEAs. The copper tape allows wires to be soldered directly to the MEAs. In addition to the two 2 SU modules, a third module with 20 SUs (A320 MEA 20 SU) was built using MEAs to investigate a scaled-up stacked system. An overview of the material is given in Tab. 3.1.

The A320 GP 2 SU module was built with current collectors made from graphite (MR40, Müller & Rössner GmbH & Co. KG, $250 \times 250 \times 10\,mm$), the flow channels were milled directly into the plates. For the MEA modules, the polymeric flow fields were 3D printed (printer: Objet Eden260, material: VeroClear, Stratasys Ltd.). Because this material is less brittle than graphite, flow fields can be thinner. They were manufactured in $5.9\,mm$ thickness. However, the layout of the flow electrode channels is the same. The layout is shown in Fig. 3.4 (a). There are three parallel flow chan-

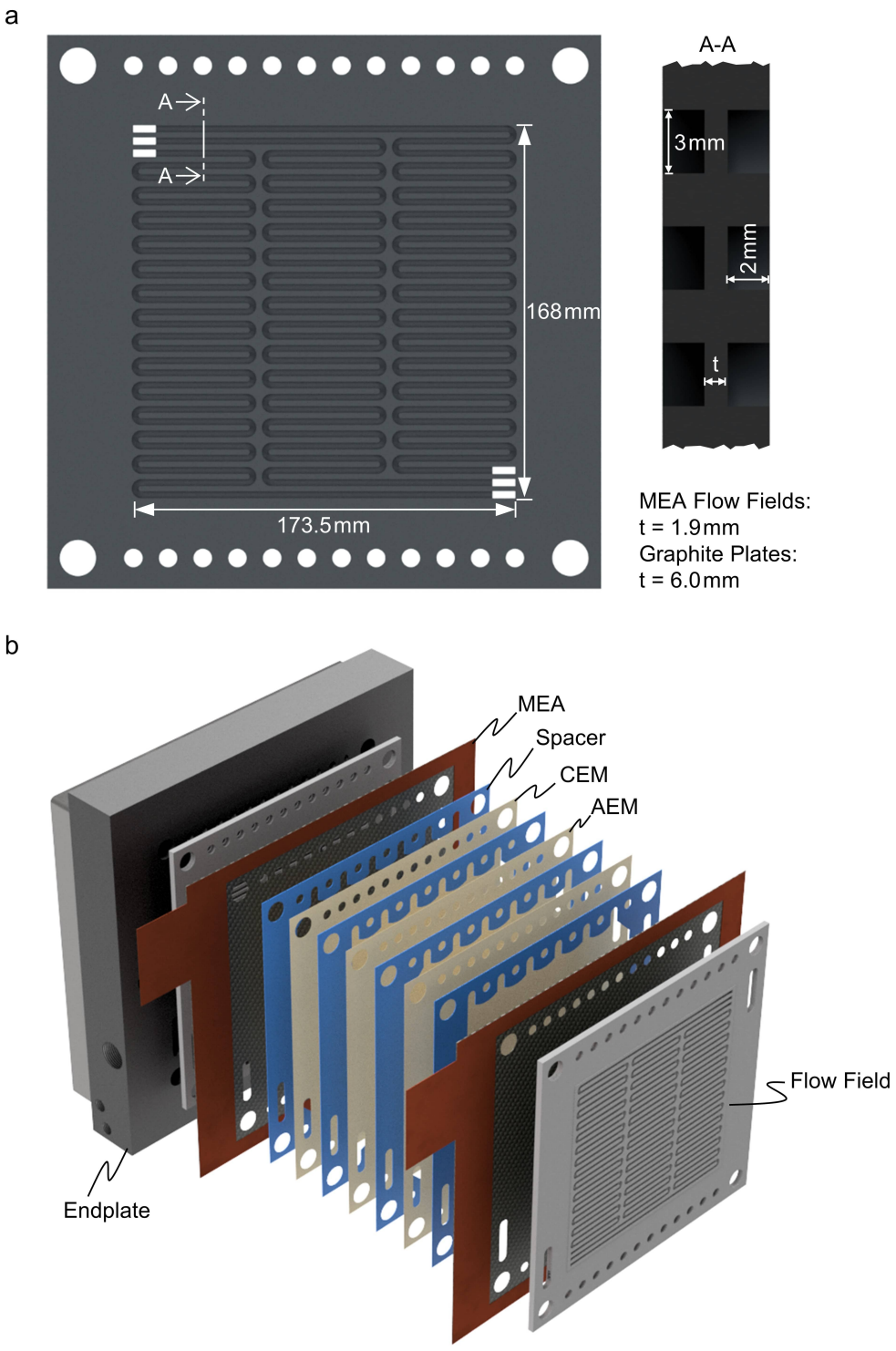

Figure 3.4: (a) Flow field with three channels for the flow electrode on both sides. The same geometry is used for flow fields made from graphite plates and for polymeric flow fields employed in MEA modules. The only difference is the thickness t of the midsection. (b) One stacking unit of the MEA module.

	Flow Fields	Membranes			Spacers
		MEAs	CEMs	AEMs	
GP 2 SU	3	0	6	4	8
MEA 2 SU	3	4	2	4	8
MEA 20 SU	21	40	20	20	80
Supplier	in-house	fumatech			fumatech Deukum
Specification	3D-printed or milled	FKS-30	FKS-130	FAS-130	ED-320

Table 3.1: Overview of materials used to construct the FCDI modules.

nels on each side of the flow field. These channels are each 3 mm wide and 2 mm deep. Next to the current collectors were cation-exchange membranes (CEM). CEMs for the MEAs were FKS-30 (Fumatech BWT GmbH). Reinforced FKS-130 membranes (Fumatech BWT GmbH) were used for the graphite plates. The middle CEM of a SU in both modules was an FKS-130 and the AEMs were FAS-130. ED-320 spacers from Fumatech BWT GmbH or Deukum GmbH were used. Polyoxymethylene end plates and steel frames were used to clamp the modules using four M14 screws. Fig. 3.4 (b) shows the assembly of one stacking unit of the module with MEAs.

3.2.2 Experimental Procedure

The experiments were carried out in continuous operation in short-circuited closed cycle mode, with the cations transported via the flow electrode. All experiments were conducted in constant voltage operation. The feed solutions were prepared by dissolving $60\,\mathrm{g\,L^{-1}}$ sodium chloride (VWR International GmbH) in ultrapure water. The same solution was also used for the flow electrode, which was prepared by suspending $15\,wt\%$ activated carbon powder (Carbopal SC11PG, Donau Carbon GmbH) in the solution. The flow electrode was stirred at least 12 h before use. In all experiments, an ISMATEC Flowmaster FMT-300 peristaltic pump (Cole-Parmer Instrument Company LLC.) conveyed the flow electrode through the modules. Due to

the size difference between the 2 SU modules and the 20 SU module, different pumps for the feeds and different power supplies were used. For the experiments with the 2 SU modules, an ISMATEC Reglo ICC (Cole-Parmer Instrument Company LLC.) peristaltic pump was used for the diluate and concentrate feeds. The voltage was applied to the module with a Keysight E3644A (Keysight Technologies Inc.) power source. For the experiments with the 20 SU module, a Masterflex EasyLoad 2 (Cole-Parmer Instrument Company LLC.) was used for the feeds, and a Keysight N5743A (Keysight Technologies, Inc.) power source was used to apply the voltage. The feed flow rates of diluate $V_{F,D}$ and concentrate $V_{F,C}$ were varied in the experiments. Outlet conductivities were monitored with Knick SE 615/1MS conductivity probes (Knick Elektronische Messgeräte GmbH & Co. KG); pH was monitored with Knick SE 102-MS pH sensors. Data from the conductivity and pH probes and power supplies were acquired and logged with a setup supplied by ZUMOLab GmbH.

All experiments were run until a steady-state was reached for the outlet conductivities in each of the compartments. Then, inlet and outlet mass flows were measured by taking samples and weighing the mass difference. The density of the samples was measured (Densito 30PX, Mettler-Toledo International Inc.), allowing for the calculation of exact volumetric flow rates from the ratio of mass flow and density. A correlation between density and sodium chloride (NaCl) concentration (see Appendix) was used to calculate the concentrations from the measured density. To verify the validity of this correlation, some samples were additionally investigated with ion chromatography (930 Compact IC Flex, Deutsche METROHM GmbH & Co. KG. Anion column: Metrosep A Supp 7 - 250/4.0. Cation column: Metrosep C 6 - 250/4.0). The deviation between the ion chromatography results and the correlation results was in the range of $\pm 5\,\%$. For each module, at least three experiments were performed and included in the evaluation. The metrics used for the comparison of the FCDI experiments are given in Eq. 2.5 and Eq. 2.6. The number of cell pairs $n_{cp} = 2$ is used. The total membrane area $A_{mem,tot}$ can be calculated from the area of one membrane $A_{mem} = 320\,\mathrm{cm}^2$

and the number of stacking units n_{su} according to Eq. 3.5.

$$A_{mem,tot} = n_{su} \cdot (2 \cdot n_{cp} + 1) \cdot A_{mem} \tag{3.5}$$

3.3 Results and Discussion

3.3.1 Two Stacking Units

In a first step, FCDI experiments were performed to compare the module with graphite plates (A320 GP 2 SU) and the module with membrane-electrode assemblies (A320 MEA 2 SU). The feed concentrations for both diluate and concentrate were $c_{Feed} = 60\,\mathrm{g\,L^{-1}}$. The feed flow rates of diluate and concentrate were set to $V_{F,D} = V_{F,C} = 3\,\mathrm{mL\,min^{-1}}$ per SU, giving a total of $6\,\mathrm{mL\,min^{-1}}$ (or $8.64\,\mathrm{L\,d^{-1}}$) for both diluate and concentrate. This resulted in a pressure loss of $\Delta p = 0.04\,\mathrm{bar}$ over the module. For the flow electrode $V_{FE} = 2.4\,\mathrm{L\,min^{-1}}$ was chosen to achieve a flow rate of $200\,\mathrm{mL\,min^{-1}}$ for each flow field channel. This flow rate was established as a safe flow rate to prevent clogging in past experiments. A cell voltage of $1.2\,\mathrm{V}$ was applied to the module. As shown in Fig. 3.5, the current efficiencies for both modules were close to unity; the ASTRs were between 1.0–$1.2\,\mathrm{\mu mol\,min^{-1}\,cm^{-2}}$, which is within the typical range reported for FCDI systems in literature [Zhan2021]. However, this is lower than the ASTR of a 2 SU module with $40\,\mathrm{cm^2}$ membranes shown as a reference. This could be caused by an uneven distribution of the feed between the spacers in the module. The spacers for the FCDI modules are designed for use in an ED-320 module. Because Electrodialysis (ED) is typically operated in batch mode, the flow rates of the feeds in the spacers are higher than those reached in continuous single-pass FCDI experiments. The low flow rates in FCDI experiments might favor uneven distribution.

The ASTR of the MEA module is higher than that of the graphite module. This could be due to the thinner FKS-30 membranes used for MEAs. In particular, the area of the interface between the current collector and the flow electrode (which is more than twice the area for the graphite plate) does not

affect the ASTR. This was already documented in earlier work [Linn2020]. The topic is addressed in more depth in the evaluation of current collector architectures in Chapter 5.

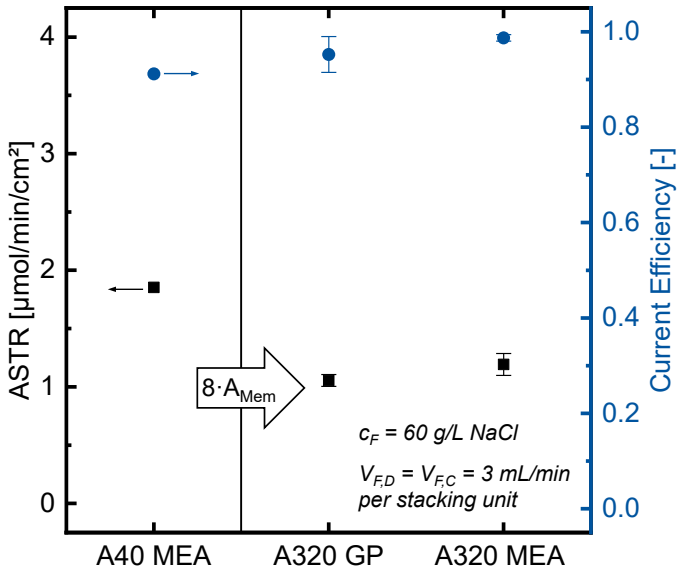

Figure 3.5: ASTR and CE of the A320 2 SU modules, results of a lab-scale A40 2 SU MEA module are given for reference [Linn2022].

The low voltages at the electrodes render FCDI stacking more complicated than stacking of ED modules. Therefore, experiments with an increased voltage are conducted to test the possibility to increase the treatment capacity of FCDI with higher voltages. The results are shown in Fig. 3.6. Filled symbols are used for the A320 MEA 2 SU module, open symbols are used for the A320 GP 2 SU module. The current efficiencies are close to unity for both modules at the voltages of 1.2 V and 2.0 V. At the initial voltage of 1.2 V, the MEA module shows a lower ASTR with 1.07 µmol min^{-1} cm^{-2} compared to 1.11 µmol min^{-1} cm^{-2} for the GP module. This is opposed to the results presented in Fig. 3.5 and shows the deviations that occur in the experiments. At higher cell voltages, the ASTR of the MEA module is higher. For the MEA module the 67 % increase in voltage yields a 50 % improved ASTR. The normalized concentrations for the experiments are plotted in Fig. 3.6 (b). Here, the A320 GP 2 SU module performs slightly better at both tested voltages, reaching higher concentrate concentrations and lower diluate concentrations. This is likely caused by lower water trans-

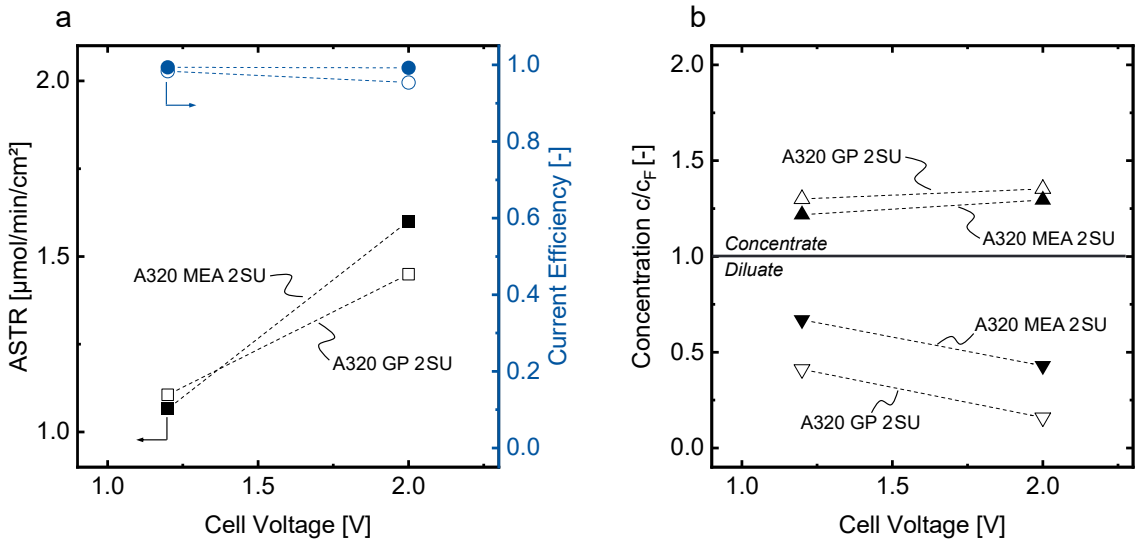

Figure 3.6: Impact of increased voltages for the A320 2 SU modules.

port across the thicker membranes used in the A320 GP 2 SU module. The results show that cell voltages above 1.2 V can increase the current in FCDI modules, leading to higher ASTRs and better desalination and concentration. The effect on the normalized diluate concentration is greater than on the normalized concentrate concentration. This is due to the relationship between ion movement and water crossover, described in Chapter 2.5.5.

Studies in literature document lower current efficiencies at elevated voltages due to faradaic reactions at the electrodes [Lian2017]. In our experiments, the pH of the concentrate and diluate produced is not constant, as shown in Fig. 3.7. The data are the result of current-voltage curves measured for the A320 MEA 2 SU and A320 GP 2 SU modules. The voltage is increased stepwise from 1.2–2.0 V and the pH of diluate and concentrate at the module outlets is measured. Interestingly, the pH of both diluate and concentrate increases for the A320 MEA 2 SU module, while decreasing trajectories are measured for the A320 GP 2 SU module. The cause of the different behavior is unclear and was not further investigated in the scope of the tests presented here. Overall, the trajectories allow the conclusion that faradaic reactions occur either at the current collector surfaces or the surfaces of the activated carbon particles. In some cases, the increase in current and treatment capacity could justify operation at high voltages.

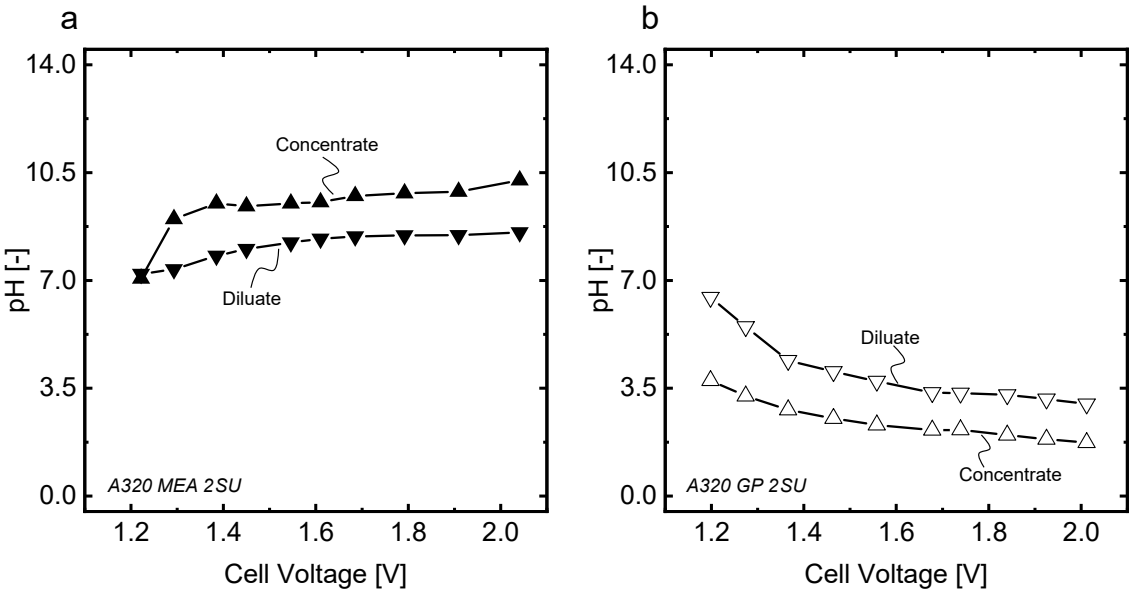

Figure 3.7: Trajectories of pH for Diluate and Concentrates from current-voltage curves with voltages greater than 1.2 V. (a): A320 MEA 2 SU module, (b): A320 GP 2 SU module.

However, there are also applications in which pH-sensitive media are handled. In this case, a low operating voltage that avoids a pH shift is an advantage of FCDI over ED. One possible application for pilot-scale FCDI modules is the concentration of wastewater containing fluoride (see Chapter 4). Here, acidic conditions must be avoided to prevent the formation of hydrofluoric acid. Also, an increase in pH should be avoided, as the next treatment step is not adjusted to basic pH. Therefore, within the scope of this chapter, no further experiments at voltages above 1.2 V are conducted. Furthermore, the results in Chapter 4 demonstrate that elevated voltages are unfavorable in a system with fluoride and nitrate, due to competitive transport between the different anions.

In the FCDI experiments shown in Fig. 3.5, the A320 MEA 2 SU module performs slightly better than the A320 GP 2 SU module. Furthermore, it has two additional advantages that are crucial for system scale-up: it can be built without the cost-intensive milling of flow channels in graphite plates, saving cost and allowing for a thinner design. In our case, the thicknesses of the two stacking units are 35 mm for the A320 GP 2 SU and 24 mm for

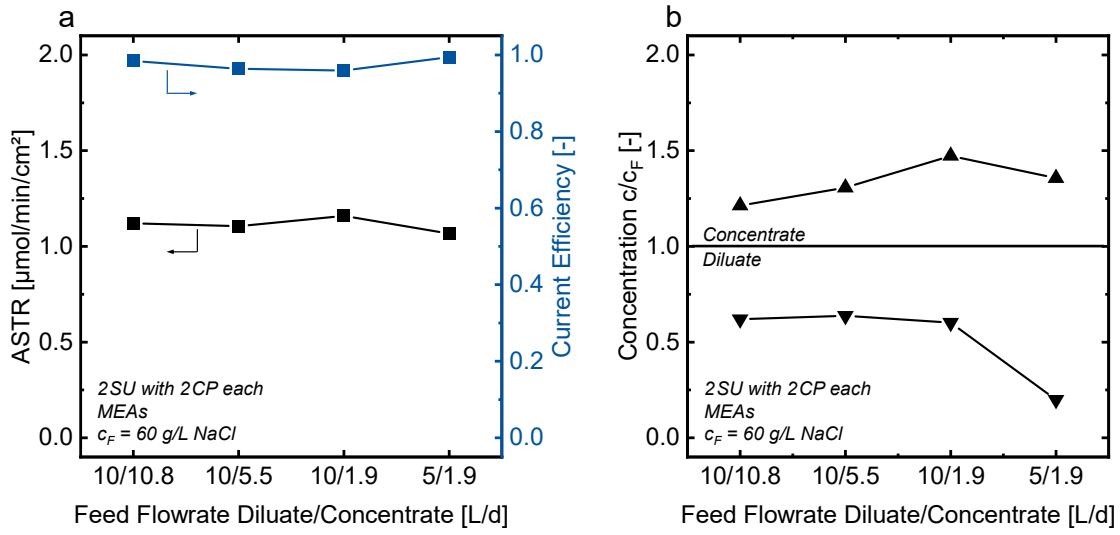

Figure 3.8: (a): ASTR and CE of A320 MEA 2SU module at varying flow rates for diluate and concentrate. (b): Normalized concentrations of A320 MEA 2SU module at varying flow rates for diluate and concentrate.

the A320 MEA 2 SU module. The thickness of stack design is certainly irrelevant for lab-scale systems but becomes essential when considering industrial applications with large stacked modules.

Due to its advantages, the A320 MEA 2 SU module was further investigated by varying the feed flow rates. Fig. 3.8 (a) shows ASTRs and CEs from this set of experiments. Fig. 3.8 (b) shows the corresponding normalized concentrations. In all experiments, the current efficiency is close to unity, and the ASTR varies between $1.06\,\mu mol\,min^{-1}\,cm^{-2}$ and $1.16\,\mu mol\,min^{-1}\,cm^{-2}$. This confirms the results from the initial experiment shown in Fig. 3.5. Initially, the flow into the diluate channel was kept constant at $10\,L\,d^{-1}$, and the flow rate in the concentrate channel was varied from $10.8\,L\,d^{-1}$ to $5.5\,L\,d^{-1}$ to $1.9\,L\,d^{-1}$. The normalized diluate concentration (c_D/c_F) remains almost constant, but c_C/c_F increases from 1.21 to 1.47. In single-pass operation, the lower flow rates correspond to a longer residence time in the module; therefore, higher concentrations are reached. For the last data point, the concentrate flow rate was kept constant and the diluate flow rate was reduced from $10\,L\,d^{-1}$ to $5\,L\,d^{-1}$. The longer residence time of the diluate led to better desalination. The normalized diluate concentration decreased from 0.60 to 0.20. At the same time, c_C/c_F reduced from 1.47 to 1.36 since the

higher concentration difference between the concentrate and the diluate channel led to a higher osmotic water crossover. High desalination (salt removal up to 80 %) can be reached, but the degree of concentration is limited. This is mainly due to an increase in the water crossover between the diluate and concentrate channels.

Water crossover can be divided into water transported in the hydration shells of the ions crossing the IEMs and water crossover due to osmotic effects. In the single-module architecture, the diluate and concentrate channels are separated only by the AEM in the middle. As pointed out in Chapter 2.5.3 this leads to greater osmotic water crossover at high concentration differences. Although this architecture has been used before to reach high concentration differences between diluate and concentrate, this is only possible at very low feed flow rates [Romm2020b]. In the scope of this study, our aim is to obtain higher flow rates. In applications that demand high concentration differences and high flow rates, a two-module layout should be considered in the future. In a two-module layout, the diluate and concentrate channels are separated from each other, and osmotic water transfer occurs only via the flow electrode. The salt concentration in the flow electrode can be set as the average of the mean concentrations in the diluate and concentrate to keep the osmotic effects in both modules as low as possible.

3.3.2 20 Stacking Units

The feed flow rates of the A320 MEA 2 SU module are still low when considering the application at pilot plant scale. To increase the treatment capacity and allow demonstration of FCDI at the pilot scale, the number of stacking units was increased to 20 SU. The aim is to investigate the metrics of an FCDI module with many flow channels in a parallel connection. Possible problems can be an uneven distribution of the flow electrode to the flow fields, leading to clogging in regions of low flow velocities. This problem is potentially aggravated by the pump used to supply the module with the flow electrode. In our test, the peristaltic pump, at its highest pump setting,

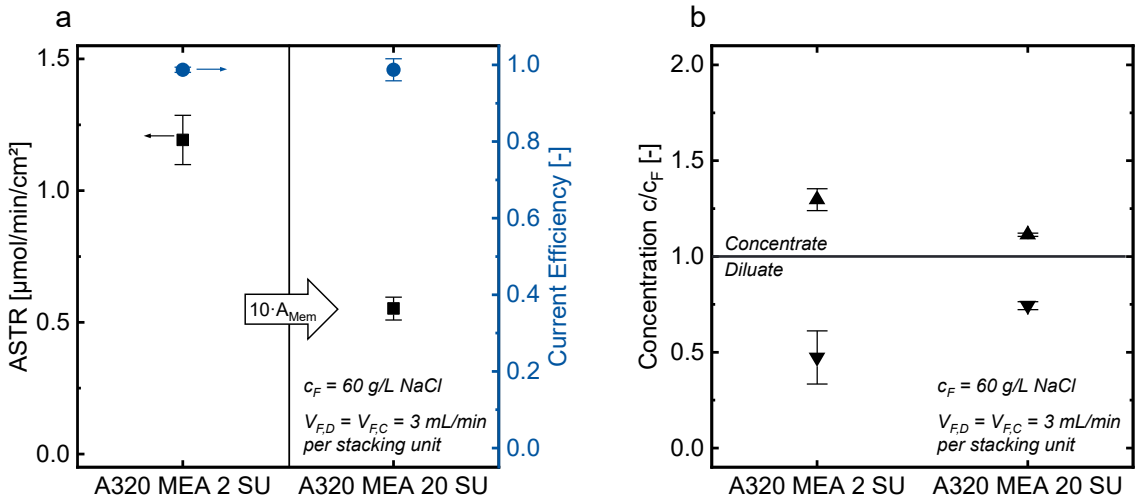

Figure 3.9: (a): ASTR and CE of A320 MEA 2 SU and A320 MEA 20 SU modules. (b): DD and CD of A320 MEA 2 SU and A320 MEA 20 SU modules.

was only able to pump $60\,\mathrm{mL\,min^{-1}}$ per flow channel through the module, not the $200\,\mathrm{mL\,min^{-1}}$ used in tests with the 2 SU modules. This change in experiment parameters has to be considered in the following comparison. The feed flow rates for diluate ($V_{F,D}$) and concentrate ($V_{F,C}$) were increased by a factor of 10 to keep the flow rate per SU constant. Fig. 3.9 shows the results from the experiment with the A320 MEA 20 SU module compared to the A320 MEA 2 SU module.

The desalination experiments with the A320 MEA 20 SU module were conducted with feed flow rates of $60\,\mathrm{mL\,min^{-1}}$, corresponding to $86.4\,\mathrm{L\,d^{-1}}$. This allows comparison with the MEA 2 SU module since the feed flow rate per stacking unit was kept constant ($3\,\mathrm{mL\,min^{-1}}$). Fig. 3.9 (a) shows lower ASTR at constant high current efficiencies. The ASTR of $0.55\,\mathrm{\mu mol\,min^{-1}\,cm^{-2}}$ is still in the range reported for FCDI systems in literature [Zhan2021]. However, for the high feed concentrations (and high conductivities of the feeds), the ASTR is certainly low. Similarly, the concentration differences reached are relatively small, as shown in Fig. 3.9 (b). The concentration on the diluate side reduces from $60\,\mathrm{g\,L^{-1}}$ to $45\,\mathrm{g\,L^{-1}}$. On the concentrate side, the concentration increases from $60\,\mathrm{g\,L^{-1}}$ to $67\,\mathrm{g\,L^{-1}}$. The most likely causes for the decrease in ASTR are an uneven distribution of feed solutions to the spacers in the module, which might lead to non-wetted membrane areas in the

cell. This problem is aggravated by a higher number of stacked units, as there are more possibilities for inadequate flow.

In some applications, the concentration differences achieved in our experiments might suffice to achieve the desired separation characteristics. However, the goal remains to reach high concentrations with FCDI. To achieve higher concentration differences, batch operation of the A320 MEA 20 SU module with higher flow rates might be beneficial. Using flow rates within the range used in ED should prevent uneven distribution of feeds. Batch operation of this module with real-word wastewater feed is described in Chapter 4. A batch system with multiple modules would also allow the prevention of high concentration differences between diluate and concentrate, which lead to high osmotic water crossovers over the central AEMs separating diluate and concentrate compartments. Contrary to initial expectations, clogging was not an issue in the experiments with this module. A post-experiment analysis showed clogging in only one of the flow fields in the middle of the stack. All flow fields had black residues of activated carbon, indicating that the flow electrode was flowing through all flow fields. However, the flow velocities in the individual flow fields might vary, which could also explain the reduced ASTR.

To evaluate the viability of the scale-up, it is helpful to view the salt transport and the scale of the modules in reference to the initial lab scale. The initially used FCDI modules had one stacking unit with one cell pair and the membrane cross-sectional area was $40\,\mathrm{cm}^2$ [Linn2022]. This leads to a total membrane area of $A_{mem}(A40\ MEA) = 120\,\mathrm{cm}^2$. In Fig. 3.10 this membrane area and the salt transport $\dot{m}_{NaCl}(A40\ MEA)$ reached with these modules are used to normalize the membrane areas and salt transport achieved with the modules investigated in scale-up. In this diagram, the dashed line at the 45° angle marks the upper limit of salt transport that can be expected for modules with a larger membrane area. It represents a parallel connection of identical lab-scale FCDI modules. It is unlikely that a module with stacking units would reach higher salt transport since this would mean that the membrane area in a stack is better utilized than in a single cell at lab

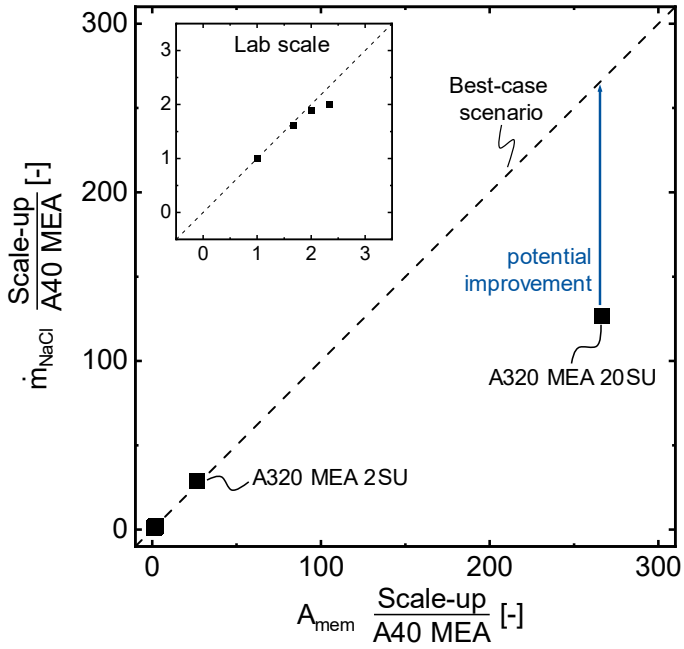

Figure 3.10: Salt mass flow over installed membrane area, normalized by the inital values for a lab-scale A40 MEA module: For lab-scale systems (small diagram, see [Linn2022]) and for the scale-up systems discussed in this work.

scale. This is not typical for membrane processes. Results on lab scale (see small graph) were obtained by using multiple cell pairs and stacking units of the A40 MEA module. These results and the results from the A320 MEA 2 SU module lie on the 45°-line or close to it. This means that stacking with lab-sized modules and the scale-up by increasing the membrane cross-section worked as well as could reasonably have been expected. However, the 20 SU module is located below the trendline, showing the potential to improve modules with a better stacking concept, for example, by tuning the distribution of feeds and flow electrode to the individual stacking units. When moving from a lab-scale A40 FCDI module (as shown as reference in Fig. 3.5) to the A320 MEA 20 SU module, the active membrane area increases by a factor of 267, while the salt mass flow only increases by a factor of 127. This difference seems significant at first, yet losses of specific treatment capacity are common for the scale-up of membrane processes by stacking. This is known, for example, from the scale-up of systems for Reverse Electrodialysis, where the power output of the system also does not increase linearly with the number of cell pairs in a stack [Kim2021].

In conclusion, the limiting factors for the scale-up of FCDI are (a) the low maximum voltage of 1.23 V, (b) water crossover over the membranes, especially over the AEM between diluate and concentrate channels and (c) the suspected uneven distribution of the feed in the module. We already showed that higher voltages are possible at the cost of increased pH shifts. Further research at elevated voltages could bring FCDI closer to ED, as already proposed by Ma et al. [Ma2020b]. Water crossover can be reduced by coating IEMs [Romm2021] or by separating concentrate and diluate in a two-module layout, as detailed above. The distribution of the feeds to the spacers in the module needs to be re-evaluated at high feed flow rates in batch operation. The next steps in scale-up could also be taken by building more modules. If multiple A320 MEA 20 SU modules are connected in parallel in a numbering-up approach, no further decrease in specific treatment capacity is expected as the distribution of the feeds and the flow electrode is handled by external piping, allowing better control.

3.4 Conclusion

To demonstrate the advantages and disadvantages of FCDI, the process needs to be investigated on an industrially applicable scale. This chapter demonstrates scale-up via cell stacking to bring FCDI single modules to pilot scale (TRL 5). First, the membrane area of the lab-scale modules was increased by choosing larger membranes. Then, the stacking of repeating units was used to further increase the treatment capacity of the modules. Stacking multiple flow electrode channels kept the voltage drop between the membrane-electrode assemblies low. This enables a lower energy demand than Electrodialysis (ED), as demonstrated in a thought experiment. This advantage comes at the price of a lower ion flux per membrane area. The comparison between ED and FCDI leads to a trade-off between lower invest cost (ED, since less membranes are needed) and lower operational cost (FCDI, since less energy is needed). However, this comparison does not include additional energy (e.g., for pumps) and needs to be verified in

a real-world scenario. As a result of this Chapter, a stacked module with an active membrane area of $3.2\,m^2$ was built and reached an average salt transfer rate (ASTR) of $0.55\,\mu mol\,min^{-1}\,cm^{-2}$ at high current efficiency, allowing us to conduct desalination and concentration experiments with feed flow rates greater than $80\,L\,d^{-1}$. This module is an important step in the scale-up of FCDI, as it can serve as a building block for larger modules and applications. Due to the modular design, multiple modules can be connected together. Future work should investigate and optimize the distribution of the diluate and concentrate feed to the stacking units in the module. The application of one stacked module in a pilot plant handling industrial wastewater is detailed in Chapter 4.

4 FCDI in Real-World Application

Parts of this chapter have been published as:

Niklas Köller, Dustin Roedder, Christian J. Linnartz, Mark Enders, Florian Morell, Patrick Altmeier, Matthias Wessling

Recovery of nitrate and fluoride salts from stainless steel pickling wastewater with flow-electrode capacitive deionization, Journal of Hazardous Materials Letters, 2025

DOI: 10.1016/j.hazl.2025.100148

4.1 Introduction

This chapter details the application of the Flow-electrode Capacitive Deionization (FCDI) process to a real-world salt removal and recycling task. The conducted work was part of the research project "Nitratkreislaufführung bei der Behandlung von Metalloberflächen durch Nutzung innovativer Techniken (NITREB)", sponsored by the German Ministry for Education and Research (BMBF). The scope of the project was the development of a new process to establish recycling loops for acids used in stainless steel pickling.

Stainless steel is a large-scale commodity product with a wide variety of applications. During production, stainless steel is handled at elevated temperatures (e.g., during casting or annealing). This causes the formation of an oxide scale layer and a chromium-depleted layer on the surface. These layers not only impair the optical properties of the surface but also reduce the resistance to corrosion. Steel pickling is used to achieve the desired qualities, by removing the surface layers and exposing the metal beneath [Li2003]. An important part of the pickling process is chemical pickling in acid baths. Hydrofluoric acid (HF) and nitric acid (HNO_3) are often used in these pickling baths [Li2005]. The spent acids are neutralized with alkaline solutions, such as calcium hydroxide, generating salt solutions. If HF and HNO_3 are used together in the pickling bath, calcium fluoride precipitates from the solution due to its low solubility limit, but the nitrate content of the effluent remains high. Therefore, the effluent cannot be discharged into the environment because the high nitrate content would cause increased eutrophication. Thus, wastewater treatment in the form of denitrification at a wastewater treatment plant or by an internal process in the steel pickling plant is necessary. In an ideal case, this wastewater treatment process would also enable the regeneration of nitrates and fluorides in the form of HF and HNO_3, resulting in a lower environmental impact and an economic benefit caused by lower cost for chemicals [Negr2001]. Several different membrane-based solutions for the recycling of acids from pickling baths are known in literature [Agra2009]. Notably, Negro et al. used a combina-

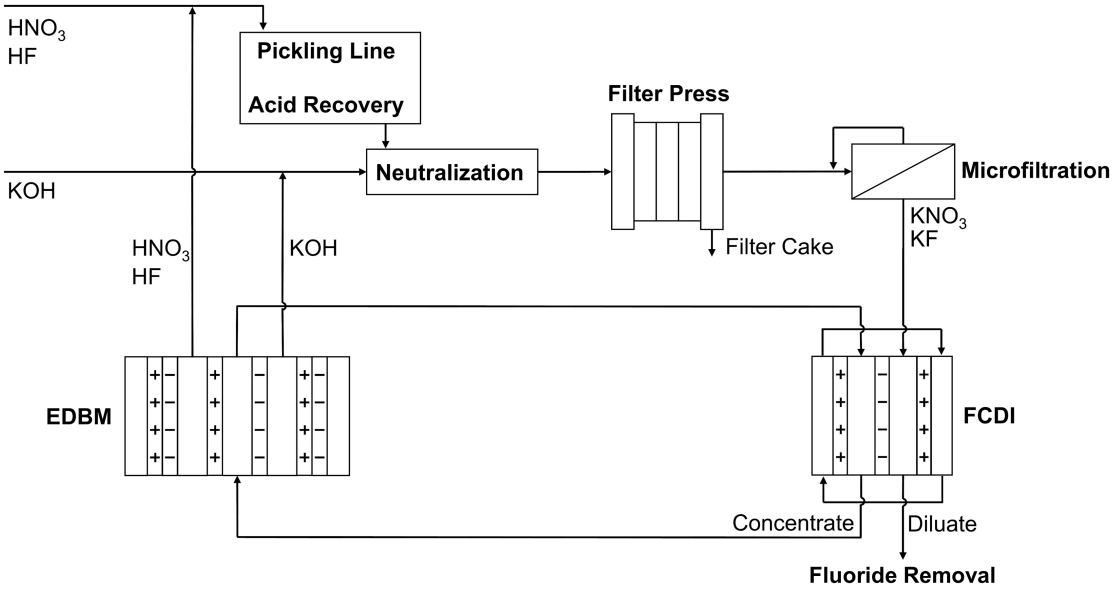

Figure 4.1: Simplified flowchart of the NITREB process for the recycling of HF and HNO_3. This flowchart does not include chromium detoxification and filter cake post-treatment.

tion of Electrodialysis (ED) and ED with bipolar membranes (EDBM) for the concentration and splitting of depleted salt solutions [Negr2001]. Based on their work, a new treatment process was proposed for the project NITREB. Fig. 4.1 shows a simplified flowchart of this treatment process.

The recycling process starts with the neutralization of the spent acids from the pickling line. In this case, the neutralization is done with potassium hydroxide (KOH). Due to the high solubility limits of potassium fluoride (KF) and potassium nitrate (KNO_3) all salts remain in solution. The salt solution is then treated with a filter press and microfiltration to remove larger impurities, which could cause problems in the following process steps. Electromembrane processes are used for the desalination and concentration of the wastewater stream. In this process, the wastewater desalination and concentration step is done with FCDI. In the electric field, salts are transported from the wastewater to a concentrate solution. The aim is to produce a diluate with a nitrate concentration below the regulatory limit for discharge to the runoff ditch. The remaining fluoride in the diluate must be removed by precipitation before discharge. Since this leads to the loss of some fluoride

and nitrate, the aim is to transport as much as possible to the concentrate solution. In the next step, the concentrate is treated with EDBM. EDBM is briefly introduced in Chapter 2.1 as a process to produce acids and bases from salt solutions. In this process, water is split into H^+-ions and OH^--ions, allowing the production of the acids HF and HNO_3 and the base KOH. HF and HNO_3 can be recycled to the pickling line and KOH to the neutralization step. The NITREB process lowers the required amount of discharged nitrates and also offers a strong economic incentive since the amounts of fresh HF, HNO_3, and KOH are lowered. The aim of the research project was to establish this process at pilot plant scale with a treatment capacity of 50–80 $L\,h^{-1}$.

There is no literature on FCDI applied to a similar process, and our research group had only limited experience in setting up FCDI with a feed containing two different salts. Therefore, the primary objective was to test the applicability of FCDI on a lab scale. For this reason, this chapter first details the tests conducted on the lab scale before moving on to the pilot plant application of an FCDI module at the stainless steel treatment plant. The scale-up of FCDI modules is described in Chapter 3. Overall, this chapter aims to highlight the adjustments needed to tailor the FCDI process to a new feed wastewater and to showcase an application on pilot scale.

4.2 Experimental

4.2.1 Lab-scale Experiments

Lab-scale tests were carried out in continuous single-pass operation. An FCDI single module with total membrane area $A_{mem,tot} = 300\,cm^2$ was used [Romm2015]. The module consisted of one stacking unit $n_{su} = 1$ with one cell pair $n_{cp} = 1$. Current collectors made of graphite (180 mm × 180 mm × 10 mm, MR40, Müller & Rössner GmbH & Co. KG) were used. Flow-electrode channels with 18 turns (3 mm × 2 mm and 2000 mm total length) were milled into the current collectors. Membrane spacers (ED-100, thickness 500 µm, Fumatech BWT GmbH) were used for the concentrate and

diluate channels between ion-exchange membranes. One cation-exchange membrane (Fumasep FKS, 75 µm PET-reinforced, Fumatech BWT GmbH) was placed adjacent to each current collector. An AEM (Fumasep FAS, 75 µm PET-reinforced, Fumatech BWT GmbH) separated the two flow channels. End plates were used to clamp the modules and provide connections for the flow electrode channels and the diluate and concentrate channels. Sealings made from ethylene propylene diene monomer (EDPM) rubber were used between the current collectors and the neighboring layers. After each module assembly, a leakage test was performed by recirculating a defined amount of ultrapure water in each flow channel for at least 3 h.
The two feed solutions for diluate and concentrate were pumped by a peristaltic pump (REGLO ICC Digital Peristaltic Pump 2-Channel, Cole-Parmer Instrument Company LLC.). The flow electrode was continuously stirred with a magnetic stirrer (VS-C4, VWR International GmbH) in a beaker and pumped through the module with a second peristaltic pump (Cole Parmer Master Flex L/S, Cole-Parmer Instrument Company LLC.). Voltage was applied to the module with a power supply, which also measured the current (E3644A, Keysight Technologies Inc.). The voltages used in the individual experiments are given in the results section. Conductivity probes were used to measure the conductivity of the outgoing diluate (SE 615/1-MS, Knick Elektronische Messgeräte GmbH Co. KG) and concentrate (LTC 0,35/23, Xylem Analytics Germany Sales GmbH & Co. KG) streams. Data from the conductivity probes and power supply were acquired and logged with a setup from ZUMOLab GmbH.
At the time of lab-scale testing, the neutralization process, filter press, and microfiltration for the NITREB process were not yet installed in the stainless steel treatment plant. Therefore, most of the experiments could not be carried out with real wastewater. Instead, a model wastewater was used. The concentrations of potassium nitrate (KNO_3) and potassium fluoride (KF) were based on samples from small-scale neutralization tests at the stainless steel treatment plant. The diluate feed solution consisted of 38.03 g L^{-1} KNO_3 (Potassium Nitrate 99 %, Carl Roth GmbH + Co. KG) and 33.38 g L^{-1} KF (Potassium Fluoride 99 %, Carl Roth GmbH + Co. KG)

dissolved in ultra-pure water. These concentrations should resemble an average of the salt concentrations found in the wastewater after the neutralization step. Higher concentrations were used for the concentrate feed solution ($83.67\,\mathrm{g\,L^{-1}}$ KNO_3 and $73.44\,\mathrm{g\,L^{-1}}$ KF) since the concentrations in the loop between FCDI and EDBM were expected to be at this level during operation of the NITREB process. The flow electrode was prepared by suspending $15\,wt\%$ activated carbon powder (Carbopal SC11PG, Donau Carbon GmbH) in salt solutions with varying concentrations of KNO_3 and KF.

Sample concentrations in all experiments were measured by ion chromatography (930 Compact IC Flex, Deutsche METROHM GmbH & Co. KG. Anion column: Metrosep A Supp 7 - 250/4.0. Cation column: Metrosep C 6 - 250/4.0). Sample densities were measured with a handheld densitometer (Densito 30PX, Mettler-Toledo International Inc.). The metrics used to describe the results are detailed in Chapter 2.5.5. Here, the total average salt transfer rate (total ASTR) is used to describe the total ion transport of both salts.

4.2.2 Pilot-scale Experiments

Pilot-scale testing was performed with one module with $3.2\,\mathrm{m^2}$ active membrane area. The design of the pilot-scale modules and the initial tests that were used to validate the performance of these newly developed modules are given in Chapter 3. The module was operated with a custom-made FCDI pilot plant (SIMA-tec GmbH). The plant features three batch tanks. The batch tank for the diluate has a volume of $60\,\mathrm{L}$, the concentrate batch tank has a volume of $35\,\mathrm{L}$, and the flow electrode batch tank has a volume of $75\,\mathrm{L}$. The flow electrode tank features a stirrer to keep the activated carbon suspended. Two gear pumps with flowrates $5\text{–}50\,\mathrm{L\,h^{-1}}$ are used to pump diluate and concentrate. For the flow electrode a peristaltic pump (Verderflex Dura 35, Verder Deutschland GmbH & Co. KG) with a flowrate $500\text{–}2500\,\mathrm{L\,h^{-1}}$ is used. A dosing pump enables the dosing of a salt solution or water to the flow electrode batch tank during operation. The FCDI

module is powered by a DC power source (Genesys ™ GEN 8-400, TDK-Lambda Germany GmbH) with a maximum voltage of 8 V and a maximum current of 400 A. An operation voltage of 1.2 V is used.
The flow rates of diluate and concentrate are measured at the inlet and outlet of the FCDI module, the flow rate of the flow electrode is measured only at the module inlet. Conductivities and temperatures are measured at the module inlet and outlet; pH of diluate and concentrate is measured at the outlet of the module. The plant is programmed to enable automatic continuous and batch operation. Automatic batch operation is used for the experiment described in this chapter. During batch operation, the flow rates of all streams are controlled and kept constant at predefined values. The target conductivities for diluate and concentrate are set, and the solutions are circulated through the module until the target conductivities are reached. Once the target of diluate or concentrate is reached, the plant automatically stops the voltage and empties the according batch tank. The solution is pumped into a storage tank and the batch tank is refilled with fresh feed solution. Then the voltage is restarted and a new batch begins. The plant program also features automatic cleaning and flushing steps, which are especially important for the flow electrode loop.
Pilot-scale tests were conducted on-site with neutralized and pretreated wastewater from the pickling line. The concentrations of KNO_3 and KF in the wastewater vary depending on the operation of the pickling line. During the experiments described in this chapter, the concentrations of the wastewater used as diluate feed were around $30\,g\,L^{-1}$ KNO_3 and $40\,g\,L^{-1}$ KF. This is a lower concentration of KNO_3 but a higher concentration of KF as in the lab-scale experiments. In pilot-scale tests, the loop between FCDI and EDBM is closed and the depleted salt solution from the EDBM is used as concentrate feed for FCDI. The concentrations were around $10\,g\,L^{-1}$ KNO_3 and $30\,g\,L^{-1}$ KF. Notably, this is significantly lower than the concentrations of concentrate feed solutions used in lab-scale experiments.

4.3 Results and Discussion

The experiments on the lab scale were aimed at evaluating the viability of the FCDI process for the given separation task. The objective was to remove 90 % of nitrate from the diluate. On the concentration side, the objective was to reach at least a concentration of 130 %. To achieve these goals, the FCDI process needed to be tailored to the specific feed solutions. Fig. 4.2 shows a flowchart diagram of the steps taken to tailor the FCDI process.

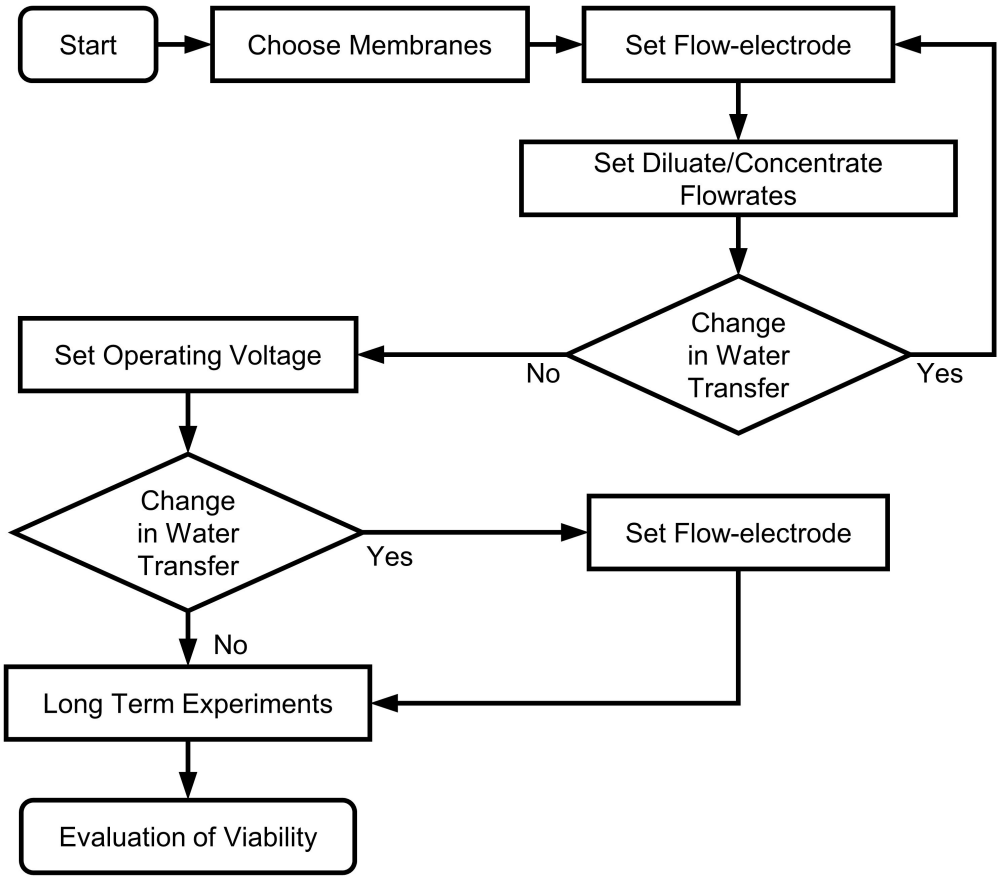

Figure 4.2: Flowchart of the adaptation steps to tailor the FCDI process to a new feed solution.

This flowchart is an outcome of the experiments presented in this chapter, as there was no prior experience tailoring the FCDI process in our research group. The first step should be the choice of ion-exchange membranes. The membranes must be stable at the pH of the feed solutions and should

allow for high ion transport. In some cases, selectivity between different ions might be desired. Information on the selectivity of ion-exchange membranes can be found in literature or be determined in first experiments. In this specific case, fumasep FAS and FKS-membranes (Fumatech BWT GmbH) were chosen based on previous experience with nitrate feed solutions [Linn2022]. In the next step, the concentration of electrolytes in the flow electrode should be set to minimize osmotic water transfer. This step should be repeated if any of the following steps lead to significant changes in water transfer.

4.3.1 Investigation of Flow Electrode

The flow electrode used in the FCDI process typically contains an electrolyte to increase its conductivity. Ideally, the salts used as background electrolytes are the same as those present in the diluate and concentrate feed streams, so that no impurities are introduced into the process by the electrolyte in the flow electrode. However, the concentration of the background electrolyte is also important. If the concentration is lower than the concentration in the neighboring channels, the flow electrode loses water due to osmotic water transport (see Chapter 2.5.3). If the concentration in the flow electrode is higher than in the neighboring channels, the osmotic water transport is directed into the flow electrode. The ideal case would be a flow electrode that is in equilibrium with the neighboring channels so that the water content in the flow electrode remains constant over time. This is impossible to achieve, as the flow electrode is in contact with both diluate and concentrate, which necessarily have different concentrations.
In the long-term operation of an FCDI process, the loss of water from the flow electrode is easier to control. Lost water can be added back to the flow electrode by hand or by a dosing pump. If the water content in the flow electrode increases, the activated carbon concentration decreases over time, and the FCDI process is hindered. The removal of water from the flow electrode is more complicated because it requires a filtration step to hold back the suspended activated carbon particles. For this reason, the

goal was to find a background electrolyte concentration that would cause a minimum amount of water loss. Different flow electrode compositions were investigated: since KF is toxic and also more expensive than KNO_3, the goal was to use only KNO_3 as salt in the flow electrode. The first experiment was conducted with a background electrolyte concentration of $c_{KNO_3} = 150\,\mathrm{g\,L^{-1}} = 1.48\,\mathrm{mol\,L^{-1}}$. Since the sum of salt concentrations in the diluate feed is $0.95\,\mathrm{mol\,L^{-1}}$ ($c_{KNO_3} = 0.38\,\mathrm{mol\,L^{-1}}$, $c_{KF} = 0.57\,\mathrm{mol\,L^{-1}}$) and in the concentrate $2.09\,\mathrm{mol\,L^{-1}}$ ($c_{KNO_3} = 0.83\,\mathrm{mol\,L^{-1}}$, $c_{KF} = 1.26\,\mathrm{mol\,L^{-1}}$), this is close to the average molar concentration of diluate and concentrate. This flow electrode was compared to a flow electrode with KNO_3 and KF. Here, both concentrations were the average of diluate and concentrate. Furthermore, the effect of sonication on the flow electrode with $c_{KNO_3} = 1.48\,\mathrm{mol\,L^{-1}}$ was investigated. The hypothesis was that sonication of the flow electrode for $1\,\mathrm{h}$ before the experiment would improve the mixing of the activated carbon particles and could improve the charge transport in the flow electrode. The membranes in these experiments were fumasep FAS-PET-75 and FKS-PET-75 (Fumatech BWT GmbH).

Fig. 4.3 (a) shows no significant improvement of ASTR for the sonicated flow electrode. The total ASTR as well as the individual ASTRs for KNO_3 and KF stay constant. These results also show the generally lower ASTR for KF. Fluoride ions are strongly charged and attract a high number of water molecules in their hydration shell. This hydration shell renders them less mobile than nitrate ions. Similar results can also be found in the literature on ED [Luo2018]; [Grze2020]; [Alia2021].
When the flow electrode with $c_{KNO_3} = 0.6\,\mathrm{mol\,L^{-1}}$ and $c_{KF} = 0.92\,\mathrm{mol\,L^{-1}}$ is used, the ASTR for KF increases, the ASTR for KNO_3 decreases. The total ASTR shows a slight increase. The presence of fluoride in the flow electrode apparently enhances the transport of fluoride between the diluate and concentrate. The total ASTR correlates well with the currents plotted in Fig. 4.3 (b). The right y-axis in Fig. 4.3 (b) shows the volume change of the flow electrode (ΔV). When the flow electrode is prepared with $c_{KNO_3} = 1.48\,\mathrm{mol\,L^{-1}}$ it experiences a net loss of water. When $c_{KNO_3} = 0.6\,\mathrm{mol\,L^{-1}}$ and $c_{KF} = 0.92\,\mathrm{mol\,L^{-1}}$ are used, the flow electrode gains

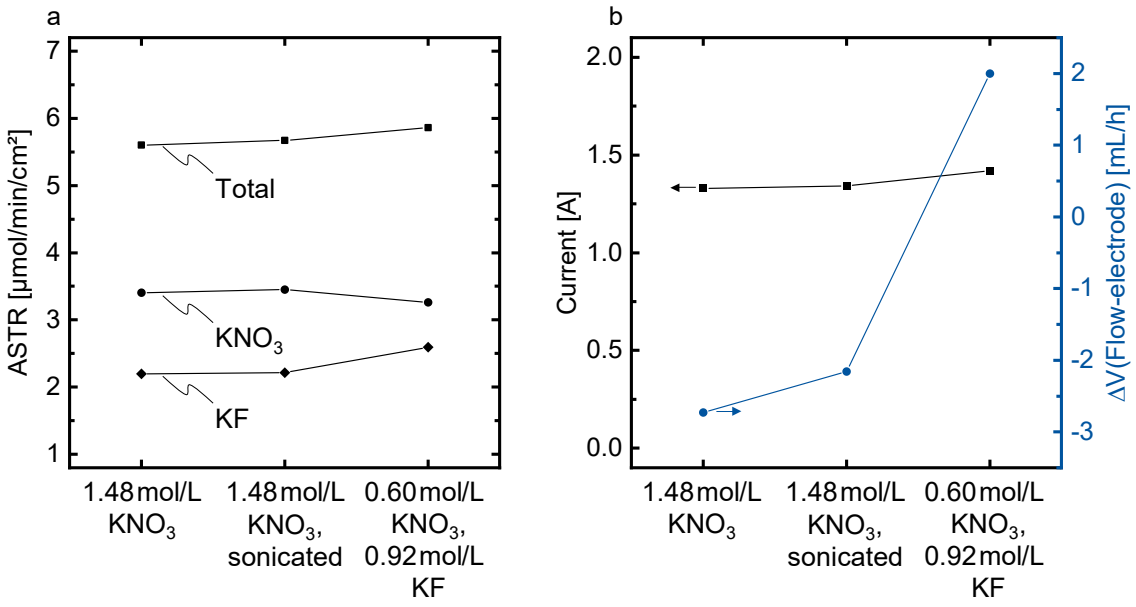

Figure 4.3: Influence of sonication and addition of KF in the flow electrode. Data points are connected by lines to guide the reader's eye.

water, even though there is only a small change in the ionic strength of the solution. On the basis of van't Hoff's law (see Chapter 2.1) the osmotic water transfer should remain constant. An explanation could be a change in the electrolyte concentration in the flow electrode. If nitrate ions are removed from the flow electrode and replaced by fluoride ions that transport more water in their hydration shells, an increase in volume will be observed. This phenomenon was not further investigated, since the flow electrode with $c_{KNO_3} = 1.48\,\mathrm{mol\,L^{-1}}$ was chosen for further experiments. The slightly lower total ASTR measured for this flow electrode is negligible. Using only KNO_3 in the flow electrode reduces the amount of KF needed in experiments and saves cost; a relevant factor from the perspective of FCDI scale-up.

4.3.2 Membrane Thickness

The transport of ions and water in electro-membrane processes are strongly influenced by the ion-exchange membranes [Pora2018]. We wanted to investigate the influence of membrane thickness on the FCDI

process. Doing this after setting the flow electrode is a deviation from the ideal flowchart in Fig. 4.2. Generally, the membranes should be chosen before the electrolyte concentration of the flow electrode is adjusted to avoid an additional loop in which the electrolyte concentration might need to be readjusted. In our investigation, the supplier and type of membrane were kept constant. Only the thickness of the middle membrane that separates the diluate and concentrate compartments was changed from a $d_{AEM} = 75\,\mu m$ thick FAS-PET-75 membrane to a $d_{AEM} = 130\,\mu m$ thick FAS-PET-130 membrane. The hypothesis was that the middle membrane would have the most influence on osmotic water transport since the concentration difference between diluate and concentrate is higher than between each of the channels and the neighboring flow electrode channel.

To allow a comparison of the two experiments, they were carried out with a constant current of $I = 1.6\,A$. In constant current operation, the ion transport is the same in both experiments. Therefore, changes in the outlet concentrations can be attributed to water transport. The diluate feed flow rate was set to $\dot{V}_{0,D} = 1.18\,mL\,min^{-1}$ and the concentrate feed rate to $\dot{V}_{0,C} = 0.5\,mL\,min^{-1}$. Fig. 4.4 (a) shows the ASTR with a membrane thickness of $d_{AEM} = 75\,\mu m$ and $d_{AEM} = 130\,\mu m$. The total ASTR and the individual ASTRs of KNO_3 and KF do not change with different membrane thicknesses. However, water transport is influenced by the change in membrane thickness. The right y-axis shows the quotient of salt transport and water transport: this metric increases from $0.29\,mg_{Salt}/mg_{H_2O}$ to $0.34\,mg_{Salt}/mg_{H_2O}$ with the thicker membrane. Since the salt transport (given by the ASTR) remains constant, this means that the water transport across the middle membrane is reduced. Fig. 4.4 (b) shows the effect on the concentrations of diluate and concentrate at the module outlet. The KNO_3 concentrations remain unchanged, and the concentration difference of KF increases slightly.

$$E_D = \frac{V \cdot I}{\dot{V}_{F,D}} \quad \left[\frac{kWh}{m^3}\right] \tag{4.1}$$

With the results from the experiments, the electrical energy demand per

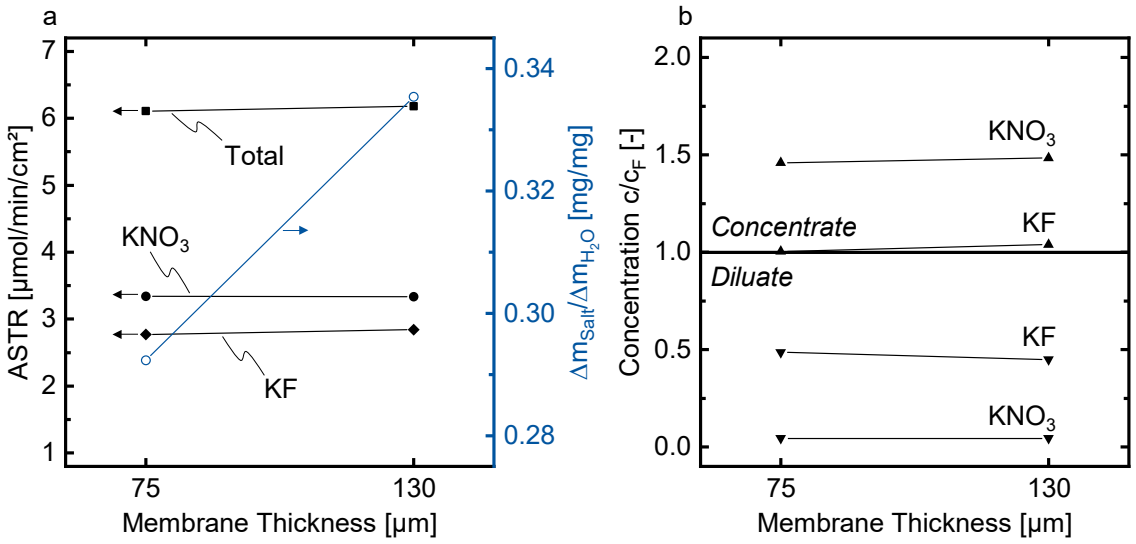

Figure 4.4: Influence of the thickness of the middle anion-exchange membrane on the salt and water transport in the FCDI module. Data points are connected by lines to guide the reader's eye.

cubic meter of treated diluate can be calculated according to Eq. 4.1. V is the voltage, and I is the current. The energy demand is normalized by the diluate feed flow rate $\dot{V}_{F,D}$. This metric is problematic when experiments with different outlet concentrations are compared. Furthermore, it does not include any additional energy (e.g., energy of the pumps in the experiment). However, it allows to characterize how much energy needs to be expended for the treatment of one cubic meter of diluate feed. The energy demand rises from $47.96\,\mathrm{kWh/m^3_D}$ for $d_{AEM} = 75\,\mu\mathrm{m}$ to $55.24\,\mathrm{kWh/m^3_D}$ for $d_{AEM} = 130\,\mu\mathrm{m}$. This means that $13\,\%$ of electrical energy can be saved by using thinner membranes. Because the effect of increased water transport on outlet concentrations was low in comparison, thinner AEMs with $d_{AEM} = 75\,\mu\mathrm{m}$ were used in the following experiments described in this chapter.

4.3.3 Diluate and Concentrate Flow Rates

In continuous single-pass experiments, outlet concentrations are influenced by diluate and concentrate feed flow rates ($\dot{V}_{F,D}$ and $\dot{V}_{F,C}$). Lower flow rates lead to longer residence times of the fluids in the electric field, where ion transport occurs. This leads to higher concentration differences

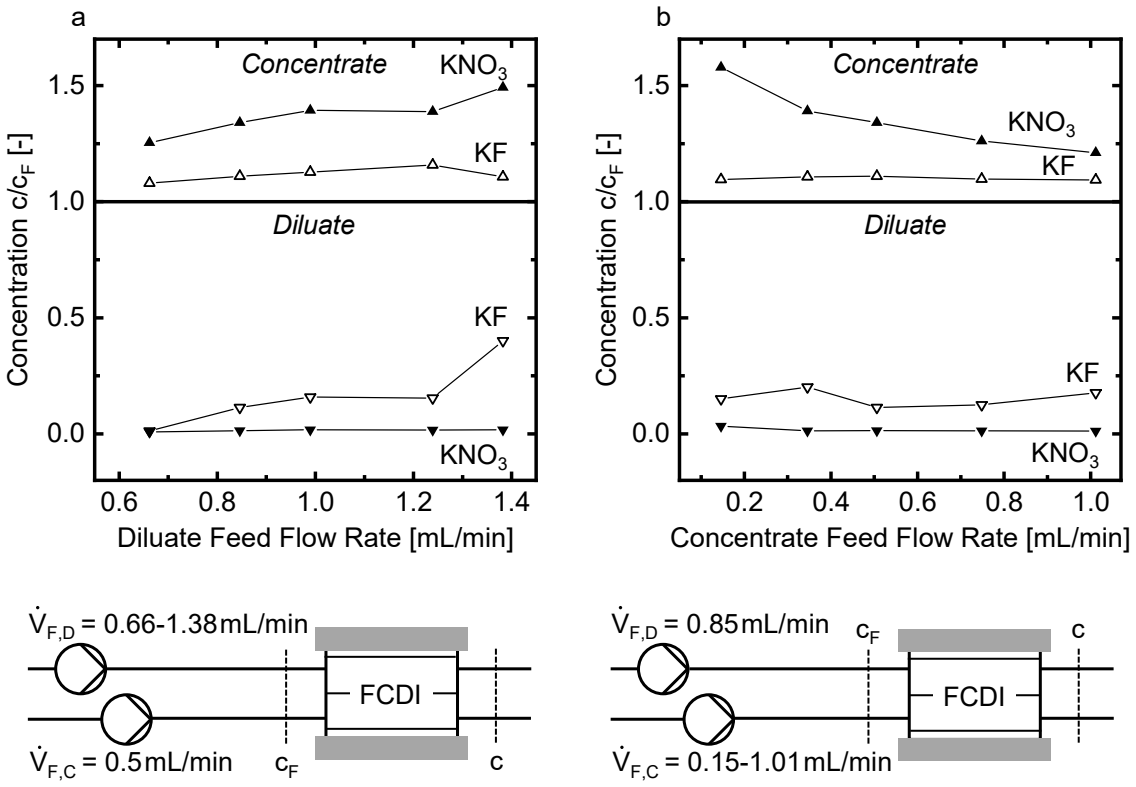

Figure 4.5: (a): Effect of the variation of the diluate feed flow rate on the outlet concentrations. (b): Effect of the variation of the concentrate feed flow rate on the outlet concentrations. Data points are connected by lines to guide the reader's eye.

between the inlet and outlet. Tailoring the flow rates allows to reach different outlet concentrations. The goal is to find the highest possible flow rates with which the required concentrations for diluate and concentrate can be reached. The diluate and concentrate channels influence each other because of the transfer of ions and water. First, $\dot{V}_{F,D}$ was varied, while $\dot{V}_{F,C}$ was kept constant. The effects of this variation on the diluate and concentrate outlet concentrations were investigated. In a second step, $\dot{V}_{F,C}$ was varied while $\dot{V}_{F,D}$ was kept constant.

The lower section of the diagram in Fig. 4.5 (a) shows the outlet concentrations c_{D,KNO_3} and $c_{D,KF}$ normalized by their feed concentrations c_{F,KNO_3} and $c_{F,KF}$. $\dot{V}_{F,D}$ is varied between 0.66–1.38 $\mathrm{mL\,min^{-1}}$. $\dot{V}_{F,C} = 0.5\,\mathrm{mL\,min^{-1}}$ is kept constant.
At the lowest feed flow rate ($\dot{V}_{F,D} = 0.66\,\mathrm{mL\,min^{-1}}$), KF is almost completely removed ($c_{D,KF}/c_{F,KF} = 0.01$). With higher feed flow rates, the concentration

increases and reaches $c_{D,KF} = 0.4 \cdot c_{F,KF}$ for $\dot{V}_{F,D} = 1.38\,\mathrm{mL\,min^{-1}}$. The KNO_3 concentration remains low with a maximum of $c_{D,KNO_3} = 0.02 \cdot c_{F,KNO_3}$. The influence of $\dot{V}_{F,D}$ on concentrate concentrations c_{C,KNO_3} and $c_{C,KF}$ is shown in the upper section of Fig. 4.5 (a). In general, the concentrations increase with increasing diluate feed flow rate. An exception is the lower concentration of KF at $\dot{V}_{F,D} = 1.38\,\mathrm{mL\,min^{-1}}$. This is most likely an outlier. The trend can be explained as follows: a higher diluate flow rate results in a higher amount of ions entering the module, which can be transferred to the concentrate. The ASTR for KNO_3 is high enough that even at high diluate flow rates almost the entire amount of KNO_3 can be transferred. As mentioned above, the transport of KF is inferior and, at high $\dot{V}_{F,D}$, a lower fraction of the KF entering the module can be transported. In summary, the degree of desalination of KNO_3 remains constant throughout the investigated range of $\dot{V}_{F,D}$. The degree of desalination of KF decreases with an increase in the diluate flow rate, while the concentration degree of KNO_3 and KF increases. Thus, the optimal diluate feed flow rate is as high as possible but low enough to achieve the desired outlet concentrations. The required outlet concentration is $0.1 \cdot c_F$. This means that a viable diluate feed flow rate can be found around $\dot{V}_{F,D} = 0.85\,\mathrm{mL\,min^{-1}}$ with outlet concentrations of $c_{D,KNO_3} = 0.01 \cdot c_{F,KNO_3}$ and $c_{D,KF} = 0.11 \cdot c_{F,KF}$.

In the second step, $\dot{V}_{F,D} = 0.85\,\mathrm{mL\,min^{-1}}$ was kept constant and $\dot{V}_{F,C}$ was optimized with the goal to reach outlet concentrations of at least $1.3 \cdot c_F$. The lower section of Fig. 4.5 (b) shows the influence of the concentrate feed flow rate on the concentrations in the diluate. The investigated concentrate feed flow rates range from $\dot{V}_{F,C} = 0.15\,\mathrm{mL\,min^{-1}}$ to $\dot{V}_{F,C} = 1.01\,\mathrm{mL\,min^{-1}}$.
The KNO_3 concentration of the diluate c_{D,KNO_3} remains almost constant. It varies between $0.01 \cdot c_{F,KNO_3}$ and $0.03 \cdot c_{F,KNO_3}$. The KF concentration $c_{D,KF}$ ranges from $0.11 \cdot c_{F,KNO_3}$ to $0.20 \cdot c_{F,KNO_3}$. It has to be noted that a precise setting of $\dot{V}_{F,D}$ was not always achieved due to deficient precision of the peristaltic pump. This caused the variation in $c_{D,KF}$. Overall, the influence of $\dot{V}_{F,C}$ on the concentrations in the diluate can be considered low.
The influence of $\dot{V}_{F,C}$ on the concentrate side is shown in the upper section of Fig. 4.5 (b). At $\dot{V}_{F,C} = 0.15\,\mathrm{mL\,min^{-1}}$ the concentration degree of KNO_3

is highest at $c_{C,KNO_3} = 1.58 \cdot c_{F,KNO_3}$. An increase in $\dot{V}_{F,C}$ leads to a decrease in concentration. The lowest concentration is $c_{C,KNO_3} = 1.21 \cdot c_{F,KNO_3}$ at $\dot{V}_{F,C} = 1.01\,\mathrm{mL\,min^{-1}}$. The concentration of KF is not influenced by $\dot{V}_{F,C}$ as much, since it only varies between $1.09 \cdot c_{F,KF}$ and $1.11 \cdot c_{F,KF}$. Overall, $\dot{V}_{F,C}$ mainly influences the concentration degree of KNO_3 while the concentration degree of KF remains almost constant.

Summarizing the results of the experiments, the target concentration of $0.1 \cdot c_F$ on the diluate side can be reached for both salts. On the concentrate side, the target concentration of $1.3 \cdot c_F$ can only be reached for KNO_3. At $\dot{V}_{F,C} = 0.5\,\mathrm{mL\,min^{-1}}$ the outlet concentration is $c_{C,KNO_3} = 1.34 \cdot c_{F,KNO_3}$. As $c_{C,KF}$ remains constant throughout the range of $\dot{V}_{F,C}$, the choice of a lower $\dot{V}_{F,C}$ does not improve the KF concentration. However, there are other adjustments to the FCDI process that may be used to yield higher KF concentrations. One possibility is operation at higher voltages, described in the next section. The results of the experiments show that concentrate feed flow rates have a low influence on diluate concentrations. Vice versa, the diluate feed flow rates do influence the concentrate concentrations. Therefore, the diluate feed flow rates should always be adjusted before the concentrate feed flow rates.

4.3.4 Operating Voltage

The next step was to investigate the operating voltage. Typically, FCDI processes are operated with a potential difference of $1.2\,\mathrm{V}$ between the two current collectors. This ensures that no electrochemical reactions can occur, because the standard potential difference for water electrolysis is $1.23\,\mathrm{V}$. However, there is also literature on FCDI processes at higher voltages [Tang2020]; [Xu2017]. Higher voltages lead to a higher driving force for ion transport. The hypothesis for this investigation is that the concentration differences found in the evaluation of the flow rates can be improved with higher voltages. Here, voltages up to $2.0\,\mathrm{V}$ are investigated. Since almost all KNO_3 is already transported from the diluate when operating with $1.2\,\mathrm{V}$, the expectation is that there will be no increase in KNO_3 transport. The goal of

the experiments is to increase the transport of KF to reach lower concentrations in the diluate and higher concentrations in the concentrate. The feed flow rates are fixed at $\dot{V}_{F,D} = 1.35\,\mathrm{mL\,min^{-1}}$ and $\dot{V}_{F,C} = 0.53\,\mathrm{mL\,min^{-1}}$. The current efficiencies in all experiments are above 90 %, indicating that the extent of water splitting at the electrodes is low.

Fig. 4.6 (a) shows the ASTRs for KF and KNO_3 and the total ASTR for increased voltages. The ASTR for KNO_3 remains constant, since even at 1.2 V almost all KNO_3 is transported from the diluate. The ASTR for KF increases from $3.34\,\mu\mathrm{mol\,min^{-1}\,cm^{-2}}$ at 1.2 V to $4.92\,\mu\mathrm{mol\,min^{-1}\,cm^{-2}}$ at 2.0 V. The increased ion transport at elevated voltages also causes changes to the water transport between diluate and concentrate. Fig. 4.6 (b) shows the total ion transport divided by the total water transport ($\frac{\Delta m_{KF}+\Delta m_{KNO_3}}{\Delta m_{H_2O}}$). Although total ion transport increases, the increase in water transfer is stronger, leading to a falling trend. When dividing the individual salts by the total water transport ($\frac{\Delta m_{KF}}{\Delta m_{H_2O}}$ and $\frac{\Delta m_{KNO_3}}{\Delta m_{H_2O}}$) the curve for KNO_3 is falling, since the amount of KNO_3 remains constant. The curve for KF rises and flattens out at 2.0 V. The increased water transport is caused by the water in the hydration shells of the additional potassium and fluoride ions that are transported at higher voltages.

Water transport also has an impact on the outlet concentrations c_D and c_C of both salts. Fig. 4.6 (c) shows that the diluate concentration of KNO_3 remains constant at very low values (between 4 % and 1 % of the feed concentration). The KF concentration decreases from $0.48 \cdot c_{F,KF}$ at 1.2 V to $0.09 \cdot c_{F,KF}$ at 2.0 V. Thus, lower KF outlet concentrations can be reached with elevated voltages. But the concentrate side also needs to be taken into account. Here, the KF concentration increases from $1.07 \cdot c_{F,KF}$ to $1.17 \cdot c_{F,KF}$. However, as already shown in Fig. 4.6 (b), the increased KF transport also causes increased water transport from the diluate into the concentrate. There is no more KNO_3 that could be transported to balance the increased water transport and the outlet concentration c_{C,KNO_3} decreases at higher voltages. At 1.2 V the outlet concentration is $c_{C,KNO_3} = 1.51 \cdot c_{F,KNO_3}$; at 2.0 V it is only $c_{C,KNO_3} = 1.39 \cdot c_{F,KNO_3}$. Therefore, there is a trade-off between a higher con-

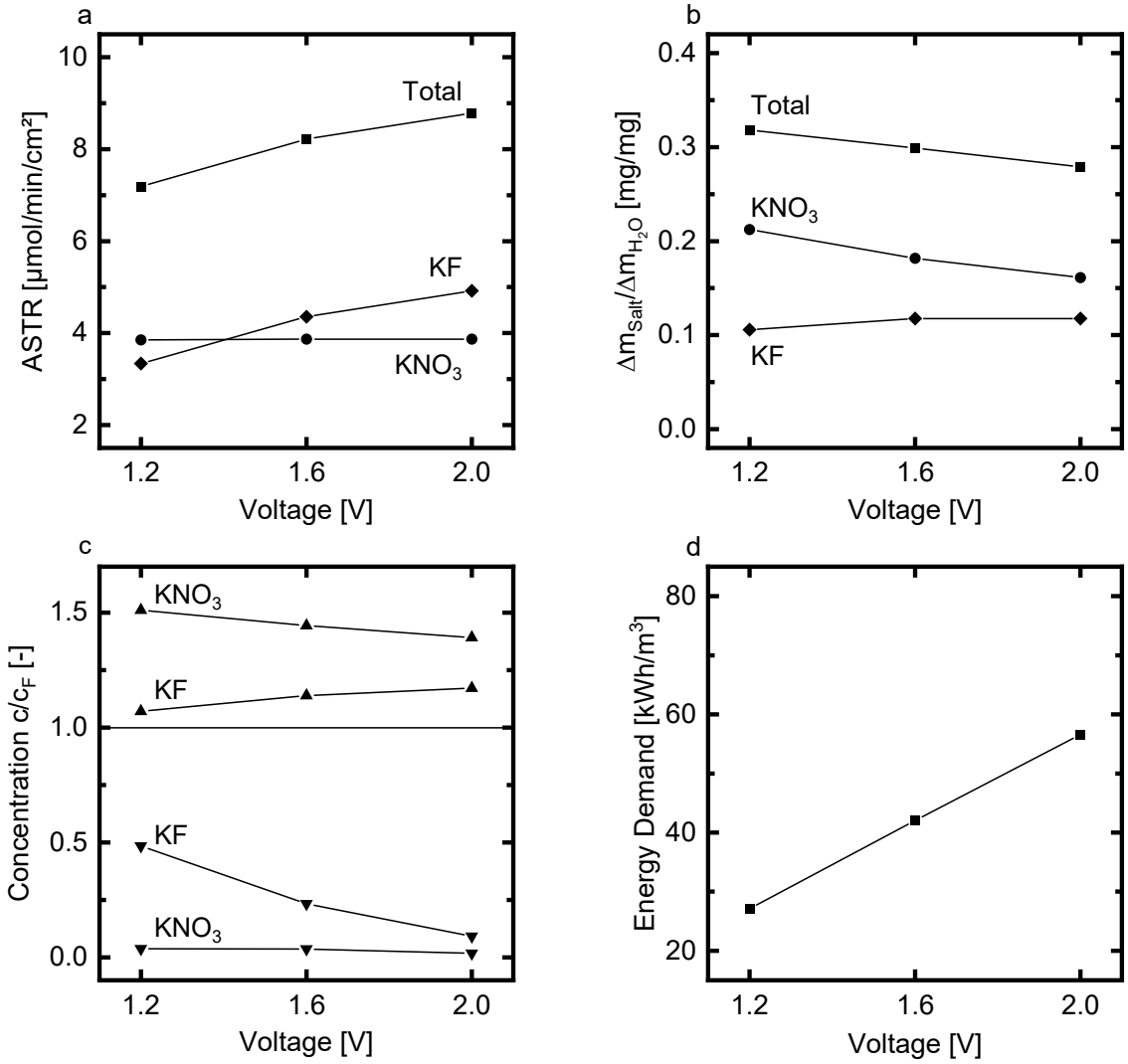

Figure 4.6: Effect of operating voltage on (a) ASTR, (b) water transport, (c) outlet concentrations, and (d) energy demand. Data points are connected by lines to guide the reader's eye.

centration of KF at high voltages and a high concentration of KNO_3 at low voltages. The target concentration in the diluate of $c_{D,KNO_3} \leq 0.1 \cdot c_{F,KNO_3}$ can be reached with lower voltages as well as elevated voltages. More experiments (at pilot scale) will be necessary to investigate the effect of elevated voltage on real wastewater.

Elevated voltages V also cause an increase in electrical energy demand, as shown in Eq. 4.1. The energy demand is shown in Fig. 4.6 (d). It increases from $27.11\,\mathrm{kWh/m^3_D}$ at $1.2\,\mathrm{V}$ to $56.54\,\mathrm{kWh/m^3_D}$ at $2.0\,\mathrm{V}$.

For the long-term operation of the FCDI process on the lab scale (see next

Section) it was decided to keep the voltage at 1.2 V. This avoids the risk of water electrolysis and hydrogen production. For the goals of the project on the concentrate side, operation at higher voltages remains an interesting option since the price of the educt hydrofluoric acid (HF) is higher than that of nitric acid, and the economics of the process could be improved with a higher recycling rate of fluoride. The trade-off between the energy demand for the FCDI step and higher fluoride recycling rate would need to be investigated on a larger scale. On the diluate side, the outlet concentrations of KF even at elevated voltages exceed regulatory limits. Therefore, a post-treatment step of the diluate (e.g., precipitation of fluoride) will always be necessary.

4.3.5 Long-term Experiments

Long-term experiments were used to evaluate the behavior of the FCDI process over several days. The experiments were also used to produce 2 L samples of concentrate to run the concentrate loop in the NITREB process together with the project partner testing Electrodialysis with Bipolar Membranes (EDBM). Since the preceding steps of wastewater treatment at the stainless steel plant were already in place, it was now possible to use the real wastewater as feed for the diluate side of FCDI. The concentrations of the wastewater were $c_{F,KNO_3} = 48\,\mathrm{g\,L^{-1}}$ and $c_{F,KF} = 38\,\mathrm{g\,L^{-1}}$. These concentrations are higher than the model feed solution with $c_{F,KNO_3} = 38\,\mathrm{g\,L^{-1}}$ and $c_{F,KF} = 33\,\mathrm{g\,L^{-1}}$ used before. Since the loop between FCDI and EDBM was not yet established, the same concentrate feed as before with $c_{F,KNO_3} = 83.67\,\mathrm{g\,L^{-1}}$ and $c_{F,KF} = 73.44\,\mathrm{g\,L^{-1}}$ was used.

In the following, a long-term experiment with a total duration of 300 h is described. The voltage was 1.2 V. During the experiment, the outlet concentrations of diluate and concentrate were tracked by measuring the conductivity at the outlets. However, this only gives an impression of the overall salt content and not the individual concentrations of KF and KNO_3. Thus, samples were taken to measure the salt concentrations. During the experiment, the flow electrode was changed twice. The flow electrode initially used had

a volume of 200 mL and was changed after about 90 h. The flow electrodes used subsequently had a volume of 400 mL. After a total experiment time of 250 h the second flow electrode was exchanged for the third. All flow electrodes had an initial concentration of $c_{FE,KNO_3} = 150\,\mathrm{g\,L^{-1}}$. The feed flow rates were determined at the end of the experiment ($\dot{V}_{F,D} = 1.07\,\mathrm{mL\,min^{-1}}$ and $\dot{V}_{F,C} = 0.10\,\mathrm{mL\,min^{-1}}$). Furthermore, stable outlet flow rates during sampling suggest that the feed flow rates are also stable during the experiment. A maximum deviation of 10 % is assumed. In conclusion, the concentrate flow rate is lower than the lowest concentrate flow rate studied in the various experiments described above. The diluate feed flow rate is closest to the flow rate $\dot{V}_{F,D} = 0.99\,\mathrm{mL\,min^{-1}}$ used in the experiments described in Section 4.3.3. There, outlet concentrations of $c_{D,KNO_3} = 0.02 \cdot c_{F,KNO_3}$ and $c_{D,KF} = 0.16 \cdot c_{F,KF}$ were found.

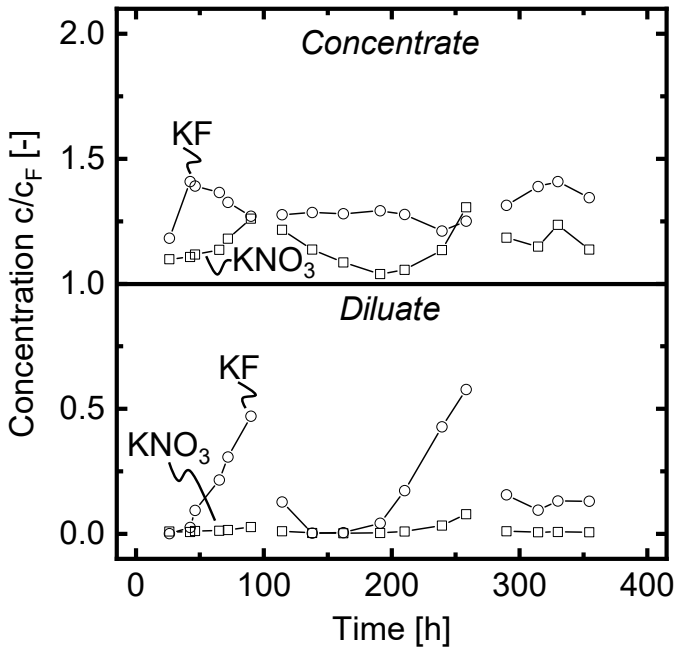

Figure 4.7: Trajectories of the concentrations during a 350 h long-term experiment. Data points are connected by lines to guide the reader's eye. At the breaks in the line the experiment was stopped and the flow electrode was changed.

Fig. 4.7 shows the trajectories of the outlet concentrations of KNO_3 and KF over time. The values are connected by lines to guide the reader's eye. The connecting lines are broken where the flow electrode was exchanged. The first sample was taken 26 h after the start of the experiment. Diluate concen-

trations are low ($c_{D,KNO_3} = 0.01 \cdot c_{F,KNO_3}$ and $c_{D,KF} < 0.01 \cdot c_{F,KF}$). This is lower than could have been expected from the previous experiments. On the concentrate side $c_{C,KNO_3} = 1.10 \cdot c_{F,KNO_3}$ and $c_{C,KF} = 1.18 \cdot c_{F,KF}$ are reached. Soon after, $c_{C,KF}$ starts to rise to a value of $c_{C,KF} = 1.41 \cdot c_{F,KF}$. This is an unexpectedly high concentration degree for KF. However, over the course of the next 50 h the desalination degree of KF decreases strongly. After 90 h the diluate outlet concentration is only $c_{D,KF} = 0.47 \cdot c_{F,KF}$. The cause of this trend is unclear, but it also influences the concentrate side of the FCDI process. Since less KF is transported, the outlet concentration $c_{C,KF}$ drops. A lower transport of KF leads to a lower water transport and the concentration c_{C,KNO_3} rises. Since the high concentrations of KF in the diluate outlet are undesired, the experiment is temporarily stopped and the flow electrode is investigated. An analysis of the salt concentration in the flow electrode reveals $c_{FE,KNO_3} = 60\,\mathrm{g\,L^{-1}}$ and $c_{FE,KF} = 52\,\mathrm{g\,L^{-1}}$. This is unexpected, as the flow electrode initially only contained $150\,\mathrm{g\,L^{-1}}$ KNO_3. Notably, the total molar concentration remains almost constant (see Tab. 4.1).
The first possible explanation was a leak in the module, so a leakage test with ultrapure water was conducted. However, no leakage was detected. It is hypothesized that the concentrations in the flow electrode might adjust over time as a result of the irregular transport of anions across the CEMs that separate the flow electrode from the diluate and concentrate channels. In the CEM datasheet, the manufacturer specifies a selectivity for cations of $S > 95\,\%$ for KCl. This means that around 5 % of the charge transport across the CEMs may be due to fluoride and nitrate ions. When calculating the total transport over 90 h, the observed changes in concentration are reasonable. However, these changes do not explain the increase in outlet concentration $c_{D,KF}$.

After the investigation, the experiment was restarted with a new flow electrode and the same diluate and concentrate feeds. Again, an initial concentration of $c_{FE,KNO_3} = 150\,\mathrm{g\,L^{-1}}$ is used. To reduce the effect of fluoride crossover, the volume of the flow electrode is increased from 200 mL to 400 mL. The experiment is restarted at 114 h. Initially, $c_{D,KF}$ remains low and $c_{C,KF}$ is stable at $c_{C,KF} = 1.28 \cdot c_{F,KF}$. The concentration c_{C,KNO_3} falls

	Time used $[h]$	$c_{FE,\,KNO_3}$ $[\frac{mol}{L}]$	$c_{FE,\,KF}$ $[\frac{mol}{L}]$	$\sum c_{FE}$ $[\frac{mol}{L}]$
Start	0	1.48	0	1.48
End 1st FE	90	0.59	0.90	1.49
End 2nd FE	144	0.70	0.83	1.53
End 3rd FE	65	0.91	0.64	1.55

Table 4.1: Time of usage and concentrations of the flow electrodes used in the long-term experiment.

until the trend is reversed after 191 h. $c_{D,KF}$ starts to rise again, reaching $c_{D,KF} = 0.58 \cdot c_{F,KF}$ after 258 h. This time, c_{D,KNO_3} also rises. After a total experiment time of 258 h the experiment is stopped again and restarted with a new flow electrode. With this flow electrode, the experiment is continued until enough concentrate for the EDBM step is generated after 354 h. When adjusting for the pauses in which the flow electrodes were changed, the experiment was run for 300 h. Comparison of the end concentrations of the flow electrodes given in Tab. 4.1 shows that the total concentration of KF and KNO_3 stays almost constant. Nitrate ions are lost from the flow electrode and replaced by fluoride ions. This effect is so small that it was not detected in the previous experiments with durations of only a few hours. However, over the time of the long-term experiment, this small effect leads to significant shifts in concentration. This shows why long-term experiments are important to fully understand the behavior of the FCDI system. In subsequent experiments, a flow electrode with a composition of KNO_3 and KF was used, as already tested in Section 4.3.1. In these experiments, the outlet concentrations were stable over time.

4.3.6 Pilot-scale Tests

The aim of the NITREB research project was to test the FCDI process on pilot scale with real wastewater from the stainless steel treatment plant. After scale-up of the FCDI module was complete (see Chapter 3) and the FCDI pilot plant was built, a trial with a duration of one month was launched.

The results from module scale-up had already shown that the desalination performance from the lab scale could not be transferred to the pilot scale. Therefore, the flow rates in continuous operation would need to be minimal to achieve adequate desalination and concentration. Instead, the operation mode was changed from single-pass continuous operation to batch operation of both diluate and concentrate. The assumption discussed in Chapter 3 was that batch operation could improve the performance of the FCDI process due to better flow conditions in the spacers. It is not possible to directly compare the results from the pilot-scale tests with the tests at the lab scale since too many variables were changed: the module layout of the pilot-scale module is different from lab-scale modules to enable a high membrane area. Additionally, the feed concentrations are different from the lab-scale tests, since the concentrations in the wastewater change with the operating parameters of the pickling line. Therefore, the aim of the results presented in the following is not to establish a comparison between lab scale and pilot scale but to showcase the performance of the FCDI process in a real-world environment.

Fig. 4.8 shows the trajectories of the diluate and concentrate batch tank filling volume and the corresponding conductivities. In total, 14 diluate batches and 75 concentrate batches are shown. Some batches were not completed due to interruptions in plant operation. These interruptions were caused by external factors (e.g., power cuts). At the beginning of a new batch, the volume in the tanks increases rapidly as the new solution is pumped into the tank. Then the volume changes slowly as a result of the water transfer during the experiment (diluate volume decreases, concentrate volume increases). At the end of a batch, the volume sharply decreases to a preset value as the tank is emptied. The tanks are never fully emptied. Correspondingly, the diluate conductivity rises sharply at the beginning of a batch because the new solution is pumped into the tank and passes the conductivity sensor. The starting conductivity of the batch is measured when the new solution has mixed with the remaining diluate in the tank, and the FCDI process is started again. In the concentrate, low conductivities are measured until the solutions have mixed.

The data also show how the target conductivities for diluate and concentrate were changed during the trial. At first, the target conductivity for the diluate was $5\,\mathrm{mS\,cm^{-1}}$. This was never reached, because a minimum tank volume of $9\,\mathrm{L}$ was specified. When the tank volume dropped below $9\,\mathrm{L}$ due to water transport, the batch was automatically stopped and a new batch was started. On May 6$^{\text{th}}$ the target conductivity was changed to $30\,\mathrm{mS\,cm^{-1}}$. Additionally, the tank volume at the beginning of a batch was changed from $21\,\mathrm{L}$ to $29.75\,\mathrm{L}$. With a larger starting volume and a higher target conductivity, batches can be completed. However, this shows that sufficient desalination was not achieved with the FCDI module on pilot scale. On the concentrate side, high concentrations were targeted until May 4$^{\text{th}}$. The same solution was used in multiple batches. The maximum concentrate tank volume of $28\,\mathrm{L}$ ended most batches. On May 4$^{\text{th}}$, the conductivity target was changed to $80\,\mathrm{mS\,cm^{-1}}$. This allowed for the completion of several batches in the next 20 days.

Due to the abundance of data, a shorter period of $42\,\mathrm{h}$ between May 8$^{\text{th}}$ 2023 15:20 and May 10$^{\text{th}}$ 08:30 is examined more closely.

Fig. 4.9 (a) shows the trajectories of batch tank volume and inlet conductivity over time for the diluate. At first, $31\,\mathrm{L}$ with a conductivity of $87.3\,\mathrm{mS\,cm^{-1}}$ were present in the batch tank. The KNO_3 concentration was $28\,\mathrm{g\,L^{-1}}$ and the KF concentration was $42\,\mathrm{g\,L^{-1}}$. The target conductivity was $30\,\mathrm{mS\,cm^{-1}}$. During the $42\,\mathrm{h}$ shown, the target conductivity was not reached; at the end of operation the conductivity in the diluate circuit was $43.7\,\mathrm{mS\,cm^{-1}}$. Analysis of the sample showed a concentration of $0.82\,\mathrm{g\,L^{-1}}$ KNO_3 and $24.23\,\mathrm{g\,L^{-1}}$ KF. While KNO_3 was removed to a high degree, the KF concentration remained high. An increase in KF transport can only be expected once there is no KNO_3 left in the diluate. The volume in the diluate tank decreased to $25.7\,\mathrm{L}$. Fig. 4.9 (b) shows ten concentrate batches. In each batch, the conductivity in the concentrate circuit increased from $68\,\mathrm{mS\,cm^{-1}}$ (feed composition approx. $12\,\mathrm{g\,L^{-1}}$ KNO_3, $32\,\mathrm{g\,L^{-1}}$) to $80\,\mathrm{mS\,cm^{-1}}$. At the end of the last batch, a sample was taken in which concentrations of $13.6\,\mathrm{g\,L^{-1}}$ KNO_3 and $36.8\,\mathrm{g\,L^{-1}}$ KF were measured. This shows that the conductivity change of $12\,\mathrm{mS\,cm^{-1}}$

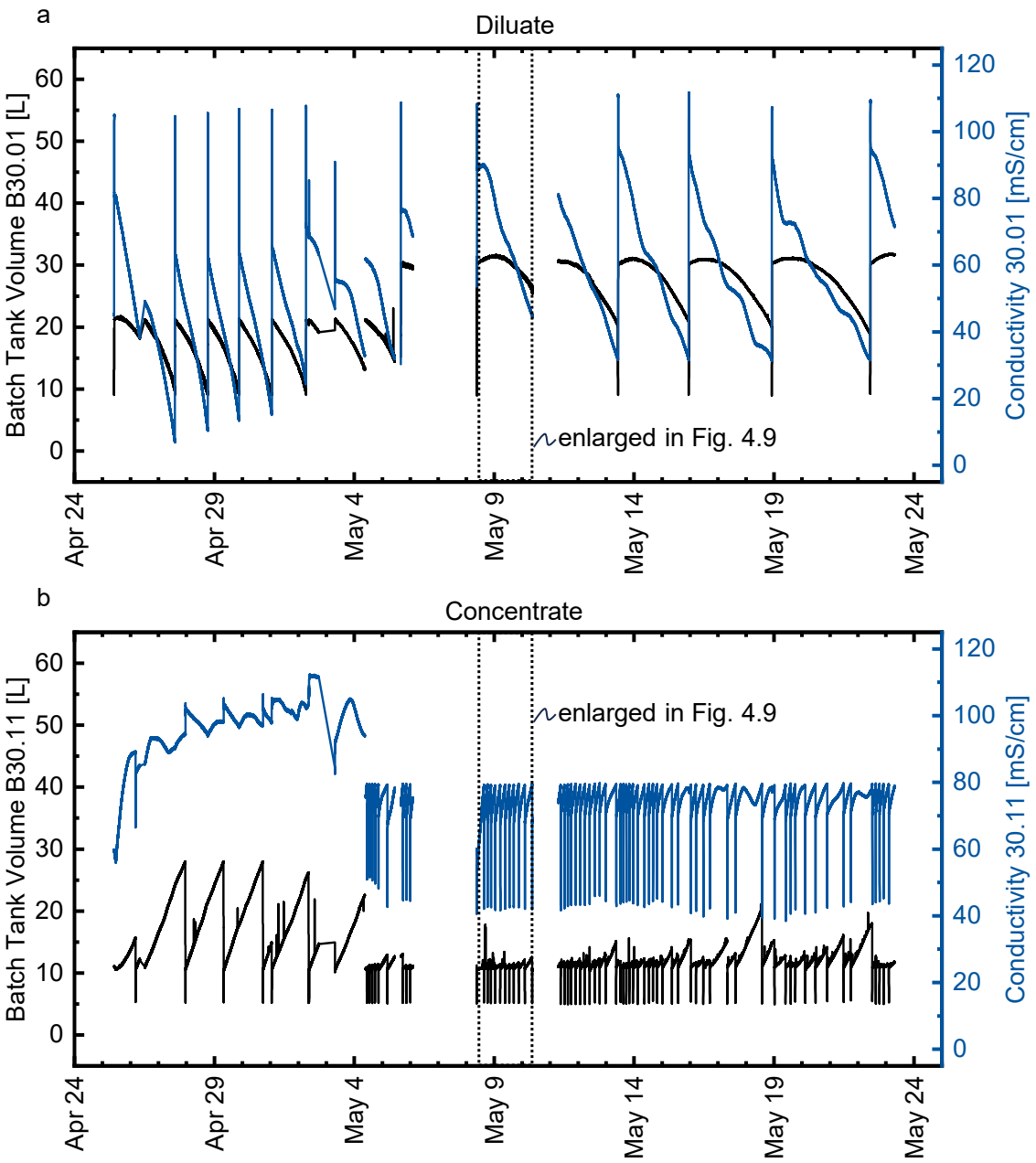

Figure 4.8: (a): Course of diluate batch tank filling volume and diluate inlet conductivity over time. (b): Course of concentrate batch tank filling volume and concentrate inlet conductivity over time. Operational parameters were adjusted as described. Breaks in the data are caused by interruptions in the experiment.

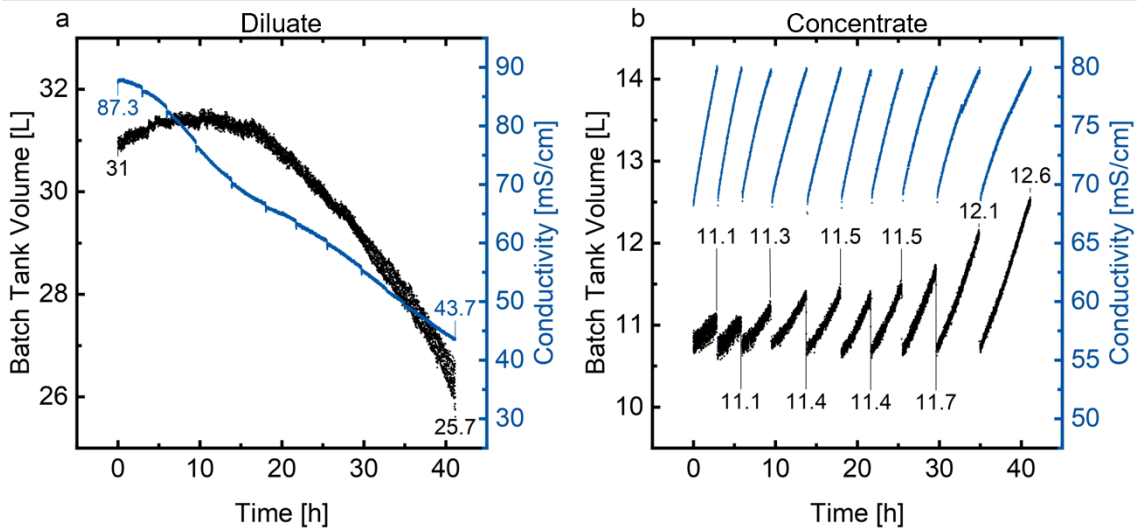

Figure 4.9: Enlarged view of batch tank volume and conductivity over time for a duration of 42 h. (a): Diluate, (b): Concentrate. The number of data points is reduced; scattered data points resulting from measurements during the emptying and refilling of the batch tanks are omitted for better readability.

4

corresponds only to small changes in salt concentration. The concentrations reached with FCDI are too low for effective treatment with EDBM in the next step of the process.

After reaching the target conductivity of the concentrate, the batch tank was automatically emptied to a volume of 5.25 L and then refilled to 10.5 L before the next batch was started. In the diagram, the volumes at the end of each batch are marked. Throughout a batch, the concentrate gains water through osmosis and transport of water in the hydration shells of ions (see Chapter 2.5). The amount of water carried over increases towards the end of the operation. An analysis of the mass balance and the total current in the last batch revealed an unaltered high current efficiency. The water transfer into the concentrate was greater than the water loss from the diluate. This leads to the conclusion that the concentrate gains additional water from the flow electrode.

In summary, the desalination capacity of one FCDI module is too low to process a diluate batch in a reasonable time. High concentrations of KF at the end of a diluate batch cause a high loss of fluoride. On the concentrate side, the KF and KNO_3 concentrations at the end of a batch are too

low to allow the successful operation of the NITREB process. To increase the treatment capacity of the FCDI process, the membrane area must be increased by either using modules with a higher number of repeating units or by connecting several modules in parallel. As discussed in the thought experiment in Chapter 3, ED would likely yield better results than FCDI without increasing the membrane area. For this reason, the FCDI step in the NITREB pilot plant was replaced by ED.

4.4 Conclusion and Outlook

The research project NITREB led to the first demonstration of the FCDI process on pilot scale. The application was the treatment of wastewater from a stainless steel pickling line. On the diluate side, potassium nitrate and potassium fluoride should be removed to at least 90 %, and on the concentrate side the concentrations should be increased to 130 % to allow salt recycling.

Several steps were taken to validate the process on a lab scale prior to the pilot scale trial. This chapter summarizes these steps and aims to provide a guide for the application of FCDI to novel separation tasks. Intensive lab-scale tests are inevitable to judge the applicability of FCDI. These experiments should be conducted with a well-tuned flow electrode (with minimal overall water loss). To enable this, the flow electrode concentration must be set correctly, especially in the case of salt mixtures. It is sensible to start the experiments with a well-tuned flow electrode to avoid high water crossover. However, the following steps might require a readjustment of the flow electrode. In these steps, the flow rates and (if applicable) the voltage of the FCDI process are adjusted. In continuous single-pass experiments, the flow rates of the diluate and concentrate have the greatest influence on the resulting outlet concentrations. The voltage can only be adjusted in cases where electrochemical reactions at the electrode will either not occur or can be tolerated. This might not be the case for all possible FCDI applications. Long-term experiments on lab scale are valuable because

they can reveal small influences that accumulate over time and that are not detected in typical short-term experiments. In the work presented in this chapter, a small crossover of anions across a cation-exchange membrane led to an accumulation of fluoride in the flow electrode.

The flowchart presented in Fig. 4.2 can be used to tailor the FCDI process to other separation tasks in the future. However, caution is necessary when transferring these results to practical application on a pilot scale: in the NITREB project, the results of lab-scale experiments were satisfactory. The desired diluate concentrations were reached. The concentrate side of the process was limited, mainly because of the water transfer from the diluate to the concentrate. However, the deficiencies were more severe on pilot scale. The membrane area of an FCDI module with 20 stacking units was too small to allow adequate flow rates for single-pass operation. Even with batch operation, the salt transport was not sufficient to reach the target concentrations of the diluate or concentrate. In the NITREB pilot application, FCDI was inferior to electrodialysis.

In the future, further scale-up of the FCDI process is needed. This can be achieved by modules with more stacking units or by parallel connection of multiple modules. Alternatively, the membrane cross-section could be enlarged. However, this would necessitate new concepts for flow electrode channels. A larger membrane cross-section would lead to longer channels which would eventually cause high pressure loss and cause clogging of the channels. This could be avoided with a higher number of flow-electrode channels. Alternatively, new module concepts similar to swiss-roll reactors or tubular membrane modules should be investigated. In these types of membrane modules, the membrane area would be increased without stacking, and the disadvantage that is caused by the parallel connection of membranes and flow electrodes would disappear. However, the effect of non-planar electrodes would need to be rigorously tested. Fig. 4.10 shows two possible module designs. The swiss-roll design in Fig. 4.10 (a) uses graphite current collectors and tubular ion-exchange membranes, the tubular module in Fig. 4.10 (b) uses tubular membrane-electrode assemblies

made of ion-exchange membranes and carbon fiber fabric. In both concepts, scale-up could be achieved by increasing the length of the tubes and by connecting multiple elements in parallel to each other.

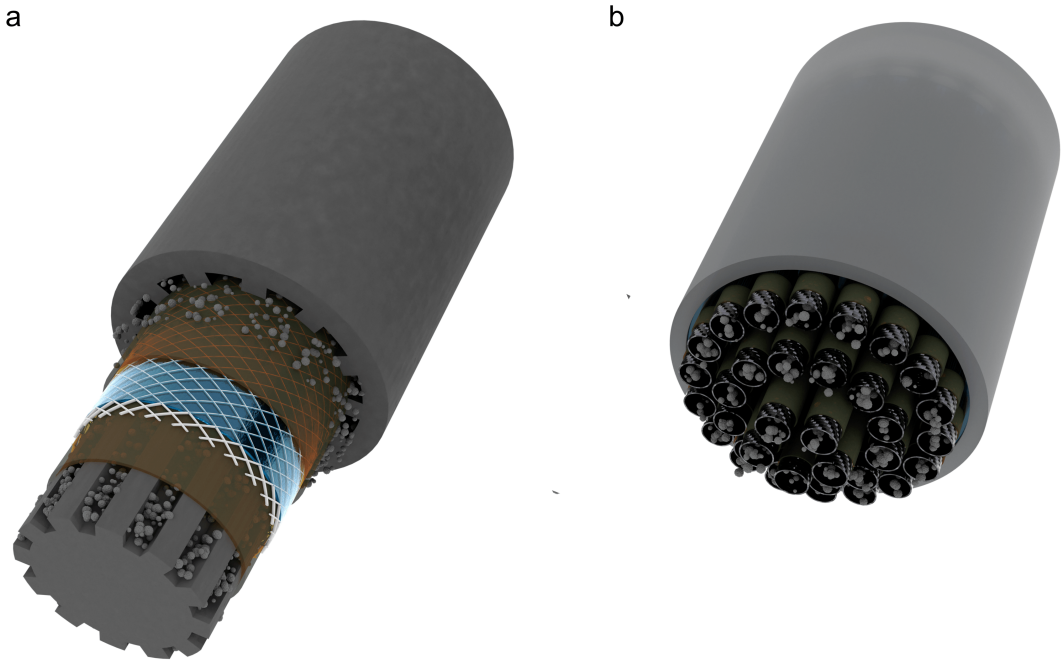

Figure 4.10: Possible alternative module designs. (a): FCDI module similar to a swiss-roll reactor employing tubular ion-exchange membranes and spacers (b): Tubular membrane module for FCDI employing tubular membrane-electrode assemblies made of ion-exchange membranes and carbon fiber fabric.

For future pilot-scale tests, less demanding applications (no salt mixtures, lower concentration differences) should be chosen. The results from the first pilot scale test show that the required membrane area for FCDI is higher than for its main competitor ED. This leads to a higher initial cost for the modules. Thus, the production cost of FCDI modules should be decreased. Chapter 5 details a new current collector architecture that reduces the cost of stacked FCDI modules.

5 Comparison of Current Collector Architectures

Parts of this chapter have been published as:

Niklas Köller, Mila Perrey, Lantz K. Brückner, Philipp Schäfer, Sebastian Werner, Christian J. Linnartz, Matthias Wessling

Comparison of current collector architectures for Flow-electrode Capacitive Deionization, Desalination, 2024

DOI: 10.1016/j.desal.2024.117595

5.1 Introduction

Current collectors are an integral part of Flow-electrode Capacitive Deionization (FCDI) module architectures. Chapter 2.5.2 gives an overview of different current collectors used in the literature. Our research group has previous experience working with graphite plates (GPs) and membrane-electrode assemblies (MEAs). In our research on MEAs, we realized that these current collectors change the concept of charge transport to the particles in the flow electrode. Charge transfer no longer occurs at the three walls of the flow channel, but directly at the membrane. Although this leads to a significantly smaller area where electrons can be exchanged with the flow electrode particles, the salt transport rate remains constant. We hypothesized that this was due to shorter transfer paths from the membrane to the current collector when using MEAs [Linn2020]. However, we were unable to prove this hypothesis. This is the first reason we wanted to continue our work on current collectors. The second reason is the MEA manufacturing process. Although MEAs allow the scale-up of FCDI modules, their production is labor- and time-intensive, as the experience with the modules described in Chapter 3 has shown. The hot-pressing step to laminate the ion-exchange membrane to the carbon fiber fabric is followed by a sealing step with silicone rubber. Since the MEAs themselves do not feature a flow channel for the flow electrode, a second part (usually 3D-printed from a polymeric, non-conductive material) is necessary. The price of these parts amounts to a significant share of the overall price of an FCDI module. Therefore, a novel current collector architecture should reduce the number of parts and manufacturing steps.

Bipolar plate (BP) current collectors from expanded graphite, as used in some fuel cells or redox-flow batteries, offer a viable alternative [Dhak2008]. Expanded graphite plates are available in thicknesses up to 2 mm, and thus thick enough so that a flow channel for a flow electrode can be cut into them. In addition, hot-pressing an IEM directly to the expanded graphite is possible. This facilitates easy production: the only necessary steps are the cutting of the flow channel and the hot-pressing; no further

gaskets or sealing steps are necessary. An overview of the constructive advantages and disadvantages of the different architectures is given in Tab. 5.1. A score ranging from **1** (worst) to **3** (best) is given, and the sum of all scores is used for evaluation. In this comparison, graphite plates and MEAs both achieve a total score of **7**, and BPs achieve a score of **9**. Initial

Architecture	Graphite Plate		MEA		Bipolar Plate	
	Property	Score	Property	Score	Property	Score
Flow channel	Milling	●	3D-printing	●●	Waterjet-cutting	●●●
Membrane	Untreated	●●●	Hot-pressing	●	Hot-pressing	●
Sealing	Gaskets	●●	Silicone	●	Not necessary	●●●
Cost		●		●●●		●●
Evaluation		$\sum ● = 7$		$\sum ● = 7$		$\sum ● = 9$

Table 5.1: Advantages and Disadvantages of the FCDI current collector architectures in this chapter. For each property a score ranging from ● to ●●● is given.

tests showed that composite BPs with polymeric binder (around $10\ wt\%$) are more durable than BPs made from pure expanded graphite. Cutting of the flow channel can be done with a waterjet cutter. This generates a flow channel in which the two walls provide the surface area for charge transport, as shown in Fig. 5.1. With graphite plates, MEAs, and BPs, there are three different current collector architectures that utilize different materials and have different surface areas for charge transport to the flow-electrode particles. This work aims to compare these current collector architectures in FCDI experiments. In the second step, the interfacial area between the current collector and the flow electrode (electron transfer area, ETA) is varied by altering the flow channel geometry of the BP architecture. Additionally, the influence of surface roughness is investigated.

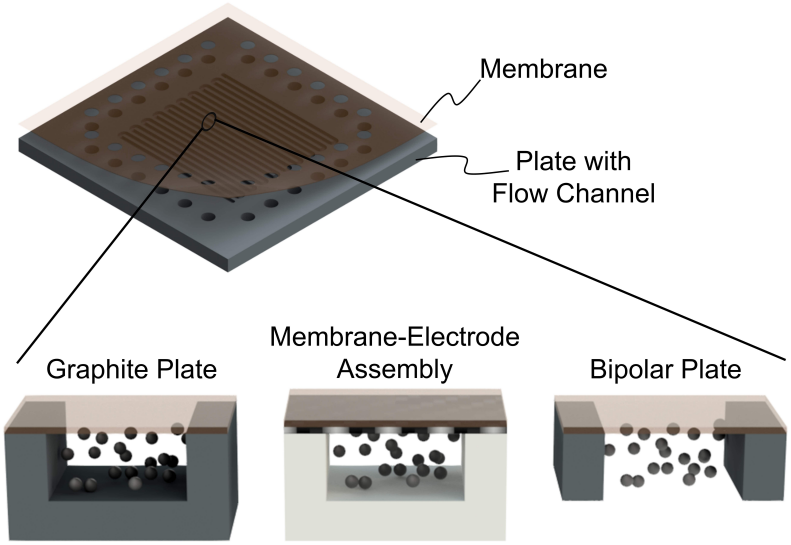

Figure 5.1: Difference in the investigated FCDI architectures. When using a graphite plate, the flow electrode has three side walls at which it can gain charge from the current collector, shown in grey. For the MEA this reduces to the surface area of the carbon fiber fabric beneath the membrane and for the bipolar plate to the two side walls.

5.2 Experimental

5.2.1 Characterization of Current Collector Materials

In this chapter, three different current collector architectures are compared. The first step was to characterize the different materials in electrical resistance measurements. Samples of each material ($50\,\mathrm{mm} \times 50\,\mathrm{mm}$) were clamped between copper plates in a press with a force of $97\,\mathrm{kN}$ at a temperature of $25\,°\mathrm{C}$. Chronoamperometric measurements with a voltage of $1\,\mathrm{mV}$ were used to determine ohmic resistances, and the resistances of the copper plates were deducted. Average resistances from three experiments were used for comparison. From these results, resistivities were calculated according to Eq. 2.8.

Graphite plates are commonly used in FCDI research, and MEAs were investigated in a previous study [Linn2020]. The bipolar plates presented here are a new approach in FCDI; therefore, the contact between the membrane and the bipolar plate was further investigated by swelling tests and field emission scanning electron microscopy (FE-SEM, Hitachi SU5000).

The surface roughnesses of the current collectors were investigated with FE-SEM and optical profilometry (NT2000, Wyko Corporation).

5.2.2 Manufacturing of Current Collectors for FCDI Experiments

For all experiments in this chapter, an FCDI single module design is used [Romm2015]. The module size was chosen to fit ED-100 membranes (active membrane area $100\,\mathrm{cm}^2$, $A_{mem,tot} = 300\,\mathrm{cm}^2$) from Fumatech BWT GmbH. Two current collectors (one positively and one negatively contacted) are required for an FCDI module.
First, graphite plate (GP) current collectors and MEAs are compared with the new bipolar plates (BPs) with fixed geometry. Then, the geometry of the bipolar plates is varied. The epoxy-impregnated GPs ($180 \times 180 \times 10\,\mathrm{mm}$, MR40, Müller & Rössner GmbH & Co. KG) have meandering flow channels with 14 turns milled into one side for the flow electrodes ($3\,\mathrm{mm} \times 1.45\,\mathrm{mm}$ and $1556\,\mathrm{mm}$ total length). The same flow channel layout is also used in the MEA and BP modules, as shown in Fig. 5.2 (a). In the flow channel cross-sections, the conductive material is shown in grey and the non-conductive material in white. The resulting electron transfer area (ETA) for each architecture is given.
In the next step, the channel length of the BP current collectors was varied by reducing the number of turns of the meandering channel from 14 to 10 and to 6, as shown in Fig. 5.2 (b). Additionally, a BP current collector with 14 round turns was investigated. Another set of experiments investigated the influence of the channel side walls and the bottom wall. The BP geometry with 14 turns was used. The side walls were replaced by non-conductive polymeric material and a second BP without flow channel geometry was added as bottom wall, as shown in Fig. 5.2 (c).

MEAs were manufactured according to the process described by Linnartz et al. [Linn2020]. A $30\,\mu\mathrm{m}$ thick FKS-30 membrane (Fumatech BWT GmbH) was used. Furthermore, a $10\,\mathrm{mm}$ rim at the edges of the MEAs was fitted

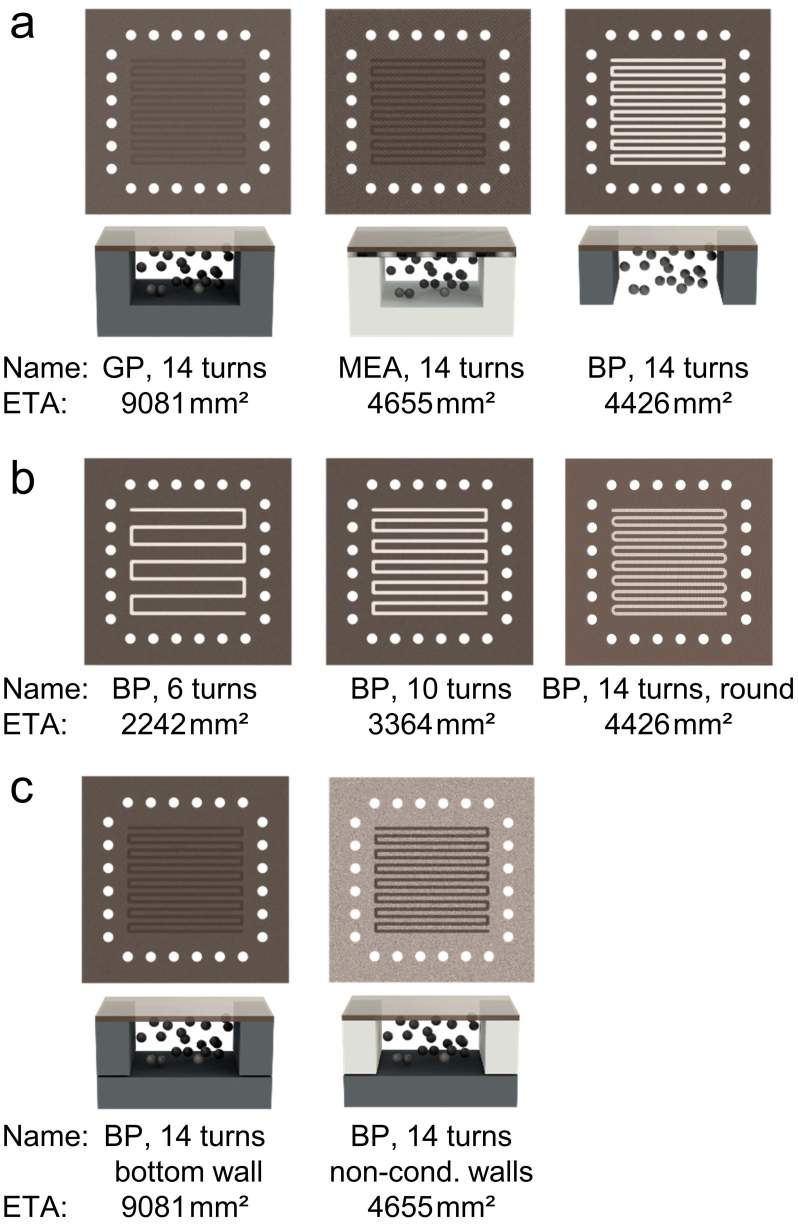

Figure 5.2: Different FCDI current collectors investigated in this chapter. (a): Comparison of different architectures. The GP and the MEA architecture consist of two separate parts, in the BP architecture the membrane and current collector form an assembly. The flow channel geometry is the same in all three architectures. (b): Variation of the flow channel in the BP architecture. (c): BP architectures with the addition of a conductive bottom wall. The BP with a conductive bottom wall has the same ETA as the GP architecture. The conductive bottom wall with non-conductive side walls has the same ETA as the MEA architecture.

with copper tape with a conductive adhesive (ET1181, 3M Corporation) to enable good electrical contact. The flow fields for the MEA modules were 3D-printed with VeroClear material (printer: Objet Eden260, material: VeroClear, Stratasys Ltd.). For the BP modules, expanded graphite plates (Sigracell FR10, SGL Carbon SE) with a thickness of $1.6\,\mathrm{mm}$ were used. The flow channel was cut into the plates by waterjet cutting. Afterwards, CEMs (FKS-130, Fumatech BWT GmbH) were pressed onto the plate at $120\,°\mathrm{C}$ and $570\,\mathrm{N\,cm^{-2}}$ for $7\,\mathrm{min}$. During pressing, the BP and the CEM were sandwiched between aluminum plates (to achieve a good alignment of the CEM and BP) and $250\,\mu\mathrm{m}$ thick sheets of PTFE (to avoid sticking of the CEM to the aluminum plate). The edges of the BP current collectors were fitted with the same copper tape used for the MEAs. The pressing procedure causes the thickness of the expanded graphite plate to reduce to $1.45\,\mathrm{mm}$. Thus, the same channel depth was used for the manufacturing of the flow fields for MEAs and graphite plates.

Anion exchange membranes (FAS-130, Fumatech BWT GmbH) and two $0.5\,\mathrm{mm}$ thick mesh spacers (ED-100 Spacer, Deukum GmbH) were used to complete the modules. Polyoxymethylene end plates were used to clamp the modules and provide connections for the flow-electrode channels and the feed spacers.

5.2.3 FCDI Experiments

The FCDI experiments were carried out in continuous single-pass operation. Feed solutions were prepared by dissolving $60\,\mathrm{g\,L^{-1}}$ sodium chloride (VWR International GmbH) in ultrapure water. The flow electrode was prepared by suspending $15\,wt\%$ activated carbon powder (Carbopal SC11PG, Donau Carbon GmbH) in the same solution. The flow electrode was stirred for at least $12\,\mathrm{h}$ prior to use. The water feed flows were conveyed by peristaltic pumps (REGLO ICC Digital Peristaltic Pump 2-Channel, Cole-Parmer Instrument Company LLC.) from a feed vessel through the module to a product vessel. The flow electrode was conveyed with a peristaltic pump (Masterflex Easyload II, Cole-Parmer Instrument Company LLC.), the

flow rate was set to $200\,\mathrm{mL\,min^{-1}}$ for all experiments. The electric potential was provided to the module by a power supply, which also measured the current (HM8143, Rohde & Schwarz GmbH & Co. KG). The conductivities of diluate and concentrate at the module outlet were measured with conductivity sensors (SE615-MS, Knick Elektronische Messgeräte GmbH & Co. KG and LTC0.35/23, Xylem Analytics Germany Sales GmbH & Co. KG). The pressure drop of the flow electrode channels was measured with pressure sensors (A-10, WIKA AG). The sensors were mounted at the inlet of the first flow electrode channel and at the outlet of the second channel. Thus, both flow electrode channels in the module were measured, including the tubing that connected them. The length of this tubing was constant. At the module inlet, the pressure oscillates due to the peristaltic pump. The average pressures were used to calculate the pressure drop. Data from all sensors and the power supply were acquired and logged with a setup supplied by ZUMOLab GmbH.

Due to the single-pass experiment mode, the outlet conductivities develop towards a steady state. This steady state is used to compare the experiments with each other. The inlet and outlet mass flows are measured by taking samples for a fixed time and weighing them. The density of the samples is measured (Densito 30PX, Mettler-Toledo International Inc.), allowing the calculation of exact volumetric flow rates. A correlation between density and sodium chloride (NaCl) concentration (see Appendix) is used to calculate concentrations from the measured density. To verify the validity of this correlation, some samples were also investigated by ion chromatography (930 Compact IC Flex, Deutsche METROHM GmbH & Co. KG. Anion column: Metrosep A Supp 7 - 250/4.0. Cation column: Metrosep C 6 - 250/4.0). The deviation between the ion chromatography results and the correlation results was in the range of $\pm 5\,\%$. For each different FCDI module, at least three experiments were performed and included in the evaluation. The metrics used for the comparison of the FCDI experiments are given in Eq. 2.5 and Eq. 2.6. The number of cell pairs and stacking units in all experiments is $n_{su} = 1$ and $n_{cp} = 1$. The total membrane area is $A_{mem,tot} = 300\,\mathrm{cm^2}$ (from two $100\,\mathrm{cm^2}$ CEMs and one $100\,\mathrm{cm^2}$ AEM) which is

constant in all experiments.

5.3 Results and Discussion

5.3.1 Material Characterization

While different current collector designs for FCDI are known in the literature, there are no studies in which bipolar plates (BPs) made of expanded graphite are used. Thus, initial tests were necessary to evaluate the material and compare it to the reference materials (here: graphite plate and membrane-electrode assembly).

First, the electrical resistances of the material samples were measured. Low resistances are an important prerequisite for the use of materials as current collectors. Graphite is an anisotropic material with a difference between in-plane and through-plane resistances. BPs made from expanded graphite, also show this anisotropy at the macroscopic level, caused by expanded graphite flakes [Celz2000]. According to the manufacturer's data sheet, the through-plane resistivity of the bipolar plates is higher (in-plane: $7 \times 10^{-7}\,\Omega\,\mathrm{m}$, through-plane: $1 \times 10^{-3}\,\Omega\,\mathrm{m}$). Thus, through-plane resistivities were used to compare the materials and give a first impression of their suitability as current collectors. All materials were tested in the thicknesses that were used to manufacture current collectors for FCDI experiments (graphite plate $10\,\mathrm{mm}$, BP $1.6\,\mathrm{mm}$, carbon fiber fabric $0.1\,\mathrm{mm}$).

First, the electrical resistances of the material samples were measured, then resistivities were calculated according to Eq. 2.8. The BPs used in this study contain a polymeric binder. To investigate the influence of the binder material on the conductivity, a sample of pure expanded graphite was measured as comparison. The resistances are given in Fig. 5.3. The values range from $0.36\,\mathrm{m}\Omega$ for the carbon fiber fabric to $0.52\,\mathrm{m}\Omega$ for the BP. Notably, the resistance of the pure expanded graphite is higher than that of the BP. However, the differences between the materials are negligible in comparison to the typical ohmic resistances of an FCDI cell ($800\,\mathrm{m}\Omega$). Thus,

BPs made from expanded graphite with binder are electrically well-suited as current collectors for FCDI. Furthermore, the resistivities are also shown in Fig. 5.3. The resistivity of the bipolar plate is with $8 \times 10^{-4}\,\Omega\,\mathrm{m}$ close to the manufacturer's value.

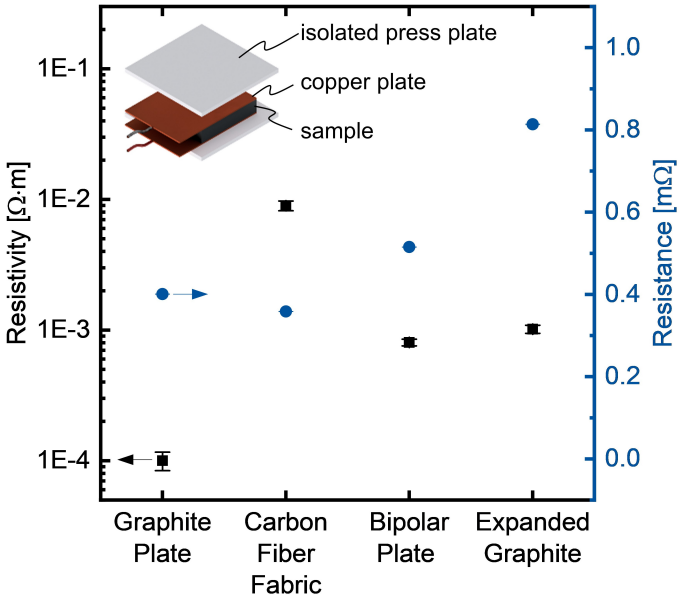

Figure 5.3: Resistivities and resistances of different materials studied as FCDI current collectors. The resistance of the bipolar plate is compared to graphite, carbon fiber fabric used for MEAs and a plate of pure expanded graphite.

The current collectors are formed by hot-pressing ion-exchange membranes to the BPs. The results of the hot-pressing procedure are investigated by FE-SEM. The images in Fig. 5.4 (a) and (b) show that the ion exchange membrane only adheres to the top layer of the BP and does not penetrate the material. At the edges, the membrane detaches slightly from the BP. However, the connection of the two materials is stable enough to withstand handling without any issues. Swelling of the membrane in water also does not cause delamination, as shown in the photographs in Fig. 5.4 (c) and (d). A sample cut out of a current collector was photographed first in dry state (c) and then again after being submerged in ultrapure water for seven days (d). Although the local detachment of the membrane and the BP is visible as light spots, the membrane stays firmly attached to the BP. In the FCDI experiments, the current collectors are additionally clamped in the FCDI modules. When the modules were taken apart after the experiments,

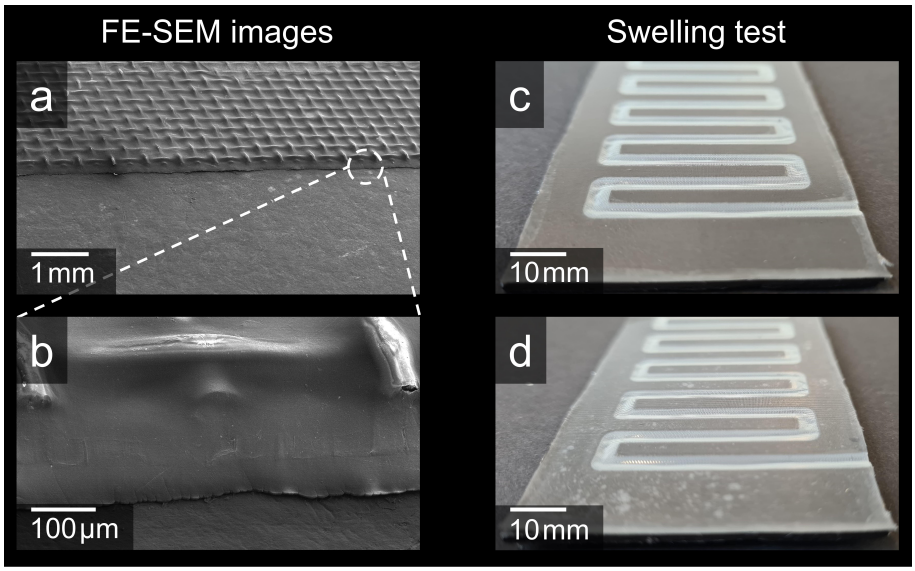

Figure 5.4: Visual investigation of bipolar plates with hot-pressed membrane. (a/b): Field emission scanning electron microscopy images of the membrane hot-pressed to the bipolar plate. (c/d): Photographs of a different sample that was used to investigate membrane swelling in ultrapure water. After seven days some light spots are visible, which show the delamination of the membrane from the bipolar plate. Overall, the membrane remained firmly attached.

no detachment of the membranes from the bipolar plates was observed.

5.3.2 FCDI Experiments

FCDI experiments were performed to compare the different current collector architectures. In the first set of experiments, newly developed BPs were compared with graphite plates (GPs) and membrane-electrode assemblies (MEAs). The arrangement of ion-exchange membranes was CEM-AEM-CEM (CAC). Fig. 5.5 (a) shows the concentration differences reached in the experiments. GP and BP show higher concentration differences in the diluate and concentrate as the MEA architecture. Fig. 5.5 (b) shows high current efficiencies above 0.95 for all architectures; current efficiencies above 1.0 are caused by inaccuracies in the concentration and mass flow measurements. However, it can be concluded that all three architectures have similarly high current efficiencies, as expected for a non-faradaic process. The average salt transfer rate (ASTR) of the BP architecture is greater than that of GPs and MEAs. BPs also have the advantage of being thinner and

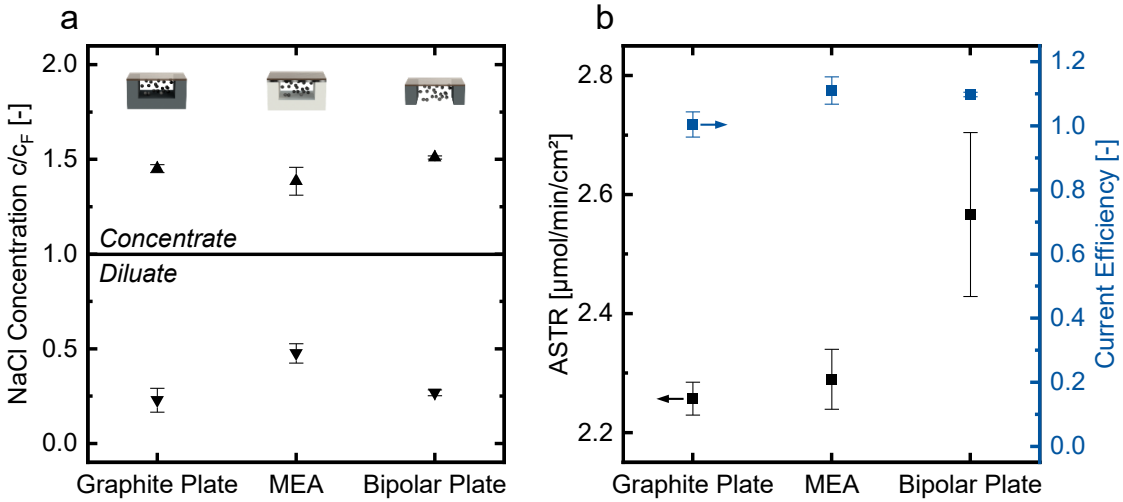

Figure 5.5: Results of FCDI experiments with the different current collector architectures investigated in this chapter. The feed flow rates of the diluate and concentrate are kept constant at 1 mL min^{-1}.

easier to manufacture (as shown in Tab. 5.1). Another advantage of the BPs lies in the flexibility of switching from CEM-AEM-CEM (CAC) arrangement to AEM-CEM-AEM (ACA) arrangement. Typically, the ACA arrangement causes problems for GP and MEA architectures when working with high chloride concentrations. The chloride ions pass through the AEMs that are adjacent to the current collectors. In the GP arrangement, the membranes are not attached to the current collectors. This causes hydrodynamic dead zones between the membrane surface and the corrugations of the GPs. In these dead zones, high chloride concentrations build up and can lead to damage of the membranes. For the GP architecture, this can be avoided by coating the top side of the corrugations with epoxy resin [Romm2015]. This is not necessary when working with BPs, since the corrugations of the flow channel are fixed to the membrane and no dead zones are generated. When switching to the ACA setup we did not observe any damage to the membranes upon disassembly. A comparison of results with the two arrangements is given in Fig. 5.6. The CAC arrangement shows higher ASTRs and greater concentration differences. This can be explained by faster transport of sodium cations. In the single-module configuration, one type of ion needs to be transported across two membranes. A faster transport of sodium would explain why the CAC setup (where sodium is transported

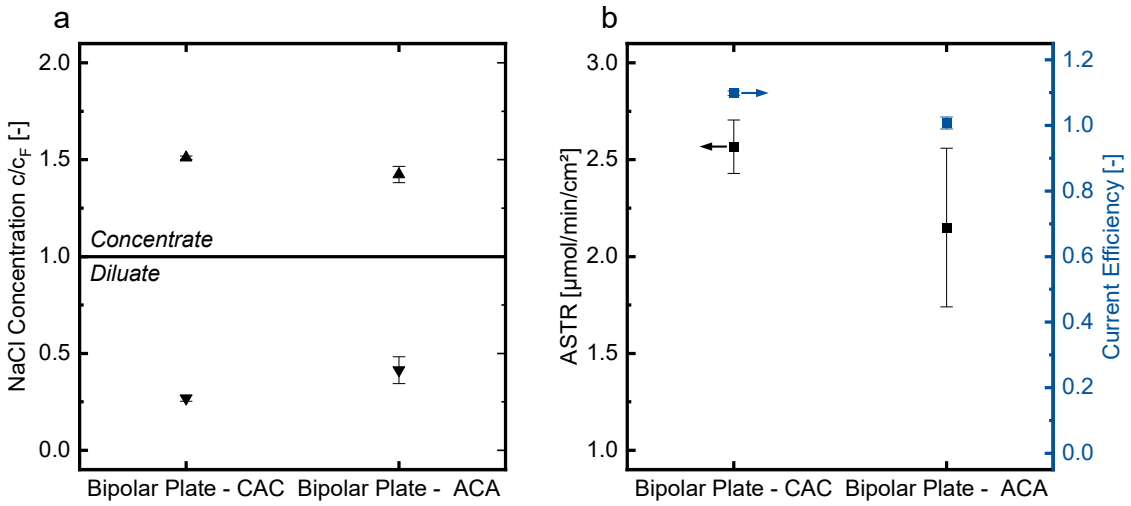

Figure 5.6: Comparison of normalized concentrations, ASTRs and current efficiencies for CAC and ACA arrangement.

across two membranes) yields higher ASTR. However, this effect is not further investigated in this chapter, since the CAC arrangement was used for all other experiments.

Interestingly, the larger electron transfer area (ETA, see Fig. 5.2) of the GPs seems not to influence the results in our comparison in Fig. 5.5. This is in line with the results obtained from the study of MEAs [Linn2020]. In that study, it was hypothesized that the close contact between the current collector and the membrane in the MEAs was the reason for the similar performance. Since this close contact is not given when using the BP, we became interested in the influence of current collector designs on the ASTR. Our goal was not to investigate the charge transport at the microscopical level but to come up with rules for the design of current collectors that enhance the salt transfer in FCDI.

When the flow-electrode composition, membranes, and operating voltage are kept constant, there are four parameters of the current collectors that can influence charge transport in FCDI: membrane area, electron transfer area, flow channel design (hydrodynamics), and current collector material. When altering current collector designs, it is difficult to vary one of the parameters independently from the others. In a first step, we deliberately shortened the flow channels of the BPs from 14 turns to 10 and 6 turns. By

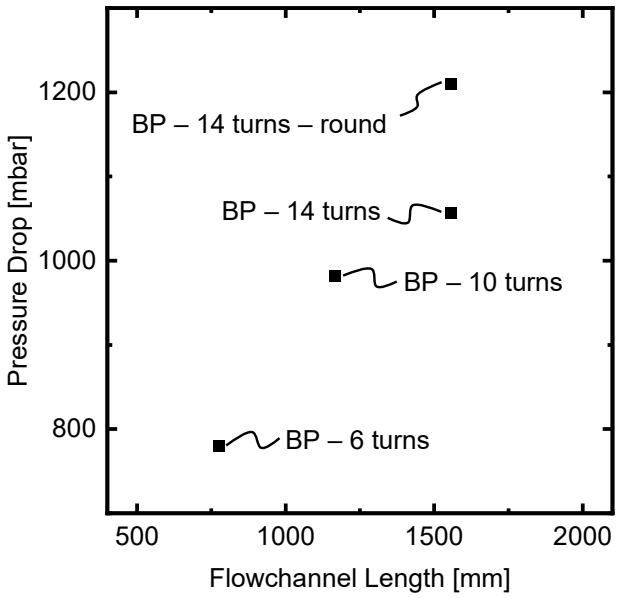

Figure 5.7: Results from pressure drop measurements for all architectures used in the comparison of hydrodynamics.

doing so, we reduced the electron transfer area, as well as the membrane area between the spacer channels and the flow electrode. Additionally, we included a geometry with 14 round turns to test the influence on hydrodynamics. Zhang et al. investigated the influence of flow channel layout on FCDI. However, their results are influenced by different flow rates of the flow electrode [Zhan2022b]. In our comparison, we kept the flow rate constant and investigated the hydrodynamics by measuring the pressure drop of the current collectors. Notably, the waterjet cutting enables easy and quick manufacturing of the different geometries. The resulting designs are shown in Fig. 5.2 (b).

The pressure drops in the flow electrode channels of these experiments are plotted in Fig. 5.7. All experiments are done with the same flow rate. The pressure drop of geometries with longer flow channels is higher. Interestingly, the pressure drop measured for the BP with 14 round turns is higher than for the standard geometry with 14 turns.

The results of the FCDI experiments are shown in Fig. 5.8. Here, concentration differences and ASTR are plotted over the electron transfer area (ETA). The ETA is defined as the sum of all conductive surface areas, where

flow-electrode particles can exchange charge with the current collectors. The current efficiency of the experiments is given to demonstrate that the experiments are not influenced by low efficiency. In Fig. 5.8 (a) and (b) the results for geometries with varied flow channel length are shown. The concentration differences and the ASTR show almost linear behavior. The same would be true for plotting them over the membrane area, since the membrane area and the ETA are geometrically linked to each other.

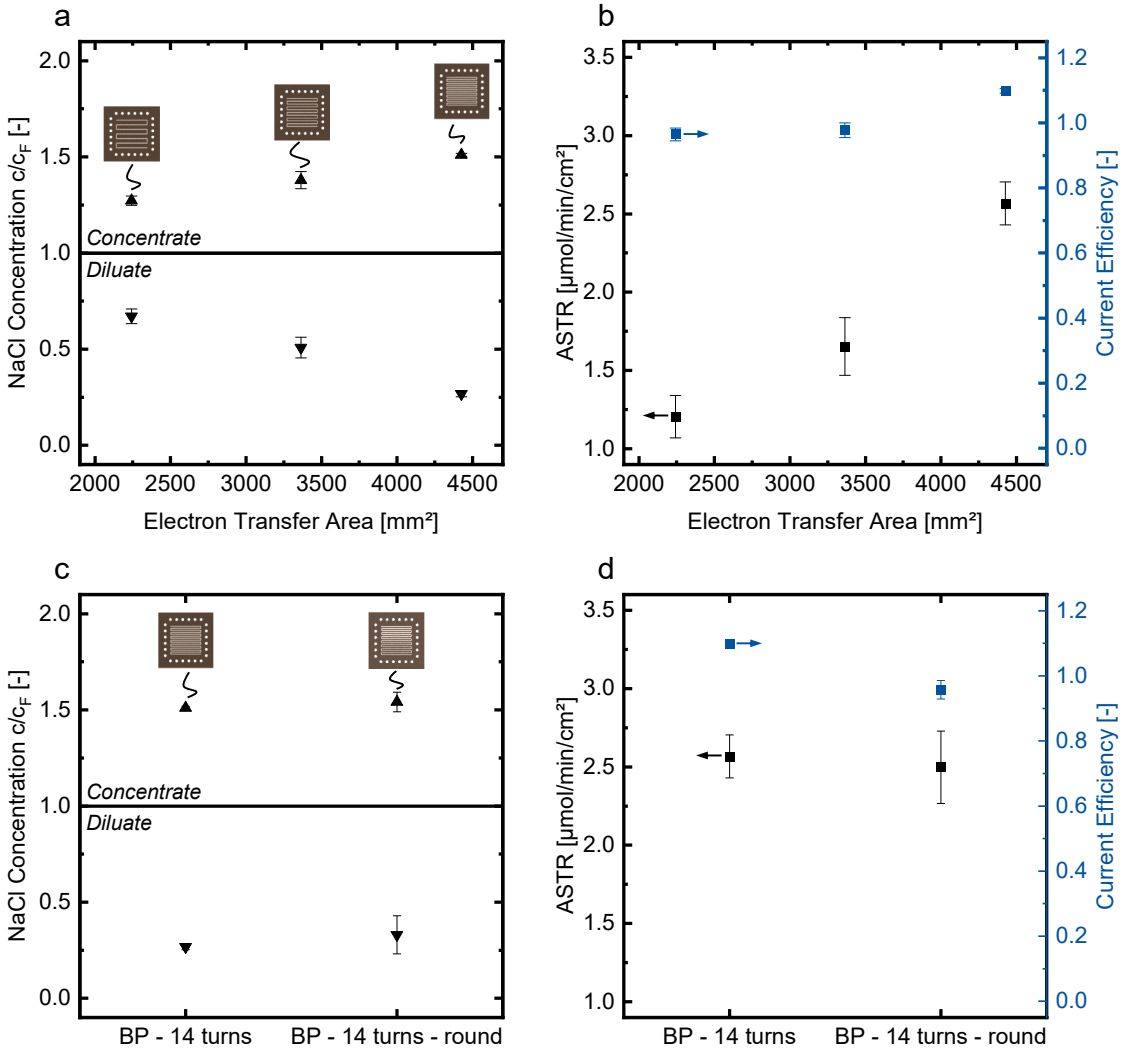

Figure 5.8: Influence of flow channel design on desalination experiments with BP architecture. (a/b): Variation of flow channel length. (c/d): Rectangular turns vs. round turns.

From these experiments, it can be concluded that (unsurprisingly) the length of the flow channel in a current collector influences the salt transfer in FCDI. This could be due to the influence of the membrane area, ETA,

or both. We assume that the membrane area is not a limiting factor for ion transport, as current densities in all experiments are around $25\,\mathrm{mA\,cm^{-2}}$, and ion-exchange membranes can be operated with current densities up to $50\,\mathrm{mA\,cm^{-2}}$ in electrodialysis [Jian2014]; [Sun2021]. This implies that the lower ETA is responsible for the lower ASTR. Future current collector designs should aim to maximize both the membrane area and the ETA. As shown here, this is possible by adding more turns to a meandering flow channel. However, the number of turns is limited by the width of the corrugations forming the flow channel. With the BP material used here, a minimum width of $3\,\mathrm{mm}$ is required to guarantee mechanical stability. Alternatively, the width of the flow channels could be minimized to achieve a higher number of turns in the same area. However, this would change the hydrodynamics of the flow electrode in the channel.

Fig. 5.8 (c) and (d) show the comparison of BPs with 14 rectangular turns and 14 round turns. There is no significant difference in the concentrations and the ASTR between these two geometries. In this case, the round corners do not improve salt transfer. Due to the higher pressure drop measured for round corners, no more experiments with this geometry are conducted. For future improvements of current collectors, the hydrodynamics in the channel could be taken into account, e.g., by CFD simulations. Geometries such as the spiral design suggested by Zhang et al. might have some merit [Zhan2022b], but for scale-up by stacking it is crucial to have both inlet and outlet close to the outer edges of the module.

Another advantage of BPs lies in the fact that the cut-through channels are open to both sides of the plate. This enables hotpressing of membranes to both sides of the expanded graphite plate. When doing so, the BPs can readily be used for stacking (in an approach with repeating flow electrode channels, as described in Chapter 3). The impact of hot-pressing CEMs to both sides of a current collector was investigated here without stacking. Two current collectors with CEMs on either side were prepared and built into a single module. This way, the CEMs facing toward the outside of the module do not contribute to charge transport. However, the setup can be

used to investigate whether such an arrangement is possible or whether the addition of a second membrane leads to clogging of the flow channel. Fig. 5.9 shows the results of the standard BP architecture in comparison to the stackable BP architecture. For stackable BP, the ASTR and concentration differences are significantly lower (ASTR 29 % lower). The flow channel of the flow electrode was less deep, as the membranes were sagging into the channel from both sides. However, no clogging was observed. More experiments in a stacked module would be necessary to evaluate whether the decreased performance would persist or if it could be remedied with a change in flow rates.

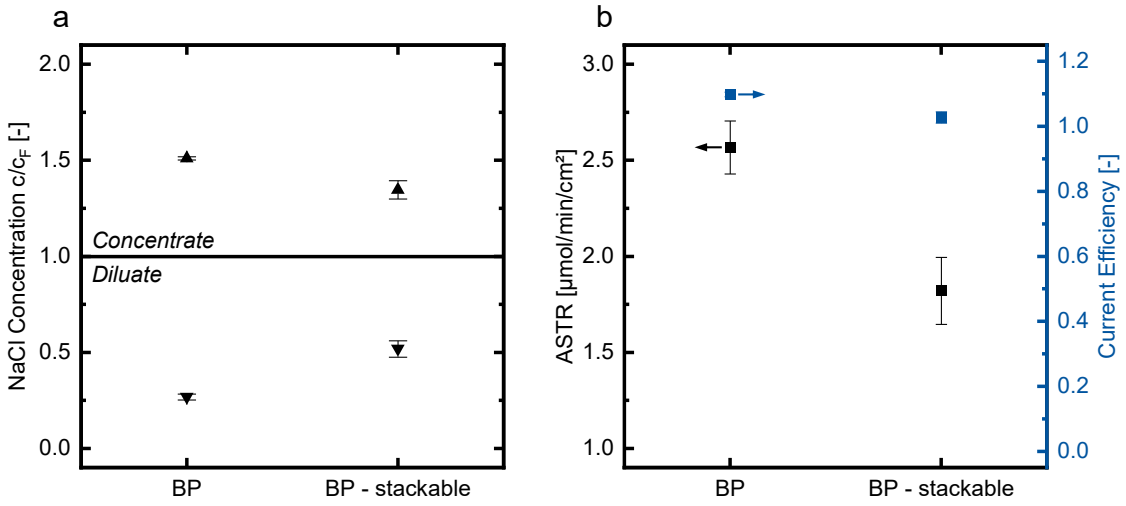

Figure 5.9: Comparison of regular BP architecture to stackable BP architecture with CEMs hotpressed to both sides of the current collector plate.

The architecture with stackable BPs is suitable for scale-up and could be used to build stacked modules, which are more cost-effective than the modules described in Chapter 3. In the scope of this chapter, we did no further experiments with this setup and instead focused on the influence of ETA on the results of FCDI experiments.

In the next step, the effect of varying the ETA without influencing the membrane area is investigated. An easy way to do this is to add a bottom wall made of conductive material to the initial BP setup. When doing this, the possibility of stacking the BPs is lost, but it could be used at the outsides of a stacked module. Alternatively, stacking three expanded graphite plates

would be possible: a middle plate without flow channel geometry and two outer plates with the flow channel geometry and membranes hot-pressed to them. Here, we used a plate cut from the stock material of our BPs without a flow channel as a bottom wall and added a standard BP with membrane on top. When the plates are pressed together in the FCDI module, a seal is formed between them without the need for gaskets. While our standard BP module has an ETA of $4426\,\mathrm{mm}^2$, the system with the bottom wall has an ETA of $9081\,\mathrm{mm}^2$. This is the same ETA as for the graphite plate architecture. In addition to the experiments with the bottom wall, we also investigated a system with a conductive bottom wall but non-conductive side walls. In this case, the side walls of the flow channel were made of polymeric material. This led to an ETA of $4655\,\mathrm{mm}^2$, the same as the MEA architecture. However, the flow channel cross-section and the membrane area remain unchanged. The flow channel geometries are shown in Fig. 5.2 (c).

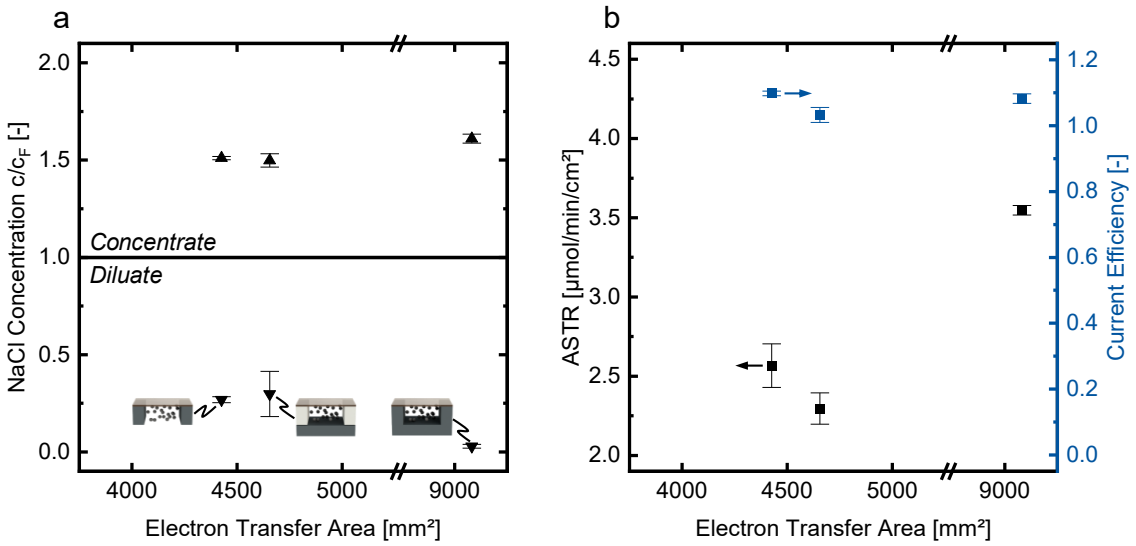

Figure 5.10: Results of desalination experiments with regular BPs, conductive bottom walls and non-conductive side walls.

The concentration differences are shown in Fig. 5.10 (a). There are no significant differences between the standard BP and the conductive bottom wall with non-conductive side walls. However, adding the bottom wall to the BP leads to a higher concentration difference. While the BP without bottom wall achieves a diluate concentration of $0.27\,c_F$ and a concentration of $1.51\,c_F$, the system with bottom wall reaches $0.02\,c_F$ and $1.61\,c_F$. This is

by far the largest concentration difference documented in our experiments and is close to the complete removal of salt from the diluate feed stream. Fig. 5.10 (b) shows high current efficiencies for all three modules. With non-conductive side walls, the ASTR is lower than with the standard BP even with a higher ETA. This result suggests that charging the flow-electrode particles at the side walls is more effective. Interestingly, the ASTR is almost equal to the result of the MEA architecture shown in Fig. 5.5 (b). For both sets of experiments, the average ASTR is $2.29\,\mu mol\,min^{-1}\,cm^{-2}$. This is consistent with expectations, since both systems have the same ETA. Therefore, the results suggest that there is no difference between charging the particles at the bottom of the flow channel or at the top close to the membrane. Further investigation in future work is required, as it can aid in the design of flow channels for FCDI or similar processes.

The BP with the bottom wall has an ETA of $9081\,mm^2$ and reaches a current density of $34\,mA\,cm^{-2}$ and the highest ASTR ($3.55\,\mu mol\,min^{-1}\,cm^{-2}$). However, the ASTR is lower than the ASTRs of the other two modules in this comparison added together. This could be due to the low concentrations of diluates reached in these experiments. Single-pass experiments lead to low diluate concentrations towards the outlet of the FCDI module. In this case, the diluate concentrations reach $1.75\,g\,L^{-1}$. Thus, there is insufficient salt left to be transported, limiting the ASTR. The direct comparison between the graphite plate and the BP with the bottom wall reveals a major disadvantage of the graphite plate architecture. Although both have an ETA of $9081\,mm^2$, the ASTR when using the BP is $55\,\%$ higher. This result cannot be explained by differences in hydrodynamics, membrane area, or ETA. Therefore, it must be caused by differences in the materials. Chen et al. hypothesized that charge transfer of graphite plates can be hindered by surface roughness and oxygen erosion of the carbon microcrystals at the surface of the graphite. They were able to improve their graphite current collectors by coating them with polyaniline [Chen2022]. Surface roughness is also a possible cause in our experiments because of the different materials and manufacturing techniques we used to obtain the current collectors.

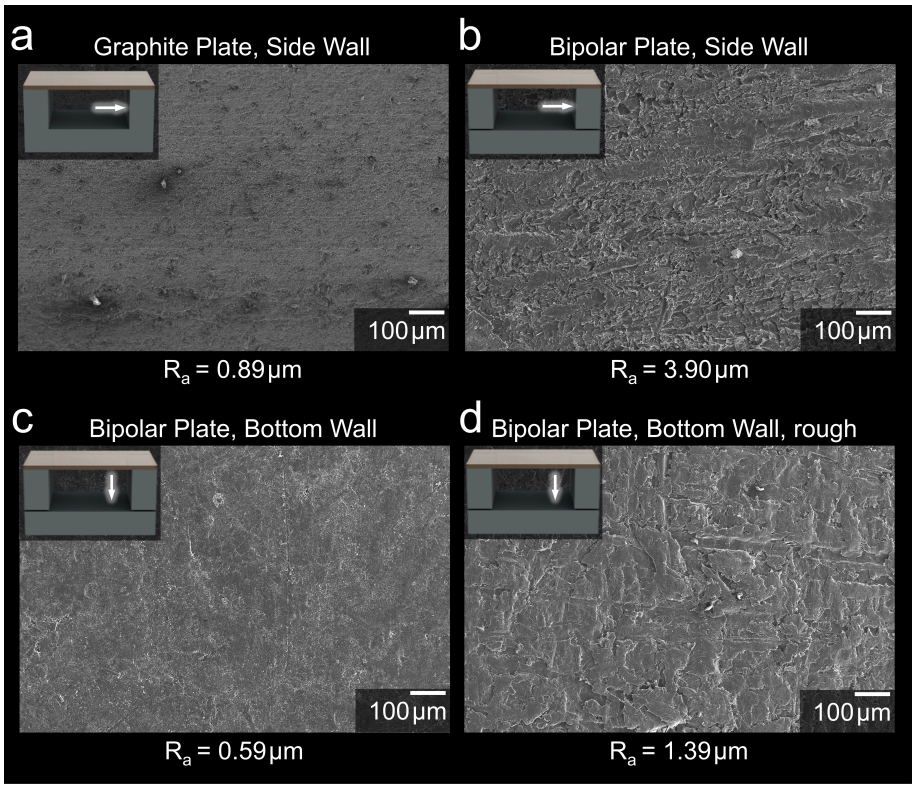

Figure 5.11: Field emission scanning electron microscopy of the surfaces of different current collectors. Arrows indicate the surfaces shown in the images. The surface roughness values R_a are measured with optical profilometry.

The difference in surface quality is investigated with field emission scanning electron microscopy (FE-SEM) and optical profilometry. FE-SEM images are shown in Fig. 5.11. The roughness values R_a beneath the images are calculated from profilometry results. The average of at least three measurements at different locations of the material is used. The untreated surface of the BP used as the bottom wall (see Fig. 5.11 c) is the smoothest surface in the comparison. The walls of the channel in the graphite current collector are manufactured by milling and are also relatively smooth (see Fig. 5.11 a). Here, the side wall is shown, but FE-SEM shows no difference in the smoothness between the side wall and the bottom wall for this current collector. The side walls of the BP are significantly rougher than the surface because they are cut with the waterjet cutter. The result of this comparison is inconclusive. The bipolar plate bottom wall is smoother than the graphite plate, but the side walls are less smooth. To investigate whether surface roughness impacts the FCDI experiments, the roughness of the bottom

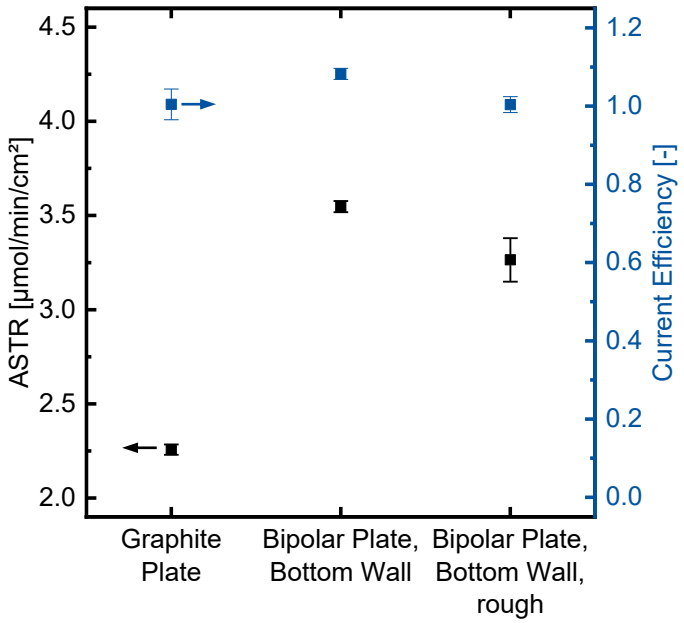

Figure 5.12: Results from experiments in which the surface roughness of the bottom wall of the bipolar plate setup is increased. The results from the graphite plate setup are given for reference.

wall is increased. Fig. 5.11 (d) shows the surface of the bottom wall after artificially increasing the roughness by treatment with sandpaper.

The impact of this artificial surface roughness on ASTR in FCDI experiments is shown in Fig. 5.12. With a rougher surface of the bottom wall, the ASTR decreases while the current efficiency remains high. However, the ASTR is still more than 40 % higher than for the graphite plate. This result supports our hypothesis that surface roughness influences current collector performance. Future research is needed to understand how surface roughness interferes with the charge transport between the current collectors and the flow-electrode particles. The roughness of the side walls needs to be included in the investigation. Additionally, long-term experiments are needed to test whether the abrasion caused by the flow-electrode particles will deteriorate the surface quality of the BPs and decrease ASTRs over time.

Typically used graphite plate current collectors show a salt transport lower than modules with membrane-electrode assemblies or BPs. The surface roughness of the graphite plates stems from the machining process and

could be avoided with a different manufacturing process or a coating. However, graphite plates are likely to remain more expensive and less well suited for scale-up by stacking.
Our work shows that there is untapped potential for improving two-dimensional FCDI current collectors. Although charge transport between current collectors and flow-electrode particles remains a challenging topic, simple constructive changes in current collectors can lead to important benefits in the FCDI process.

5.4 Conclusion

Due to the limitation of cell stacking described in Chapter 3, multiple current collectors are necessary to build an FCDI module at an increased scale. Thus, the performance and price of these current collectors become increasingly important. In this chapter, different current collector architectures are compared: graphite plates, which are typically used in FCDI research, membrane-electrode assemblies made from carbon fiber fabric, and a new type of bipolar plates made from expanded graphite. Our results show superior salt transport in modules built with the bipolar plates, which are also cheaper to manufacture than graphite plates and easier to apply than membrane-electrode assemblies. The bipolar plates can be used with an ion-exchange membrane on both sides to enable stacking. Alternatively, it is possible to add a conductive bottom wall. With the bottom wall, the surface area where the charge can be transported between the current collector and the flow electrode is equal to that of the graphite plate architecture. However, the salt transfer rate with bipolar plates is 55 % higher. We conclude that this enhancement is partially caused by the lower surface roughness of the bottom wall. Our research shows that the ideal current collector for FCDI with an activated carbon flow electrode has to have a high surface area available for charge transport, with the side walls close to the membrane contributing more to charge transport. The surfaces should be smooth; however, the influence of surface roughness on

the charge transfer process needs to be investigated in more depth in the future. Although there is a lot of research on the particles that form flow electrodes, our work shows that there is great potential for improvement in the engineering of current collectors. In future work, current collectors and flow-electrode particles could be tuned together to optimize charge transfer.

6 Local Salt Concentrations

6.1 Introduction

Membrane processes achieve the separation of components by restricting transport across the membrane to certain components. This leads to the development of concentration profiles along the membrane surface. These concentration profiles can, in turn, influence transport due to concentration gradients or osmotic pressure. Measurements of concentration changes during the operation of a membrane process are crucial to correctly operate the process and understand the processes at the membrane surface.

Electro-membrane processes that deal with the separation of ions from aqueous solutions, like Electrodialysis (ED) or Capacitive Deionization (CDI), are typically operated in batch mode [Stra2004]. This implies that the solutions undergo multiple passes through the membrane module, and the concentration changes during each pass are negligible. To monitor variations in concentration over time, it is typically sufficient to measure the concentrations at the module inlet, module outlet, or in the batch tank [Stra2004]. Because the direct measurement of ion concentrations in flow is challenging, other quantities such as the conductivity of the solution are measured. Chapter 2.6 describes Kohlrausch's law as an empirical correlation that can be used to calculate concentrations from conductivities.
However, if an electro-membrane process is operated in continuous single-pass operation, then the desired change in concentration occurs during just one pass of the membrane module. Single-pass operation may be used for Flow-electrode Capacitive Deionization (FCDI) or ED. If concentrations are measured only at the module inlet and outlet, this does not allow monitoring of concentration changes. Thus, there is no information on the local evolution of concentrations in the module. This information would be crucial for a better understanding of transport phenomena in FCDI. Because ion transport in the electric field and water transport in hydration shells as well as water transport by osmosis interact with each other, the resulting concentration profiles are non-linear.

Concentration profiles were investigated in simulations (ED: [Zour2015];

[Batt2021], FCDI: [Wang2020]). In our research group, Rommerskirchen et al. developed a process model for FCDI [Romm2018]; [Romm2020a]. This model was enhanced to allow the calculation of local salt concentrations in an FCDI module [Linn2022]. However, the predictions of the model cannot be validated in experiments because there is no method for measuring local salt concentrations.

Membrane resistances are typically measured with reference electrodes or thin metal wires [Geis2014]; [Gala2016]. However, this only allows to characterize the membrane conductivity (which to some extent depends on the surrounding salt concentration) but not the salt concentration in the module. Segmented ED modules can be used to achieve local resolution of currents and concentrations [Door2020]; [Fili2023]. No further attempts at measuring local salt concentrations in electro-membrane processes are documented in literature. However, in other fields of research, measurement techniques like wire mesh sensors (WMS) and electrical impedance tomography are applied to resolve local resistances [Vela2015]; [Mila2020]. More detail on WMS is given in Chapter 2.6.3.

This chapter describes WMS that can be used to measure resistances in a spacer channel. These resistances can then be used to calculate salt concentrations. The chapter details the first application of this device and showcases the results of its evaluation.

6.2 Experimental

In this chapter, a setup for the investigation of local salt concentrations in narrow spacer channels is developed. The setup is based on wire mesh sensors (WMS), which are described in Chapter 2.6.3. In the literature, conductive WMS was used to measure salt concentrations in liquids [Höhn2006]; [Klie2008b]. Therefore, conductive WMS is also applied in this work. The flow geometry of the narrow spacer channel is similar to the channels studied in the work of Ito et al. [Ito2011]. The flow channel in their work had a width of 25 mm and a depth of 3 mm. The spacer channels

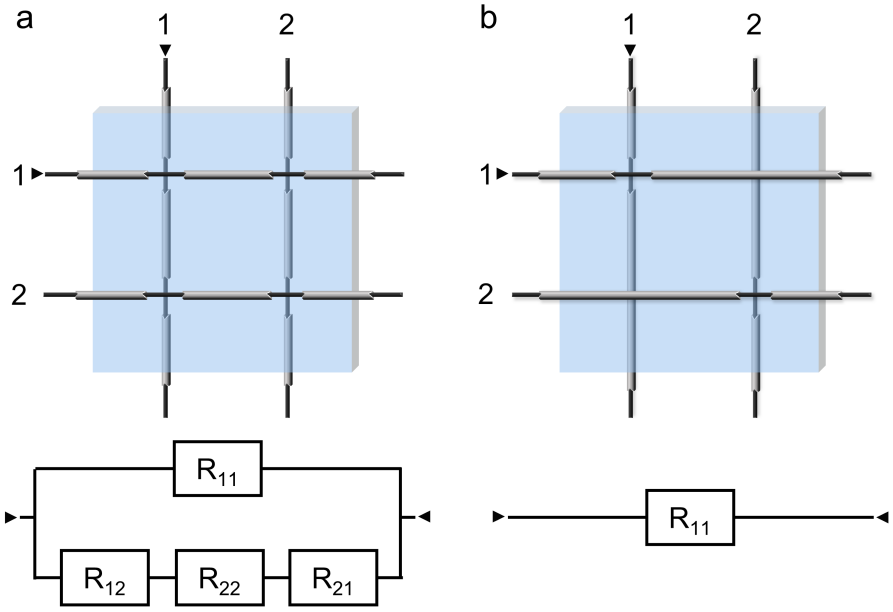

Figure 6.1: Design of WMS for concentration measurements. (a): Wire isolation is removed at all crossing points resulting in four points for measurement and the equivalent circuit below. (b): Wire isolation is removed at only one location for each wire, resulting in two measuring points and a circuit with just the investigated resistance R_{11}.

used in FCDI are even narrower, with a depth of just 500 µm. We adapted their approach by placing transmitter and receiver wires on either side of the spacer channel.

A common problem in WMS is cross-talk between measuring points. Literature recommends placing the electrodes sufficiently far apart to minimize the amount of cross-talk and amplifying the desired signal with operational amplifiers [Vela2015]. In our initial tests, we used a setup with two planes of two wires each, leading to four measuring points. With an increasing number of wires (n_W) the number of measuring points would increase according to $n_P = (\frac{n_W}{2})^2$. Isolated platinum wires (diameter 125 µm with 14 µm thick polyester insulation, Goodfellow Cambridge Ltd.) were used. The isolation was removed locally at the measuring points. The design is depicted in Fig. 6.1 (a).

The wires were attached to a potentiostat (Reference 3000™, Gamry Instruments Inc.) to perform electrochemical impedance spectroscopy and yield local solution resistances at the wire crossing points. However,

this initial design was flawed, as it led to the equivalent circuit shown in Fig. 6.1 (a). When measuring between the two first wires marked with triangles, the desired resistance R_{11} is in a parallel connection to the series of R_{12}, R_{22}, R_{21}. Since all resistances are in the same range, this leads to a resistance measurement that is approximately $25\,\%$ lower than the correct value for R_{11}. If all other values are known and stay constant over time, measurements could be corrected in a post-processing step. However, the local resistances in an FCDI module will change over time. Thus, this initial setup was not suited for the application in FCDI. In the future, the cross-talk between the measuring points could be reduced by applying an external circuit with operational amplifiers. Instead, we decided to use a setup where the isolation of each wire is only removed in one place, as shown in Fig. 6.1 (b). This yields the two measuring points R_{11} and R_{22} that are independent from one another. This enabled measurements without cross-talk between the measuring points. However, the number of measuring points now only scales with $n_P = \frac{n_W}{2}$.

In the next step, the test cell was changed to a module that allowed clamping of a spacer from an FCDI module and four wires in each plane, yielding a WMS with four individual measuring points (P1-P4). The module had a transparent upper plate, which allowed visual examination of the fluid in the spacer. The setup is shown in Fig. 6.2. An Arduino-controlled circuit (Arduino Board Mega 2560 Core) was designed to automatically switch between measuring points. The circuit diagram is given in the Appendix. The wires and the spacer were clamped in the module and a leakage test was performed. Before an experiment was started, the measuring points were calibrated. Individual calibration of each measuring point is necessary since the distance between the wires cannot be assumed to be constant. Calibration was done by flooding the spacer with a solution of known concentration and measuring the resistances at all four measuring points. Then the solution was flushed out of the module and replaced by the next solution. In our experiments, we expected concentrations in a range of $25\,\mathrm{g\,L^{-1}}$ to $40\,\mathrm{g\,L^{-1}}$. Thus, sodium chloride (NaCl) solutions with $25\,\mathrm{g\,L^{-1}}$, $30\,\mathrm{g\,L^{-1}}$, $35\,\mathrm{g\,L^{-1}}$ and $40\,\mathrm{g\,L^{-1}}$ were used for calibration. The resistances $R_{i,j}$

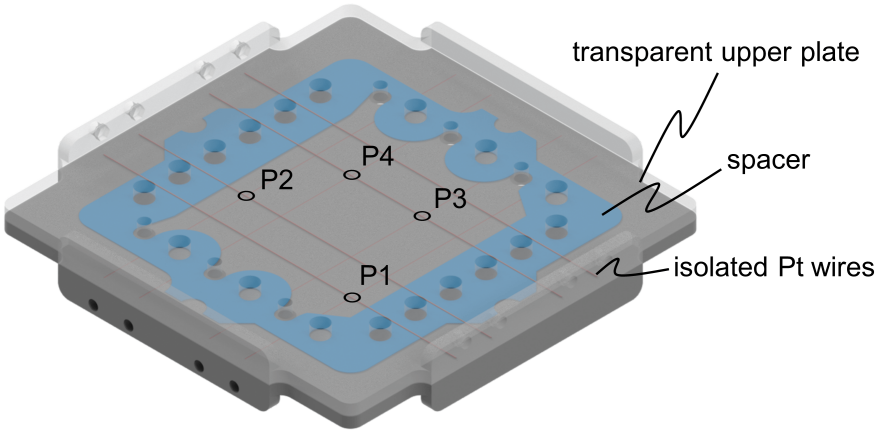

Figure 6.2: Test cell for wire mesh sensor with four individual measuring points. Pt wires (shown in red) are separated by a typical ED100 spacer for FCDI experiments.

for the $i = 1..4$ measuring points with all $j = 1..4$ solutions were measured. Each measurement was repeated five times. For each measuring point, a Belehradek-type function was fitted to the data. The function is a power law, as shown in Eq. 6.1. It should be noted that the fitting function does not describe a physical correlation between concentration and resistance. However, it was generally found to fit the data better than Kohlrausch's law (see Eq. 2.12). In the next step, the fitting curves can be used to calculate concentrations from the resistances measured in experiments.

$$R_{i,j} = a_i \cdot (c_{NaCl,j} - b_i)^{c_i} \tag{6.1}$$

In the experiments, solutions were flushed into the spacer with syringes or with a peristaltic pump (REGLO ICC Digital Peristaltic Pump 2-Channel, Cole-Parmer Instrument Company LLC.) and the resistances at the measuring points was measured. Some solutions are mixed with a dye to allow visual examination of fluid mixing. The dye Tartrazine (C.I. 19140, Carl Roth GmbH & Co.KG) is used. The influence of $1\,w\%$ Tartrazine on the conductivity of a solution with a concentration of $25\,g_{NaCl}/L$ was investigated with a conductivity probe. It was found that the addition of the Tartrazine increases the conductivity from $36.26\,mS\,cm^{-1}$ to $40.07\,mS\,cm^{-1}$. This increase in conductivity has to be taken into account in the evaluation of solutions

colored with Tartrazine. The higher conductivity of the colored solutions leads to lower resistances in the measurement. Thus, the concentrations of colored solutions are overestimated. In the experiments, the resistances of the measuring points were measured sequentially. Each measuring point was measured five times, and the average was used for evaluation.

6.3 Results and Discussion

6.3.1 Calibration and Verification

Calibration of the individual measuring points was performed with sodium chloride (NaCl) solutions. The concentrations were $25\,\mathrm{g\,L^{-1}}$, $30\,\mathrm{g\,L^{-1}}$, $35\,\mathrm{g\,L^{-1}}$ and $40\,\mathrm{g\,L^{-1}}$. The results are plotted in Fig. 6.3 (a). The results of P1, P3, and P4 are comparable with each other; the resistances measured at P2 are lower. This might be a result of a lower distance between the wires. Calibration curves were fitted to the data as described in Section 6.2. The resulting calibration curves are plotted in Fig. 6.3 (b), the fitting parameters a_i, b_i, c_i, and the goodness of fit R^2 are given in Tab. 6.1.

A first experiment was used to verify the independence of the four measuring points. Salt solutions were pumped into the module so that first only P1 was wetted with the solution, and the resistance at P1 was measured. The module was then filled further, so that successively also P2-P4 were in contact with the solution. Again, the resistance at P1 was evaluated to verify the independence of P1 from the other resistances. Fig. 6.4 shows the resulting resistances. The resistances measured in P1 remain constant;

Table 6.1: Parameters a,b,c of the Belehradek functions used to fit the data from the calibration of P1-P4.

	P1	P2	P3	P4
a_i	14313.99	17111.88	400.37	6878.39
b_i	-25.54	-29.85	4.45	-20.16
c_i	-1.42	-1.46	-0.66	-1.27
R^2	0.9808	0.9655	0.9937	0.9895

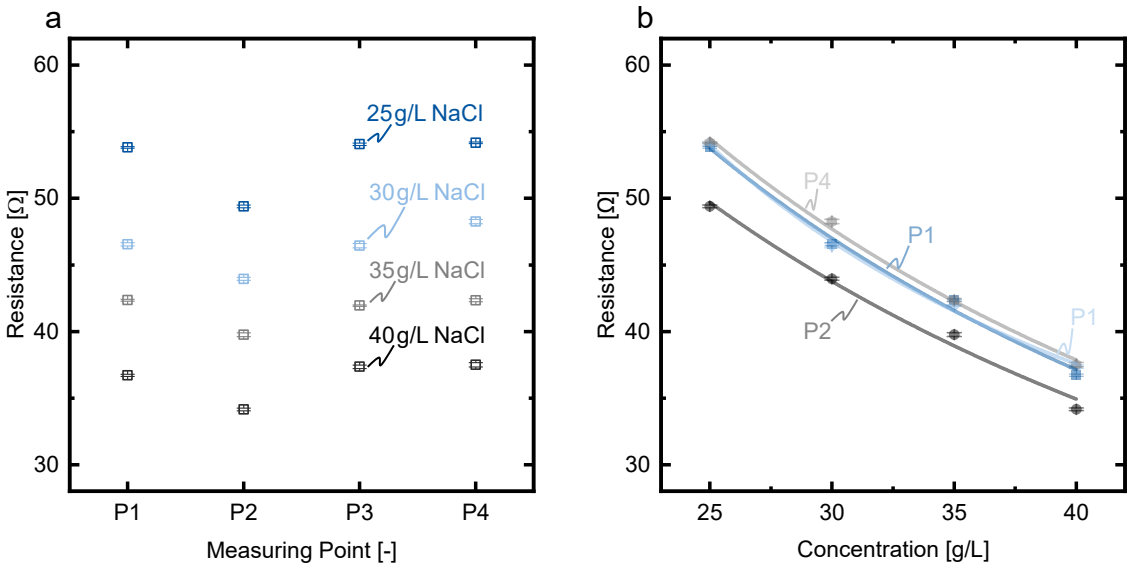

Figure 6.3: Results from the calibration of the WMS. (a): Resistances measured for four different salt concentrations. (b): Fitting curves calculated for the measuring points P1-P4.

the largest difference in resistance is detected when filling the module with $25\,g_{NaCl}/L$. The maximum deviation between the measurements (P1) and (P1,P2,P3,P4) is $1.2\,\%$, a parallel connection as shown in Fig. 6.1 (a) is avoided.

In conclusion, the WMS in the test cell enables independent measurements without cross-talk. In the next step, the test cell is subjected to changing concentrations to evaluate the time-dependent behavior of the measuring points.

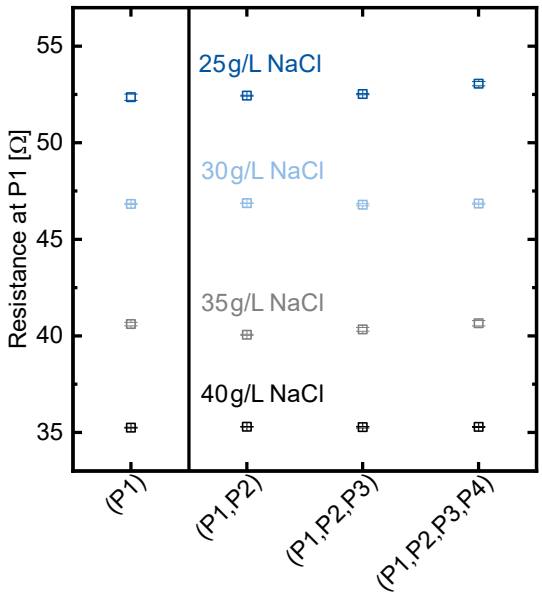

Figure 6.4: The independence of the resistance at P1 from P2-P4 is investigated by increasing the amount of solution in the module stepwise so that the number of wetted measuring points increases.

6.3.2 Diffusion

The first possibility to induce a time-dependent change of concentrations in the module is diffusion between two salt solutions with different concentrations. At the start of the experiment, the module was completely filled with a solution with a concentration of $25\,g_{NaCl}/L$. Then a syringe was used to inject $3\,mL$ of a solution with a concentration of $40\,g_{NaCl}/L$ at the inlet closest to P4. The solution was colored with Tartrazine to visually track the diffusion. During the first $60\,min$ of the experiment, resistances were measured every $5\,min$, then the intervall was increased to $10\,min$. The concentrations calculated from the resistance measurements are plotted in Fig. 6.5. The initial concentrations before the start of the experiment are given at $t = -0.5\,min$. P1 and P4 measure close to $25\,g_{NaCl}/L$, while P2 and P3 are shifted. Then, the colored solution with $40\,g_{NaCl}/L$ is introduced, so that P4 is placed within this solution. The concentration at P4 is initially calculated at $38.90\,g_{NaCl}/L$ and then decreases steadily. After $180\,min$ a concentration of $30.58\,g_{NaCl}/L$ is reached.

Diffusion in the module does not occur uniformly, as evidenced by photographs taken during the experiment (see Appendix). This is likely caused

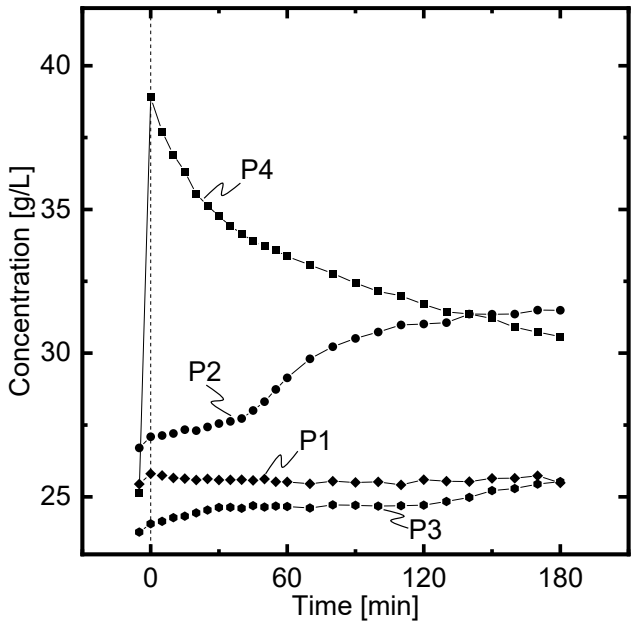

Figure 6.5: Trajectories of the concentration at the measuring points P1-P4 during diffusion of a $40\,g_{NaCl}/L$ solution starting from P4.

by the spacer mesh influencing the direction of diffusion. P2 is reached first and the concentration starts to increase from an initial concentration of $26.7\,g_{NaCl}/L$ to a final concentration of $31.5\,g_{NaCl}/L$. The concentration at P3 is initially underestimated with $23.8\,g_{NaCl}/L$ and then rises to a final value of $25.5\,g_{NaCl}/L$. The concentration measured at P1 stays almost constant throughout the experiment ($25.5\,g_{NaCl}/L$). This corresponds well with the visual examination of the diffusion front, which does not reach P1 during the experiment (see Appendix). Overall, the WMS seems capable of correctly detecting time-dependent concentrations in the module.

6.3.3 Convection

The main goal of the WMS setup is to measure the concentration changes during flow in an FCDI module. Another experiment was devised to test the applicability of the WMS in flow. In the beginning of the experiment the test cell was filled with a solution with a concentration of $30\,g_{NaCl}/L$. The module was set up vertically, as in an FCDI experiment. Then a solution with $40\,g_{NaCl}/L$ was pumped into the module from bottom to top. This solution

was mixed with Tartrazine. Resistances at all measuring points were measured in 30 s intervalls. The calculated concentrations are given in Fig. 6.6. The initial concentrations before the start of the experiment are given at $t = -0.5\,\text{min}$. P1 and P4 measure close to $30\,\text{g}_{\text{NaCl}}/\text{L}$. P2 and P3 measure higher concentrations throughout the entire experiment. This is likely caused by an outdated calibration. Calibration should be repeated before an experiment to check if the fitted curve is still correct.
At P1, the rise in concentration starts directly. In the beginning the change in concentration is greater and then drops of until the final concentration of $40\,\text{g}\,\text{L}^{-1}$ is reached. The onset of concentration change in P2 and P3 corresponds with the visual examination through photographs. However, the final concentrations that are obtained at these measuring points are unreasonably high. The results for P4 match the expectations from the visual examination.

Overall it becomes clear, that four measuring points are not enough to fully evaluate the mixing between the stationary solution and the inflowing solution. More measuring points would be necessary, e.g., to evaluate the effect of a lower flow rate at the right spacer outlet, which becomes visible after 4 min (see photographs in Fig. 6.6). More measuring points would also increase the reliability since unreasonable results could be excluded from the evaluation.

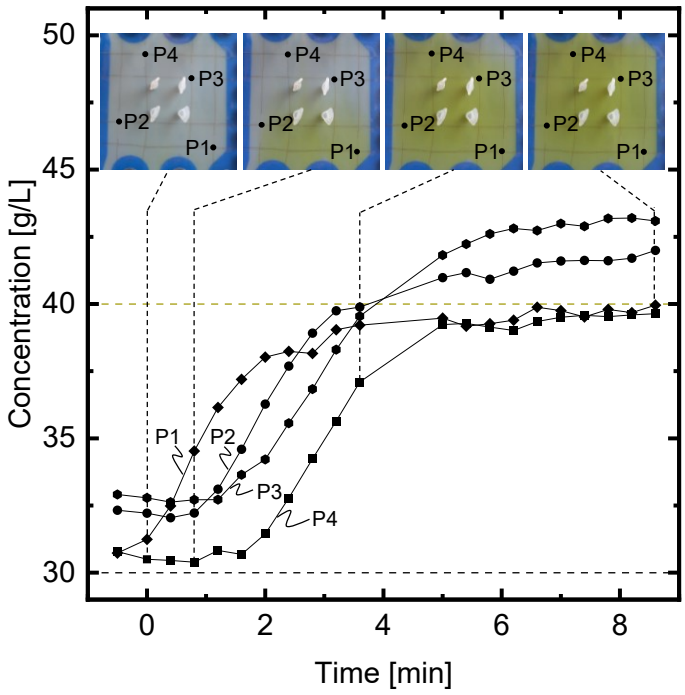

Figure 6.6: Trajectories of the concentrations at the measuring points P1-P4 during the convection experiments. The photographs show the inflow of the yellow colored salt solution with $c = 40\,\mathrm{g_{NaCl}/L}$.

6.4 Conclusion and Outlook

The concept of Wire Mesh Sensors (WMS) is known for 37 years. The application of these sensors mostly focuses on two-phase flow with high differences in resistance between the phases (e.g., water and air). We applied a WMS grid in a spacer channel to measure differences in salt concentration. The results documented in this chapter should be seen as first tests in the design and application of such a sensor. Our sensor enables the measurement of the concentrations of stationary salt solutions with good reproducibility. However, in more complex applications such as flowing salt solutions the design is held back by too low resolution. This could easily be fixed in the future by the addition of more wire pairs. Currently, two wires are necessary to form one crossing point that is used for the measurement. With more sophisticated electronics or a multi-electrode array, measurement at each crossing point of the wires could be enabled, raising the number of measuring points in a test cell from $\frac{n_{wire}}{2}$ to $\frac{n_{wire}^2}{2}$. This would greatly improve the local resolution of the sensor. Currently platinum

wires are used for the wire mesh since the material is conductive, corrosion-resistant, mechanically stable, and easy to solder. However, platinum wire is expensive and other materials should be investigated to lower the cost of the WMS. This would aid the application of these sensors in FCDI and other electrochemical desalination processes that depend on a change in local concentration across the desalination module. Reliable concentration measurements can in the future improve the understanding of salt transport in these processes and lead to advanced module designs.

7 Summary

7.1 Reflections on the State of FCDI Research

More than 10 years have passed since the first mention of Flow-electrode Capacitive Deionization (FCDI) in literature. In these years, the technology has received growing academic interest. Advantages such as high energy efficiency, low cost, and continuous operation of a capacitive desalination process are perceived. However, the field of commercial desalination is fairly conservative, and technological progress occurs slowly. This is evidenced, for example, by the slow but steady increase that allowed Reverse Osmosis to replace thermal processes as the main desalination technology. The conservative environment and the competition by well-established processes like Electrodialysis (ED) slow the application of FCDI to real-world separation problems.

The demand for desalination and salt concentration processes can be expected to increase in the future with the prospects of water scarcity and stricter environmental regulations that require salt recycling. The application of FCDI to these real-world tasks is critically relevant to develop the technology towards market demand. For every new technology, scale-up is an important prerequisite for the application to real-world problems. This is especially true for FCDI, which is typically researched at lab scale with production rates in a range of milliliters to liters per hour. So far, literature on FCDI scale-up in real-world applications is scarce. This thesis aims to provide a roadmap for scale-up and application. In this final chapter, the results are summarized, conclusions are drawn, and an outlook on the future of FCDI is given.

The thesis contains four chapters that focus on different aspects of FCDI scale-up. Chapter 3 deals with the design of a modular plate-and-frame type FCDI module. The stacking design is inspired by ED; however, due to the unique nature of capacitive deionization and the use of flow electrodes, the design deviates from a typical ED module. Two-sided flow channels for the flow electrode are used as repeating elements in the module stack. Subsequently, stacked modules with increased membrane area are built

and tested. The comparison to FCDI modules on lab scale shows that the achieved salt transfer rates do not scale linearly with the increasing membrane area. The final FCDI module has a $267\times$ higher membrane area than modules at lab scale; however, the salt transport rate is only increased by a factor of 127. This has a significant impact on the cost effectiveness of the module. The diminished specific salt transport rate in pilot-scale FCDI modules needs to be considered in future scale-up of applications from lab scale.

An important disadvantage of FCDI compared to ED is lower ion transport per membrane area in stacked plate-and-frame modules. This is shown in Chapter 3 through a thought experiment. The consequences of this thought experiment are serious: with the state-of-the-art plate-and-frame module design, FCDI will always require more total membrane area than ED. Because the cost of the ion-exchange membranes has a significant share in the total cost of a module, FCDI modules will always be more expensive than ED modules. However, a possible economic advantage of FCDI lies in the lower energy demand for desalination. To compare the two processes with each other, rigorous application and testing on pilot scale is necessary.

The systematic approach to pilot-scale testing of FCDI is described in Chapter 4. The chapter focuses on the application of FCDI to the desalination and recycling of wastewater from a stainless steel treatment plant. The chapter starts with a series of lab-scale experiments that were conducted early in the project to evaluate the applicability of FCDI to the separation task. The goal was to establish a methodology that could also be applied to other novel separation tasks in the future. Based on the results from this chapter, the required membrane area for FCDI modules on pilot scale was calculated. Since these calculations were done before pilot-scale modules could be built and tested (scope of Chapter 3), these calculations did not reflect the losses that occur during scale-up. Together with the complicated production process of the modules, this led to an inadequately low treatment capacity of the FCDI modules during the piloting phase of the project.

The results of a 30 d trial under real-world conditions are detailed in the chapter. The applied membrane area was too low to sufficiently treat the feed solutions; the unsuitability became especially apparent on the diluate side of the process where a higher concentration difference needed to be overcome. Since ED was also tested for the same application in the project, a direct comparison of the two technologies became possible. The productivity of an ED stack with 30 % greater membrane area (ED: $A_{mem} = 4.14\,\mathrm{m}^2$, FCDI $A_{mem} = 3.20\,\mathrm{m}^2$) was roughly a factor of 20 higher. Due to the significant difference in productivity and the difference in the outlet concentrations obtained, a comparison of the energy demand is not constructive. However, it is impossible for the energy advantage of FCDI to offset the severe economic disadvantage of requiring about 15× more membrane area to reach the same productivity as ED.

The overall prospects for FCDI at the end of this project are bleak. In the first pilot-scale application of the process, FCDI was unable to demonstrate its effectiveness in comparison to an established technology. However, FCDI is still a young technology and significant advances might be made in the future. Research on different flow electrodes carried out by research groups around the world is especially promising for the future of FCDI. The introduction of intercalation materials and redox couples to the flow electrodes yields a process that is no longer based purely on capacitive ion storage but has improved salt removal rates at a still relatively low energy demand. As discussed in Chapter 3 a two-module approach could be taken to reduce the impact of undesired water transport between diluate and concentrate in FCDI. However, the main disadvantage in the comparison to ED is the insufficient utilization of the membrane area described in the thought experiment in Chapter 3. This is a fundamental problem of stacked plate-and-frame FCDI modules that can only be overcome with novel reactor concepts. From today's perspective, modules with increased membrane cross-section, tubular membrane modules or swiss-roll-type modules appear to be the most promising. These modules would increase the membrane area of FCDI without stacking. However, these concepts would need to be tested rigorously both in terms of desalination performance and eco-

nomic viability.

Pilot-scale testing also exposed specific advantages of the FCDI technology over ED. Because hydrogen gas production is omitted, the safety regulations for FCDI are lower. This renders operation of FCDI easier than ED. In the pilot-scale application that is the focus of Chapter 4, this advantage was not relevant since the trials were conducted in a facility that was already fulfilling the necessary safety regulations. However, this advantage might become more important in other applications of FCDI. Overall, the early pilot-scale application of FCDI technology led to a better understanding of the process, its chances, and potential pitfalls. Pilot-scale tests should form a major part of FCDI research in the future.

Chapters 5 and 6 of this thesis aim to make progress in some fields where incremental improvements might facilitate the application of FCDI in the future. Chapter 5 poses the question of how the cost-effectiveness of FCDI could be improved with new materials. Current collectors are often overlooked in the research on FCDI; however, they become increasingly important in scale-up concepts such as the one presented in Chapter 3. By using thin bipolar plates made of expanded graphite, the workflow of manufacturing can be simplified, and the cost is lowered. Through the direct combination of the current collector, the flow channel for the flow electrode, and the membrane in one single part, the modules become easier to build. The newly developed bipolar plate current collectors are compared to established graphite plates and membrane-electrode assemblies in lab-scale experiments and yield superior salt removal rates. The reason for the increased salt removal is found in the better contact of the flow-electrode particles at the surface of the bipolar plates. This has implications for the design of current collector and flow electrode systems in the future and could be used as a starting point to develop a system where the current collector and flow electrode are optimized together to enhance the capabilities of FCDI.

Chapter 6 is the first approach to answer a more fundamental question about phenomena that occur in FCDI and other electro-membrane pro-

cesses. The interplay of ion transport and water transport during the operation of the processes makes the prediction of local salt concentrations in the modules challenging. This is especially problematic for processes that are operated in continuous single-pass operation, with high concentration differences between module inlet and module outlet. A better knowledge of local salt concentrations could help to improve and tailor FCDI modules in future. Thus, the application of wire mesh sensors to membrane spacers, as they are used in FCDI or ED, is investigated in Chapter 6. The results have to be seen as a test case, but they are promising. With improvements in the existing sensor design, it will be possible to measure local salt concentrations during FCDI operation in the future. This will help to improve the modules, especially for single-pass operation, which might pose another advantage of FCDI over ED. However, these sensors could also be applied to a variety of other processes where local changes in salt concentration are involved. Thus, these sensors could potentially reach beyond the topic of FCDI.

7.2 Outlook

Although the superiority of FCDI could not be shown in this thesis, there are reasons to remain hopeful for the future of this desalination technology. Research continues to show again and again that incremental changes lead to significant improvements in the process. The interaction of flow-electrode particles in charge transport is still insufficiently understood. Future research should try to elucidate these phenomena so that a targeted approach can be taken to the tailoring of flow electrode systems. Furthermore, there is a need for a set of standard experiments to compare the ever-growing number of reported flow electrodes and FCDI modules with each other and to enable goal-oriented development. Scale-up should be an important goal for every researcher working in this field. If the capabilities of the FCDI process are not explored in real-world applications, the process is unlikely to remain relevant 10 years from now. Different appli-

cations in industry lend themselves to the application of desalination. Ion recovery is now becoming increasingly relevant due to the increasing prices of raw materials, stricter environmental regulations, and new applications such as the recycling of Li-Ion batteries. If more research is conducted on pilot scale, this might lead to a certain application where FCDI has a unique advantage over established technologies. Then the development of the technology could be aimed towards this niche. However, real-world application of FCDI is only possible with pilot-scale or industrial-scale modules. Thus, new concepts for FCDI scale-up like tubular modules, swiss-roll modules, or completely new approaches to module design need to be investigated.

Even if the time has not yet come for FCDI to enter the market as a successful technology, there might come a second chance in the future. Its predecessor, Capacitive Deionization (CDI), was intensively researched in the 1960s only to be almost completely abandoned for 40 years. Then, new developments like the availability of durable and comparatively low-price ion-exchange membranes allowed the technology to enter the desalination market. There is no reason to suspect that a similar development could not occur for FCDI. The demand for an energy-efficient tool to produce drinking water and close material cycles through salt recycling will only increase in the future and poses a great challenge to human ingenuity.

8 Appendix

Correlation Density - Concentration

The correlation between the density of the solution and the sodium chloride (NaCl) concentration allows quick and robust measurement of the sample concentrations. Densities are measured with a handheld densitometer (Densito 30PX, Mettler-Toledo International Inc.). All sample densities are measured three times; the average value is used to calculate the NaCl concentration according to the calibration curve shown in Fig. 8.1.

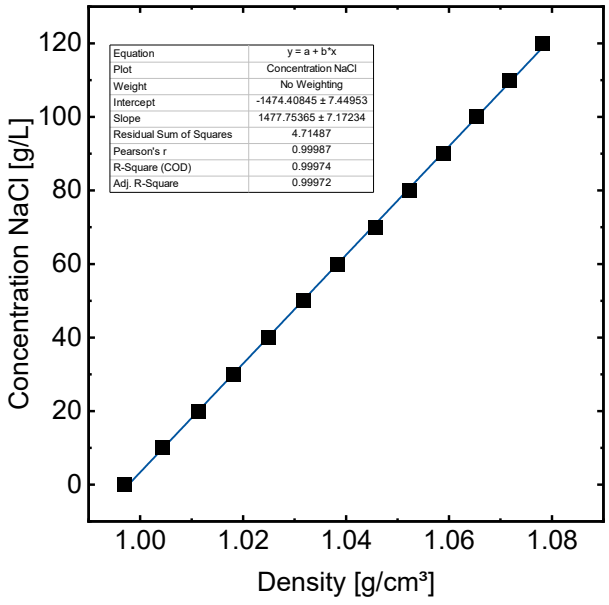

Figure 8.1: Calibration curve used to correlate the sample density with the sodium chloride concentration.

Circuit Diagram Relay Box

The experiment documented in Chapter 6 are enabled by a circuit that allows switching between several measruing points in a fast sequence. This circuit is based around an Arduino Mega microcontroller (Arduino S.r.l.). The circuit can be used with relays as displayed in the circuit diagram in Fig. 8.2 or with optocouplers. The circuit is connected directly to the potentiostat. The software which controls the potentiostat (Gamry Framework, Gamry Instruments Inc.) is used to also control the Arduino to enable the switching from one measuring point to the next.

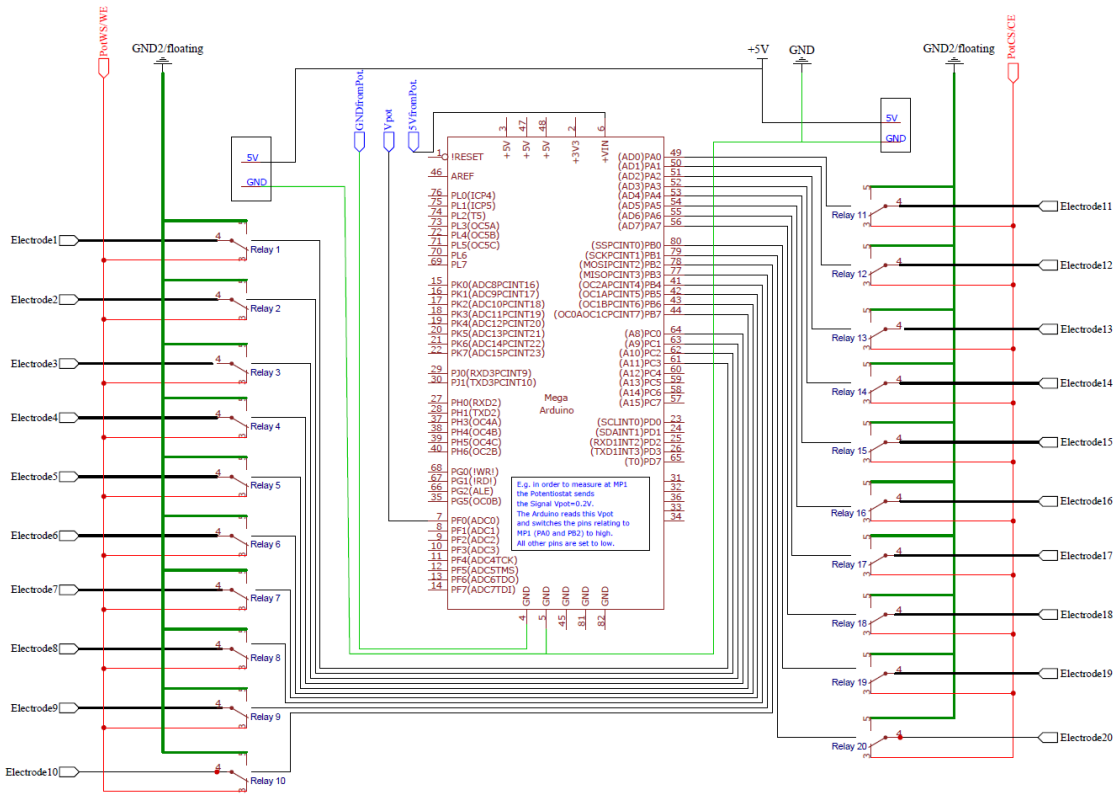

Figure 8.2: Circuit diagram of the relay box used for switching between individual measuring points.

Photograph Series from Diffusion Experiment

During the diffusion experiment detailed in Chapter 6, photographs are taken to investigate the mixing between the solution with $25\,g_{NaCl}/L$ and the yellow colored solution with $40\,g_{NaCl}/L$. Some of these phtographs are given

in Fig. 8.3. The postions of the measuring points P1-P4 are marked.

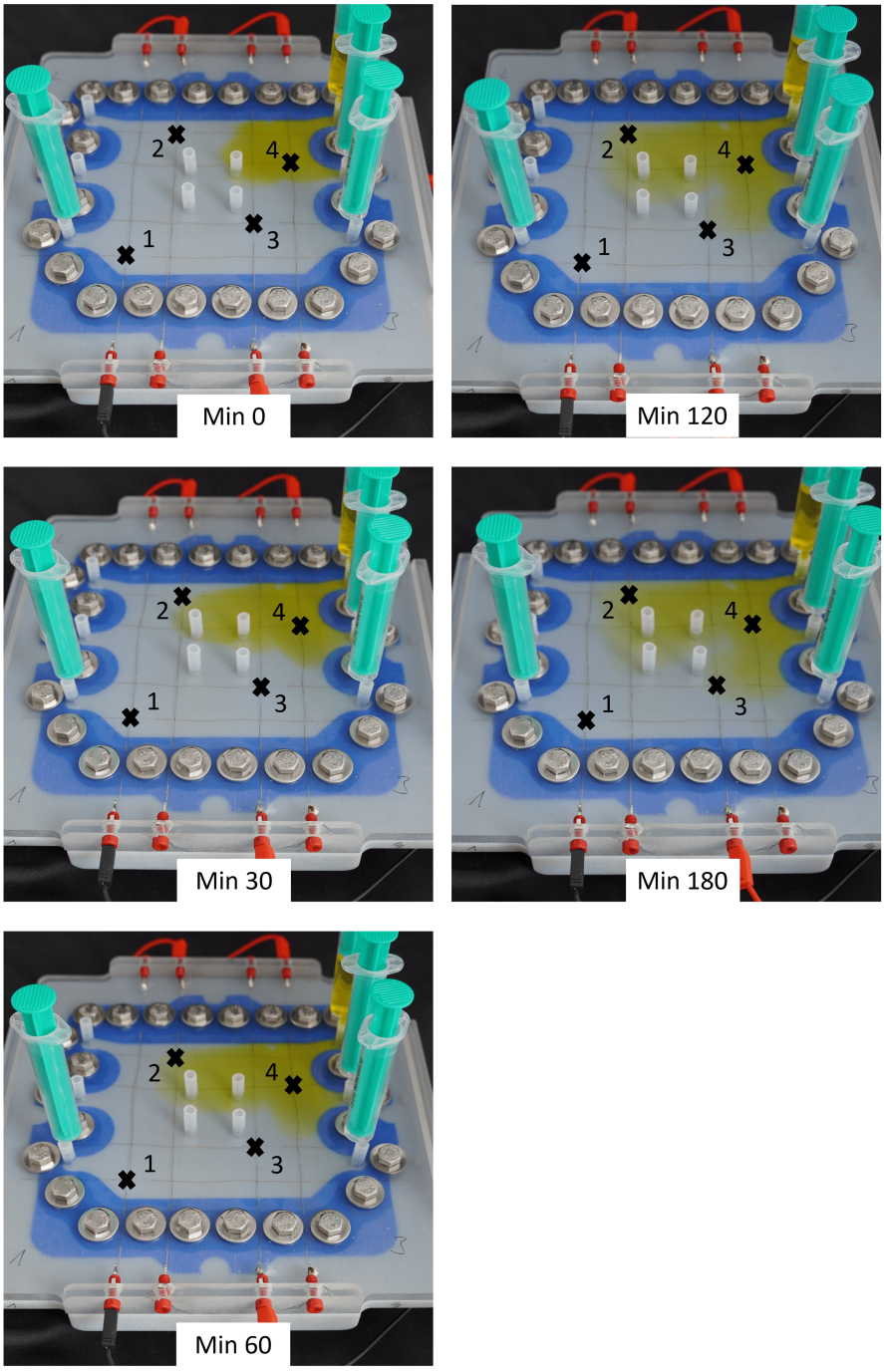

Figure 8.3: Photographs taken during the diffusion experiment show the diffusion between the colored solution and the solution initially placed into the test cell.

Bibliography

[Agra2009] A. Agrawal and K. Sahu. “An overview of the recovery of acid from spent acidic solutions from steel and electroplating industries”. *J. Hazard. Mater.* 171.1 (2009). DOI: 10.1016/j.jhazmat.2009.06.099 (cit. on p. 66).

[Ahme2018] M. A. Ahmed and S. Tewari. “Capacitive deionization: Processes, materials and state of the technology”. *J. Electroanal. Chem.* 813 (2018). DOI: 10.1016/j.jelechem.2018.02.024 (cit. on pp. 16, 23).

[Ahme2021] F. E. Ahmed, A. Khalil, and N. Hilal. “Emerging desalination technologies: Current status, challenges and future trends”. *Desalination* 517 (2021). DOI: 10.1016/j.desal.2021.115183 (cit. on p. 2).

[Akuz2020] B. Akuzum, P. Singh, D. A. Eichfeld, L. Agartan, S. Uzun, Y. Gogotsi, and E. C. Kumbur. “Percolation Characteristics of Conductive Additives for Capacitive Flowable (Semi-Solid) Electrodes”. *ACS Appl. Mater. Interfaces* 12.5 (2020). DOI: 10.1021/acsami.9b19739 (cit. on p. 27).

[Alia2021] M. Aliaskari and A. I. Schäfer. “Nitrate, arsenic and fluoride removal by electrodialysis from brackish groundwater”. *Water Res.* 190 (2021). DOI: 10.1016/j.watres.2020.116683 (cit. on p. 74).

[Ande2004] M. D. Andelman and G. S. Walker. *Charge barrier flow-through capacitor*. US Patent 6,709,560. 2004 (cit. on p. 23).

[Ande2010] M. A. Anderson, A. L. Cudero, and J. Palma. “Capacitive deionization as an electrochemical means of saving energy and delivering clean water. Comparison to present desalination practices: Will it compete?” *Electrochim. Acta* 55.12 (2010). DOI: 10.1016/j.electacta.2010.02.012 (cit. on p. 16).

[Arno1961] B. B. Arnold and G. W. Murphy. “Studies on the electrochemistry of carbon and chemically-modified carbon surfaces”. *J. Phys. Chem.* 65.1 (1961). DOI: 10.1021/j100819a038 (cit. on p. 22).

[Bake2004] R. W. Baker. *Membrane Technology and Applications, second ed.* Chichester, UK: John Wiley & Sons, Ltd, 2004. DOI: 10.1002/0470020393 (cit. on pp. 13, 14).

[Bald2013] M. Balderacchi, P. Benoit, P. Cambier, O. M. Eklo, A. Gargini, A. Gemitzi, M. Gurel, B. Kløve, Z. Nakic, E. Predaa, S. Ruzicic, P. Wachniew, and M. Trevisan. “Groundwater pollution and quality monitoring approaches at the European level”. *Crit. Rev. Environ. Sci. Technol.* 43 (4 2013). DOI: 10.1080/10643389.2011.604259 (cit. on p. 1).

[Bard2000] A. J. Bard, L. R. Faulkner, and H. S. White. *Electrochemical methods: fundamentals and applications*. John Wiley & Sons, 2000 (cit. on p. 20).

[Batt2021] G. Battaglia, L. Gurreri, M. Ciofalo, A. Cipollina, I. D. L. Bogle, A. Pirrotta, and G. Micale. “A 2-D model of electrodialysis stacks including the effects of membrane deformation”. *Desalination* 500 (2021). DOI: 10.1016/j.desal.2020.114835 (cit. on p. 121).

[Bech2018] W. Bechmann and I. Bald. *Einstieg in die physikalische Chemie für Naturwissenschaftler*. Springer, 2018 (cit. on p. 36).

[Bies2009a] P. M. Biesheuvel, B. van Limpt, and A. van der Wal. “Dynamic Adsorption/Desorption Process Model for Capacitive Deionization”. *J. Phys. Chem. C* 113.14 (2009). DOI: 10.1021/jp809644s (cit. on p. 21).

[Bies2009b] P. Biesheuvel. “Thermodynamic cycle analysis for capacitive deionization”. *J. Colloid Interface Sci.* 332.1 (2009). DOI: 10.1016/j.jcis.2008.12.018 (cit. on p. 21).

[Bies2011] P. Biesheuvel, R. Zhao, S. Porada, and A. van der Wal. “Theory of membrane capacitive deionization including the effect of the electrode pore space”. *J. Colloid Interface Sci.* 360.1 (2011). DOI: 10.1016/j.jcis.2011.04.049 (cit. on p. 21).

[Bies2014] P. Biesheuvel, S. Porada, M. Levi, and M. Z. Bazant. “Attractive forces in microporous carbon electrodes for capacitive deionization”. *J. Solid State Chem.* 18 (2014). DOI: 10.1007/s10008-014-2383-5 (cit. on p. 21).

[Blai1960] J. W. Blair and G. W. Murphy. “Electrochemical Demineralization of Water with Porous Electrodes of Large Surface Area”. In *Saline Water Conversion*. 1960. Chap. 20, pp. 206–223. DOI: 10.1021/ba-1960-0027.ch020 (cit. on p. 22).

[Bock2000] J. O. Bockris, A. K. Reddy, and M. Gamboa-Aldeco. “Electrodics”. *Modern Electrochemistry 2A: Fundamentals of Electrodics* (2000). (Cit. on pp. 20, 37).

[Bóda2003] A. Bódalo-Santoyo, J. Gómez-Carrasco, E. Gómez-Gómez, F. Máximo-Martín, and A. Hidalgo-Montesinos. “Application of reverse osmosis to reduce pollutants present in industrial wastewater”. *Desalination* 155.2 (2003). DOI: 10.1016/S0011-9164(03)00287-X (cit. on p. 12).

[Bore2019] A. Boretti and L. Rosa. “Reassessing the projections of the World Water Development Report”. *npj Clean Water* 2.15 (2019). DOI: 10.1038/s41545-019-0039-9 (cit. on p. 1).

[Bost1996] J. Bostjancic and R. Ludlum. “Getting to zero discharge: how to recycle that last bit of really bad wastewater”. In *Proceedings of the International Water Conference*. Vol. 57. Engineers Society of Western Pennsylvania. 1996, pp. 290–295 (cit. on p. 12).

[Cado1985] J. E. Cadotte. “Evolution of Composite Reverse Osmosis Membranes”. In *Materials Science of Synthetic Membranes*. 1985. Chap. 12, pp. 273–294. DOI: 10.1021/bk-1985-0269.ch012 (cit. on p. 12).

[Camp2018] A. Campione, L. Gurreri, M. Ciofalo, G. Micale, A. Tamburini, and A. Cipollina. “Electrodialysis for water desalination: A critical assessment of recent developments on process fundamentals, models and applications”. *Desalination* 434 (2018). DOI: 10.1016/j.desal.2017.12.044 (cit. on p. 15).

[Cañe2013] M. Cañedo-Argüelles, B. J. Kefford, C. Piscart, N. Prat, R. B. Schäfer, and C.-J. Schulz. “Salinisation of rivers: An urgent ecological issue”. *Environ. Pollut.* 173 (2013). DOI: 10.1016/j.envpol.2012.10.011 (cit. on p. 1).

[Celz2000] A. Celzard, J. F. Marêché, G. Furdin, and S. Puricelli. “Electrical conductivity of anisotropic expanded graphite-based monoliths”. *J. Phys. D: Appl. Phys.* 33.23 (Dec. 2000). DOI: 10.1088/0022-3727/33/23/313 (cit. on p. 103).

[Chan2019] J. Chang, F. Duan, H. Cao, K. Tang, C. Su, and Y. Li. “Superiority of a novel flow-electrode capacitive deionization (FCDI) based on a battery material at high applied voltage”. *Desalination* 468 (2019). DOI: 10.1016/j.desal.2019.114080 (cit. on p. 27).

[Chap1913] D. L. Chapman. “LI. A contribution to the theory of electrocapillarity”. *The London, Edinburgh, and Dublin Philosophical Magazine and Journal of Science* 25.148 (1913). DOI: 10.1080/14786440408634187 (cit. on p. 20).

[Chen2022] R. Chen, X. Deng, C. Wang, J. Du, Z. Zhao, W. Shi, J. Liu, and F. Cui. “A newly designed graphite-polyaniline composite current collector to enhance the performance of flow electrode capacitive deionization”. *Chem. Eng. J.* 435 (2022). DOI: 10.1016/j.cej.2022.134845 (cit. on pp. 30, 113).

[Chen2023] B. Chen, Z. Zhang, C. Jiang, R. Fu, J. Yan, H. Wang, R. Li, G. Cao, Y. Wang, and T. Xu. “Electro-membrane reactor: A powerful tool for green chemical engineering”. *AIChE Journal* 69.9 (2023). DOI: 10.1002/aic.18140 (cit. on p. 18).

[Cho2017] Y. Cho, K. S. Lee, S. C. Yang, J. Choi, H. R. Park, and D. K. Kim. “A novel three-dimensional desalination system utilizing honeycomb-shaped lattice structures for flow-electrode capacitive deionization”. *Energy Environ. Sci.* 10 (8 2017). DOI: 10.1039/c7ee00698e (cit. on pp. 29, 44).

[Choo2019] K. Y. Choo, K. S. Lee, M. H. Han, and D. K. Kim. “Study on the electrochemical characteristics of porous ceramic spacers in a capacitive deionization cell using slurry electrodes”. *J. Electroanal. Chem.* 835 (2019). DOI: 10.1016/j.jelechem.2019.01.009 (cit. on p. 44).

[Chun2020] H. J. Chung, J. Kim, D. I. Kim, G. Gwak, and S. Hong. “Feasibility study of reverse osmosis–flow capacitive deionization (RO-FCDI) for energy-efficient desalination using seawater as the flow-electrode aqueous electrolyte”. *Desalination* 479 (2020). DOI: 10.1016/j.desal.2020.114326 (cit. on p. 31).

[Dams2009] M. Damsohn and H.-M. Prasser. “High-speed liquid film sensor with high spatial resolution”. *Meas. Sci. Technol.* 20.11 (2009). DOI: 10.1088/0957-0233/20/11/114001 (cit. on p. 40).

[Dave2018] D. M. Davenport, A. Deshmukh, J. R. Werber, and M. Elimelech. “High-Pressure Reverse Osmosis for Energy-Efficient Hypersaline Brine Desalination: Current Status, Design Considerations, and Research Needs”. *Environ. Sci. Technol. Lett.* 5.8 (2018). DOI: 10.1021/acs.estlett.8b00274 (cit. on p. 13).

[Denn2014] C. R. Dennison, M. Beidaghi, K. B. Hatzell, J. W. Campos, and Y. Gogotsi. “Effects of flow cell design on charge percolation and storage in the carbon slurry electrodes of electrochemical flow capacitors”. *J. Power Sources* 247 (2014). DOI: 10.1016/j.jpowsour.2013.08.101 (cit. on pp. 29, 39).

[Dhak2008] S. Dhakate, S. Sharma, M. Borah, R. Mathur, and T. Dhami. “Expanded graphite-based electrically conductive composites as bipolar plate for PEM fuel cell”. *Int. J. Hydrogen Energy* 33.23 (2008). DOI: 10.1016/j.ijhydene.2008.09.004 (cit. on p. 96).

[Dixi2019] M. B. Dixit, D. Moreno, X. Xiao, M. C. Hatzell, and K. B. Hatzell. “Mapping Charge Percolation in Flowable Electrodes Used in Capacitive Deionization”. *ACS Mater. Lett.* 1.1 (2019). DOI: 10.1021/acsmaterialslett.9b00106 (cit. on p. 27).

[Dong2021] Y. Dong, W. Xing, K. Luo, J. Zhang, J. Yu, W. Jin, J. Wang, and W. Tang. “Effective and continuous removal of Cr(VI) from brackish wastewater by flow-electrode capacitive deionization (FCDI)”. *J. Clean. Prod.* 326 (2021). DOI: 10.1016/j.jclepro.2021.129417 (cit. on p. 32).

[Donn1911] F. G. Donnan. “The theory of membrane equilibrium in the presence of a non-dialyzable electrolyte”. *Z. Electrochem.* 17 (1911). (Cit. on p. 18).

[Door2020] G. Doornbusch, H. Swart, M. Tedesco, J. Post, Z. Borneman, and K. Nijmeijer. “Current utilization in electrodialysis: Electrode segmentation as alternative for multistaging”. *Desalination* 480 (2020). DOI: 10.1016/j.desal.2019.114243 (cit. on p. 121).

[Driv1999] J. Driver, D. Lijmbach, and I. Steen. “Why Recover Phosphorus for Recycling, and How?” *Environ. Technol.* 20.7 (1999). DOI: 10.1080/09593332008616861 (cit. on p. 2).

[Elim2011] M. Elimelech and W. A. Phillip. “The Future of Seawater Desalination: Energy, Technology, and the Environment”. *Science* 333.6043 (2011). DOI: 10.1126/science.1200488 (cit. on p. 10).

[Elsa2020] K. Elsaid, M. Kamil, E. T. Sayed, M. A. Abdelkareem, T. Wilberforce, and A. Olabi. “Environmental impact of desalination technologies: A review”. *Sci. Total Environ.* 748 (2020). DOI: 10.1016/j.scitotenv.2020.141528 (cit. on pp. 2, 11).

[Fang2018] K. Fang, H. Gong, W. He, F. Peng, C. He, and K. Wang. “Recovering ammonia from municipal wastewater by flow-electrode capacitive deionization”. *Chem. Eng. J.* 348 (2018). DOI: 10.1016/j.cej.2018.04.128 (cit. on p. 32).

[Farm2018] A. Farmer. “Phosphate pollution: A global overview of the problem”. In *Phosphorus: Polluter and Resource of the Future – Removal and Recovery from Wastewater*. IWA Publishing, June 2018. (Cit. on p. 2).

[Fili2023] A. Filingeri, L. Gurreri, M. Ciofalo, A. Cipollina, A. Tamburini, and G. Micale. “Current distribution along electrodialysis stacks and its influence on the current-voltage curve: behaviour from near-zero current to limiting plateau”. *Desalination* 556 (2023). DOI: 10.1016/j.desal.2023.116541 (cit. on p. 121).

[Fola2022] G. Folaranmi, M. Tauk, M. Bechelany, P. Sistat, M. Cretin, and F. Zaviska. “Investigation of fine activated carbon as a viable flow electrode in capacitive deionization”. *Desalination* 525 (2022). DOI: 10.1016/j.desal.2021.115500 (cit. on p. 27).

[Fost2019] S. Foster and E. Custodio. “Groundwater Resources and Intensive Agriculture in Europe – Can Regulatory Agencies Cope with the Threat to Sustainability?” *Water Resour. Manag.* 33 (6 Apr. 2019). DOI: 10.1007/s11269-019-02235-6 (cit. on p. 2).

[Fran1996] C. Frank, C. Sink, L. Mynatt, R. Rogers, and A. Rappazzo. “Surviving the “valley of death”: A comparative analysis”. *J. Technol. Transf.* 21 (1996). DOI: 10.1007/BF02220308 (cit. on p. 3).

[Frei2024] N. H. Freire, C. J. Linnartz, L. A. Montoro, V. S. Ciminelli, and M. Wessling. “Flow electrode capacitive deionization with iron-based redox electrolyte”. *Desalination* 578 (2024). DOI: https://doi.org/10.1016/j.desal.2024.117313 (cit. on p. 27).

[Fril1956] V. J. Frilette. “Preparation and characterization of bipolar ion exchange membranes”. *J. Phys. Chem.* 60.4 (1956). DOI: 10.1021/j150538a013 (cit. on p. 18).

[Frit2007] C. Fritzmann, J. Löwenberg, T. Wintgens, and T. Melin. “State-of-the-art of reverse osmosis desalination”. *Desalination* 216.1 (2007). DOI: 10.1016/j.desal.2006.12.009 (cit. on p. 13).

[Gala2016] A. Galama, N. Hoog, and D. Yntema. “Method for determining ion exchange membrane resistance for electrodialysis systems”. *Desalination* 380 (2016). DOI: 10.1016/j.desal.2015.11.018 (cit. on p. 121).

[Geis2014] G. M. Geise, A. J. Curtis, M. C. Hatzell, M. A. Hickner, and B. E. Logan. “Salt Concentration Differences Alter Membrane Resistance in Reverse Electrodialysis Stacks”. *Environ. Sci. Technol. Lett.* 1.1 (2014). DOI: 10.1021/ez4000719 (cit. on p. 121).

[Gend2014] Y. Gendel, A. Rommerskirchen, O. David, and M. Wessling. “Batch mode and continuous desalination of water using flowing carbon deionization (FCDI) technology”. *Electrochem. Commun.* 46 (2014). DOI: 10.1016/j.elecom.2014.06.004 (cit. on pp. 3, 25, 27).

[Gene2021] M. M. Generous, N. A. Qasem, U. A. Akbar, and S. M. Zubair. “Techno-economic assessment of electrodialysis and reverse osmosis desalination plants”. *Sep. Purif. Technol.* 272 (2021). DOI: 10.1016/j.seppur.2021.118875 (cit. on pp. 14, 15).

[Gouy1910] Gouy, M. “Sur la constitution de la charge électrique à la surface d’un électrolyte”. *J. Phys. Theor. Appl.* 9.1 (1910). DOI: 10.1051/jphystap:019100090045700 (cit. on p. 20).

[Grai1996] S. Graillon, F. Persin, G. Pourcelly, and C. Gavach. “Development of electrodialysis with bipolar membranes for the treatment of concentrated nitrate effluents”. *Desalination* 107.2 (1996). DOI: 10.1016/S0011-9164(96)00155-5 (cit. on p. 2).

[Gree2009] L. F. Greenlee, D. F. Lawler, B. D. Freeman, B. Marrot, and P. Moulin. “Reverse osmosis desalination: Water sources, technology, and today’s challenges”. *Water Res.* 43.9 (2009). DOI: 10.1016/j.watres.2009.03.010 (cit. on p. 12).

[Grze2020] M. Grzegorzek, K. Majewska-Nowak, and A. E. Ahmed. “Removal of fluoride from multicomponent water solutions with the use of monovalent selective ion-exchange membranes”. *Sci. Total Environ.* 722 (2020). DOI: 10.1016/j.scitotenv.2020.137681 (cit. on p. 74).

[Ha2019] Y. Ha, H. B. Jung, H. Lim, P. S. Jo, H. Yoon, C. Y. Yoo, T. K. Pham, W. Ahn, and Y. Cho. “Continuous lithium extraction from aqueous solution using flow-electrode capacitive deionization”. *Energies* 12 (15 2019). DOI: 10.3390/en12152913 (cit. on p. 32).

[Hatz2015] K. B. Hatzell, M. C. Hatzell, K. M. Cook, M. Boota, G. M. Housel, A. McBride, E. C. Kumbur, and Y. Gogotsi. “Effect of Oxidation of Carbon Material on Suspension Electrodes for Flow Electrode Capacitive Deionization”. *Environ. Sci. Technol.* 49.5 (2015). DOI: 10.1021/es5055989 (cit. on p. 27).

[Hatz2017] K. B. Hatzell, J. Eller, S. L. Morelly, M. H. Tang, J. Alvarez, and Y. Gogotsi. “Direct observation of active material interactions in flowable electrodes using X-ray tomography”. *Faraday Discuss.* (2017). DOI: 10.1039/c6fd00243a (cit. on pp. 26, 27).

[Hawk2019] S. A. Hawks, A. Ramachandran, S. Porada, P. G. Campbell, M. E. Suss, P. Biesheuvel, J. G. Santiago, and M. Stadermann. “Performance metrics for the objective assessment of capacitive deionization systems”. *Water Res.* 152 (2019). DOI: 10.1016/j.watres.2018.10.074 (cit. on p. 32).

[He2018] C. He, J. Ma, C. Zhang, J. Song, and T. D. Waite. “Short-Circuited Closed-Cycle Operation of Flow-Electrode CDI for Brackish Water Softening”. *Environ. Sci. Technol.* 52.16 (2018). DOI: 10.1021/acs.est.8b02807 (cit. on p. 32).

[He2021] C. He, B. Lian, J. Ma, C. Zhang, Y. Wang, H. Mo, and T. D. Waite. “Scale-up and Modelling of Flow-electrode CDI Using Tubular Electrodes”. *Water Res.* 203 (Sept. 2021). DOI: 10.1016/j.watres.2021.117498 (cit. on pp. 29, 44).

[Heid2021] A. Heidarian, S. C. Cheung, and G. Rosengarten. “The effect of flow rate and concentration on the electrical conductivity of slurry electrodes using a coupled computational fluid dynamic and discrete element method (CFD–DEM) model”. *Electrochem. Commun.* 126 (2021). DOI: 10.1016/j.elecom.2021.107017 (cit. on pp. 27, 28).

[Helm1853] H. v. Helmholtz. “Ueber einige Gesetze der Vertheilung elektrischer Ströme in körperlichen Leitern, mit Anwendung auf die thierisch-elektrischen Versuche (Schluss.)” *Ann. Phys.* 165.7 (1853). (Cit. on p. 20).

[Hemm2015] A. Hemmatifar, M. Stadermann, and J. G. Santiago. “Two-Dimensional Porous Electrode Model for Capacitive Deionization”. *J. Phys. Chem. C* 119.44 (2015). DOI: 10.1021/acs.jpcc.5b05847 (cit. on p. 22).

[Höhn2006] T. Höhne, S. Kliem, and U. Bieder. “Modeling of a buoyancy-driven flow experiment at the ROCOM test facility using the CFD codes CFX-5 and Trio_U”. *Nucl. Eng. Des.* 236.12 (2006). DOI: 10.1016/j.nucengdes.2005.12.005 (cit. on pp. 41, 121).

[Hoyt2018] N. C. Hoyt, E. Agar, E. A. Nagelli, R. Savinell, and J. Wainright. “Editors’ Choice—Electrochemical Impedance Spectroscopy of Flowing Electrosorptive Slurry Electrodes”. *J. Electrochem. Soc.* 165.10 (2018). DOI: 10.1149/2.0051810jes (cit. on p. 39).

[Huka2016] S. Hukari, L. Hermann, and A. Nättorp. “From wastewater to fertilisers — Technical overview and critical review of European legislation governing phosphorus recycling”. *Sci. Total Environ.* 542 (2016). DOI: 10.1016/j.scitotenv.2015.09.064 (cit. on p. 2).

[Hwan2021] I. Hwang, D. Lee, Y. Jung, K. Park, Y.-G. Jung, D. Kim, G.-H. Cho, S.-i. Jeon, Y.-k. Byeun, U. Paik, S. Yang, and T. Song. “Cross Effect of Surface Area and Electrical Conductivity for Carbonaceous Materials in Flow-electrode Capacitive Mixing (F-CapMix) and Flow-electrode Capacitive Deionization (FCDI): Solid-like Behavior of Flow-electrode”. *ACS Sustain. Chem. Eng.* 9.40 (2021). DOI: 10.1021/acssuschemeng.1c04419 (cit. on p. 27).

[Impe1983] R. Impey, P. Madden, and I. McDonald. “Hydration and mobility of ions in solution”. *J. Phys. Chem.* 87.25 (1983). DOI: 10.1021/j150643a008 (cit. on p. 30).

[Ito2011] D. Ito, H. Kikura, and M. Aritomi. “Micro wire-mesh sensor for two-phase flow measurement in a rectangular narrow channel”. *Flow Meas. Instrum.* 22.5 (2011). DOI: 10.1016/j.flowmeasinst.2011.06.001 (cit. on pp. 40, 121).

[Ito2012] H. Ito, T. Maeda, A. Nakano, C. M. Hwang, M. Ishida, A. Kato, and T. Yoshida. “Experimental study on porous current collectors of PEM electrolyzers”. *Int. J. Hydrogen Energy* 37.9 (2012). DOI: 10.1016/j.ijhydene.2012.01.095 (cit. on p. 28).

[Jeon2013] S.-i. Jeon, H.-r. Park, J.-g. Yeo, S. Yang, C. H. Cho, M. H. Han, and D. K. Kim. “Desalination via a new membrane capacitive deionization process utilizing flow-electrodes”. *Energy Environ. Sci.* 6.5 (2013). DOI: 10.1039/c3ee24443a (cit. on pp. 3, 24, 25, 27).

[Jian2014] C. Jiang, Y. Wang, Z. Zhang, and T. Xu. “Electrodialysis of concentrated brine from RO plant to produce coarse salt and freshwater”. *J. Membr. Sci.* 450 (2014). DOI: 10.1016/j.memsci.2013.09.020 (cit. on pp. 16, 110).

[Jian2021] S. Jiang, H. Sun, H. Wang, B. P. Ladewig, and Z. Yao. “A comprehensive review on the synthesis and applications of ion exchange membranes”. *Chemosphere* 282 (2021). DOI: 10.1016/j.chemosphere.2021.130817 (cit. on p. 19).

[Jian2022] H. Jiang, J. Zhang, K. Luo, W. Xing, J. Du, Y. Dong, X. Li, and W. Tang. “Effective fluoride removal from brackish groundwaters by flow-electrode capacitive deionization (FCDI) under a continuous-flow mode”. *Sci. Total Environ.* 804 (2022). DOI: 10.1016/j.scitotenv.2021.150166 (cit. on p. 32).

[John1987] I. D. Johnson. “Method and apparatus for measuring water in crude oil”. Pat. US4644263A. 1987 (cit. on p. 40).

[Jone2019] E. Jones, M. Qadir, M. T. van Vliet, V. Smakhtin, and S.-m. Kang. “The state of desalination and brine production: A global outlook”. *Sci. Total Environ.* 657 (2019). DOI: 10.1016/j.scitotenv.2018.12.076 (cit. on pp. 1, 12).

[Juda1950] W. Juda and W. A. McRae. “Coherent ion-exchange gels and membranes”. *J. Am. Chem. Soc.* 72.2 (1950). DOI: 10.1021/ja01158a528 (cit. on p. 18).

[Kast1988] B. Kastening. “Properties of Slurry Electrodes from Activated Carbon Powder”. *Ber. Bunsenges. Phys. Chem.* 92.11 (1988). DOI: 10.1002/bbpc.198800334 (cit. on p. 26).

[Kast1997] B. Kastening, T. Boinowitz, and M. Heins. “Design of a slurry electrode reactor system”. *J. Appl. Electrochem.* 27.2 (1997). DOI: 10.1023/A:1018443705541 (cit. on p. 26).

[Kaus2016] S. S. Kaushal. “Increased Salinization Decreases Safe Drinking Water”. *Environ. Sci. Technol.* 50.6 (2016). DOI: 10.1021/acs.est.6b00679 (cit. on p. 1).

[Khaw2008] A. D. Khawaji, I. K. Kutubkhanah, and J.-M. Wie. “Advances in seawater desalination technologies”. *Desalination* 221.1-3 (2008). DOI: 10.1016/j.desal.2007.01.067 (cit. on p. 11).

[Kim2017] B. Kim, S. Choi, V. S. Pham, R. Kwak, and J. Han. “Energy efficiency enhancement of electromembrane desalination systems by local flow redistribution optimized for the asymmetry of cation/anion diffusivity”. *J. Membr. Sci.* 524 (2017). DOI: 10.1016/j.memsci.2016.11.046 (cit. on p. 15).

[Kim2019] J. Kim, K. Park, D. R. Yang, and S. Hong. “A comprehensive review of energy consumption of seawater reverse osmosis desalination plants”. *Appl. Energy* 254 (2019). DOI: 10.1016/j.apenergy.2019.113652 (cit. on p. 12).

[Kim2021] H. Kim, S. Yang, J. Choi, J.-O. Kim, and N. Jeong. “Optimization of the number of cell pairs to design efficient reverse electrodialysis stack”. *Desalination* 497 (2021). DOI: 10.1016/j.desal.2020.114676 (cit. on p. 62).

[Kim2023] N. Kim, J. Park, Y. Cho, and C.-Y. Yoo. “Comprehensive Electrochemical Impedance Spectroscopy Study of Flow-Electrode Capacitive Deionization Cells”. *Environ. Sci. Technol.* 57.23 (2023). DOI: 10.1021/acs.est.3c01619 (cit. on p. 39).

[Klie2008a] S. Kliem, H.-M. Prasser, T. Sühnel, F.-P. Weiss, and A. Hansen. “Experimental determination of the boron concentration distribution in the primary circuit of a PWR after a postulated cold leg small break loss-of-coolant-accident with cold leg safety injection”. *Nucl. Eng. Des.* 238.7 (2008). DOI: 10.1016/j.nucengdes.2007.10.016 (cit. on p. 40).

[Klie2008b] S. Kliem, T. Sühnel, U. Rohde, T. Höhne, H.-M. Prasser, and F.-P. Weiss. “Experiments at the mixing test facility ROCOM for benchmarking of CFD codes”. *Nucl. Eng. Des.* 238.3 (2008). DOI: 10.1016/j.nucengdes.2007.02.053 (cit. on pp. 41, 121).

[Kona2020] G. Konapala, A. K. Mishra, Y. Wada, and M. E. Mann. “Climate change will affect global water availability through compounding changes in seasonal precipitation and evaporation”. *Nature Commun.* 11.1 (2020). DOI: 10.1038/s41467-020-16757-w (cit. on p. 1).

[Krau2007] S. Krause. “Impedance Methods”. In *Encyclopedia of Electrochemistry*. John Wiley & Sons, Ltd, 2007. DOI: 10.1002/9783527610426.bard030206 (cit. on p. 39).

[Kuma2013] S. Kumar and S. Jain. “History, introduction, and kinetics of ion exchange materials”. *J. Chem.* 2013 (2013). DOI: 10.1155/2013/957647 (cit. on p. 17).

[La C2018] M. La Cerva, L. Gurreri, M. Tedesco, A. Cipollina, M. Ciofalo, A. Tamburini, and G. Micale. “Determination of limiting current density and current efficiency in electrodialysis units”. *Desalination* 445 (2018). DOI: 10.1016/j.desal.2018.07.028 (cit. on p. 15).

[Lee2006] J.-B. Lee, K.-K. Park, H.-M. Eum, and C.-W. Lee. “Desalination of a thermal power plant wastewater by membrane capacitive deionization”. *Desalination* 196.1 (2006). DOI: 10.1016/j.desal.2006.01.011 (cit. on p. 23).

[Li2003] L.-F. Li and J.-P. Celis. “Pickling of Austenitic Stainless Steels (a Review)”. *Can. Metall. Q.* 42.3 (2003). DOI: 10.1179/cmq.2003.42.3.365 (cit. on p. 66).

[Li2005] L.-F. Li, P. Caenen, M. Daerden, D. Vaes, G. Meers, C. Dhondt, and J.-P. Celis. “Mechanism of single and multiple step pickling of 304 stainless steel in acid electrolytes”. *Corros. Sci.* 47.5 (2005). DOI: 10.1016/j.corsci.2004.06.025 (cit. on p. 66).

[Li2008] H. Li, Y. Gao, L. Pan, Y. Zhang, Y. Chen, and Z. Sun. “Electrosorptive desalination by carbon nanotubes and nanofibres electrodes and ion-exchange membranes”. *Water Res.* 42.20 (2008). DOI: 10.1016/j.watres.2008.09.026 (cit. on p. 23).

[Li2019] X. Li, Y. Mo, W. Qing, S. Shao, C. Y. Tang, and J. Li. “Membrane-based technologies for lithium recovery from water lithium resources: A review”. *J. Membr. Sci.* 591 (2019). DOI: 10.1016/j.memsci.2019.117317 (cit. on p. 2).

[Li2024] Y. Li, J. Ma, M. Yu, J. Niu, J. Gu, M. Chen, P. Zhang, J. Zhang, and C. Liu. “Carbon felt (CF) acted as an “ionic capacitor” to enhance flow electrode capacitive deionization (FCDI) desalination performance”. *Desalination* 575 (2024). DOI: https://doi.org/10.1016/j.desal.2024.117341 (cit. on p. 30).

[Lian2017] P. Liang, X. Sun, Y. Bian, H. Zhang, X. Yang, Y. Jiang, P. Liu, and X. Huang. “Optimized desalination performance of high voltage flow-electrode capacitive deionization by adding carbon black in flow-electrode”. *Desalination* 420 (2017). DOI: 10.1016/j.desal.2017.05.023 (cit. on p. 56).

[Link2001] V. Linkov and V. Belyakov. “Novel ceramic membranes for electrodialysis”. *Sep. Purif. Technol.* 25.1 (2001). DOI: 10.1016/S1383-5866(01)00090-9 (cit. on p. 18).

[Linn2020] C. J. Linnartz, A. Rommerskirchen, J. Walker, J. Plankermann-Hajduk, N. Köller, and M. Wessling. “Membrane-electrode assemblies for flow-electrode capacitive deionization”. *J. Membr. Sci.* 605 (2020). DOI: 10.1016/j.memsci.2020.118095 (cit. on pp. 30, 50, 55, 96, 98, 99, 107).

[Linn2022] C. Linnartz. “From fundamentals of transport in flow electrodes at membrane interfaces to application”. published Shaker Verlag, ISBN 978-3-8440-8666-9. PhD thesis. RWTH Aachen University, 2022 (cit. on pp. 44, 45, 55, 61, 62, 73, 121).

[Liu2019] C. Liu, J. Lin, H. Cao, Y. Zhang, and Z. Sun. “Recycling of spent lithium-ion batteries in view of lithium recovery: A critical review”. *J. Clean. Prod.* 228 (2019). DOI: 10.1016/j.jclepro.2019.04.304 (cit. on p. 2).

[Loeb1962] S. Loeb and S. Sourirajan. “Sea water demineralization by means of an osmotic membrane”. In. ACS Publications, 1962. (Cit. on p. 12).

[Loha2019] J. Lohaus, D. Rall, M. Kruse, V. Steinberger, and M. Wessling. “On charge percolation in slurry electrodes used in vanadium redox flow batteries”. *Electrochem. Commun.* 101 (2019). DOI: 10.1016/j.elecom.2019.02.013 (cit. on p. 27).

[Luo2018] T. Luo, S. Abdu, and M. Wessling. “Selectivity of ion exchange membranes: A review”. *J. Membr. Sci.* 555 (2018). DOI: 10.1016/j.memsci.2018.03.051 (cit. on pp. 2, 14, 19, 30, 74).

[Ma2016] J. Ma, D. He, W. Tang, P. Kovalsky, C. He, C. Zhang, and T. D. Waite. “Development of Redox-Active Flow Electrodes for High-Performance Capacitive Deionization”. *Environ. Sci. Technol.* 50.24 (2016). DOI: 10.1021/acs.est.6b03424 (cit. on p. 27).

[Ma2019] J. Ma, Y. Zhang, R. N. Collins, S. Tsarev, N. Aoyagi, A. S. Kinsela, A. M. Jones, and T. D. Waite. “Flow-Electrode CDI Removes the Uncharged Ca–UO2–CO3 Ternary Complex from Brackish Potable Groundwater: Complex Dissociation, Transport, and Sorption”. *Environ. Sci. Technol.* 53.5 (2019). DOI: 10.1021/acs.est.8b07157 (cit. on p. 32).

[Ma2020a] J. Ma, J. Ma, C. Zhang, J. Song, W. Dong, and T. D. Waite. “Flow-electrode capacitive deionization (FCDI) scale-up using a membrane stack configuration”. *Water Res.* 168 (2020). DOI: 10.1016/j.watres.2019.115186 (cit. on pp. 44, 45).

[Ma2020b] J. Ma, C. Zhang, F. Yang, X. Zhang, M. E. Suss, X. Huang, and P. Liang. “Carbon Black Flow Electrode Enhanced Electrochemical Desalination Using Single-Cycle Operation”. *Environ. Sci. Technol.* 54.2 (2020). DOI: 10.1021/acs.est.9b04823 (cit. on pp. 27, 63).

[Mane2003] A. Manera. “Experimental and analytical investigations on flashing-induced instabilities in natural circulation two-phase systems: Applications to the startup of boiling water reactors.” PhD thesis. Technische Universiteit Delft (The Netherlands), 2003 (cit. on p. 41).

[Mank2009] J. C. Mankins. “Technol. readiness assessments: A retrospective”. *Acta Astronaut.* 65.9 (2009). DOI: 10.1016/j.actaastro.2009.03.058 (cit. on p. 44).

[McGo2014] R. K. McGovern, S. M. Zubair, and J. H. Lienhard V. “The benefits of hybridising electrodialysis with reverse osmosis”. *J. Membr. Sci.* 469 (2014). DOI: 10.1016/j.memsci.2014.06.040 (cit. on p. 16).

[Meko2016] M. M. Mekonnen and A. Y. Hoekstra. “Four billion people facing severe water scarcity”. *Sci. Adv.* 2.2 (2016). DOI: 10.1126/sciadv.1500323 (cit. on p. 1).

[Meli2007] T. Melin and R. Rautenbach. *Membranverfahren: Grundlagen der Modul- und Anlagenauslegung*. 3., aktualisierte und erweiterte Auflage. VDI-Buch. Berlin, Heidelberg: Springer-Verlag Berlin Heidelberg, 2007. DOI: 10.1007/978-3-540-34328-8 (cit. on pp. 13, 14).

[Meye1940] K. H. Meyer and W. Straus. “La perméabilité des membranes VI. Sur le passage du courant electrique a travers des membranes sélectives”. *Helv. Chim. Acta* 23.1 (1940). (Cit. on p. 18).

[Mila2020] G. Milano, A. Cultrera, K. Bejtka, N. De Leo, L. Callegaro, C. Ricciardi, and L. Boarino. “Mapping Time-Dependent Conductivity of Metallic Nanowire Networks by Electrical Resistance Tomography toward Transparent Conductive Materials”. *ACS Appl. Nano Mater.* 3.12 (2020). DOI: 10.1021/acsanm.0c02204 (cit. on p. 121).

[Mill1974] F. J. Millero. “The physical chemistry of seawater”. *Annu. Rev. Earth Planet. Sci.* 2.1 (1974). DOI: 10.1146/annurev.ea.02.050174.000533 (cit. on p. 10).

[More2018] D. Moreno and M. C. Hatzell. “Influence of Feed-Electrode Concentration Differences in Flow-Electrode Systems for Capacitive Deionization”. *Ind. Eng. Chem. Res.* 57.26 (2018). DOI: 10.1021/acs.iecr.8b01626 (cit. on p. 28).

[Moss2013] M. Mossad, W. Zhang, and L. Zou. “Using capacitive deionisation for inland brackish groundwater desalination in a remote location”. *Desalination* 308 (2013). DOI: 10.1016/j.desal.2012.05.021 (cit. on p. 22).

[Murp1967] G. Murphy and D. Caudle. “Mathematical theory of electrochemical demineralization in flowing systems”. *Electrochim. Acta* 12.12 (1967). DOI: 10.1016/0013-4686(67)80079-3 (cit. on p. 22).

[Naga1977] K. Nagasubramanian, F. Chlanda, and K.-J. Liu. “Use of bipolar membranes for generation of acid and base — an engineering and economic analysis”. *J. Membr. Sci.* 2 (1977). DOI: 10.1016/S0376-7388(00)83237-8 (cit. on p. 18).

[Negr2001] C. Negro, M. A. Blanco, F. López-Mateos, A. M. C. P. DeJong, G. LaCalle, J. V. Erkel, and D. Schmal. “Free Acids and Chemicals Recovery from Stainless Steel Pickling Baths”. *Sep. Sci. Technol.* 36.7 (2001). DOI: 10.1081/SS-100103887 (cit. on pp. 66, 67).

[Oren2008] Y. Oren. “Capacitive deionization (CDI) for desalination and water treatment — past, present and future (a review)”. *Desalination* 228.1-3 (2008). DOI: 10.1016/j.desal.2007.08.005 (cit. on pp. 16, 23).

[Ostw1890] W. Ostwald. “Elektrische Eigenschaften halbdurchlässiger Scheidewände”. *Z. Phys. Chem.* 6U.1 (1890). DOI: 10.1515/zpch-1890-0609 (cit. on p. 18).

[Padl2024] M. C. Padligur, C. J. Linnartz, S. Zimmer, J. Linkhorst, and M. Wessling. “Coupled optical-electric monitoring of charge percolation events in carbon flow-electrodes”. *Chem. Eng. J.* (2024). DOI: 10.1016/j.cej.2024.148749 (cit. on p. 27).

[Pärn2021] R. Pärnamäe, S. Mareev, V. Nikonenko, S. Melnikov, N. Sheldeshov, V. Zabolotskii, H. Hamelers, and M. Tedesco. “Bipolar membranes: A review on principles, latest developments, and applications”. *J. Membr. Sci.* 617 (2021). DOI: https://doi.org/10.1016/j.memsci.2020.118538 (cit. on p. 19).

[Pate2020] S. K. Patel, M. Qin, W. S. Walker, and M. Elimelech. “Energy Efficiency of Electro-Driven Brackish Water Desalination: Electrodialysis Significantly Outperforms Membrane Capacitive Deionization”. *Environ. Sci. Technol.* 54.6 (2020). DOI: 10.1021/acs.est.9b07482 (cit. on p. 45).

[Pate2021] S. K. Patel, P. M. Biesheuvel, and M. Elimelech. “Energy Consumption of Brackish Water Desalination: Identifying the Sweet Spots for Electrodialysis and Reverse Osmosis”. *ACS EST Engg.* 1.5 (2021). DOI: 10.1021/acsestengg.0c00192 (cit. on p. 15).

[Pete2015] T. J. Petek, N. C. Hoyt, R. F. Savinell, and J. S. Wainright. “Characterizing Slurry Electrodes Using Electrochemical Impedance Spectroscopy”. *J. Electrochem. Soc.* 163.1 (2015). DOI: 10.1149/2.0011601jes (cit. on p. 39).

[Pora2012] S. Porada, B. B. Sales, H. V. M. Hamelers, and P. M. Biesheuvel. “Water Desalination with Wires”. *J. Phys. Chem. Lett.* 3.12 (2012). DOI: 10.1021/jz3005514 (cit. on p. 24).

[Pora2013] S. Porada, R. Zhao, A. van der Wal, V. Presser, and P. M. Biesheuvel. “Review on the science and technology of water desalination by capacitive deionization”. *Prog. Mater. Sci.* 58.8 (2013). DOI: 10.1016/j.pmatsci.2013.03.005 (cit. on pp. 16, 20, 23).

[Pora2014] S. Porada, D. Weingarth, H. V. Hamelers, M. Bryjak, V. Presser, and P. M. Biesheuvel. “Carbon flow electrodes for continuous operation of capacitive deionization and capacitive mixing energy generation”. *J. Mater. Chem. A* 2.24 (2014). DOI: 10.1039/C4TA01783H (cit. on pp. 23, 27).

[Pora2018] S. Porada, W. van Egmond, J. Post, M. Saakes, and H. Hamelers. “Tailoring ion exchange membranes to enable low osmotic water transport and energy efficient electrodialysis”. *J. Membr. Sci.* 552 (2018). DOI: 10.1016/j.memsci.2018.01.050 (cit. on pp. 31, 75).

[Pres2012] V. Presser, C. R. Dennison, J. Campos, K. W. Knehr, E. C. Kumbur, and Y. Gogotsi. “The Electrochemical Flow Capacitor: A New Concept for Rapid Energy Storage and Recovery”. *Adv. Energy Mater.* 2.7 (2012). DOI: 10.1002/aenm.201100768 (cit. on p. 26).

[Raut2000] R. Rautenbach, T. Linn, and L. Eilers. “Treatment of severely contaminated waste water by a combination of RO, high-pressure RO and NF — potential and limits of the process”. *J. Membr. Sci.* 174.2 (2000). DOI: 10.1016/S0376-7388(00)00388-4 (cit. on p. 13).

[Rodr2011] I. H. Rodriguez, H. K. Yamaguti, M. S. de Castro, M. J. Da Silva, and O. M. Rodriguez. “Slip ratio in dispersed viscous oil–water pipe flow”. *Exp. Therm. Fluid Sci.* 35.1 (2011). DOI: 10.1016/j.expthermflusci.2010.07.017 (cit. on p. 41).

[Romm2015] A. Rommerskirchen, Y. Gendel, and M. Wessling. “Single module flow-electrode capacitive deionization for continuous water desalination”. *Electrochem. Commun.* 60 (2015). DOI: 10.1016/j.elecom.2015.07.018 (cit. on pp. 25, 50, 68, 99, 106).

[Romm2018] A. Rommerskirchen, B. Ohs, K. A. Hepp, R. Femmer, and M. Wessling. “Modeling continuous flow-electrode capacitive deionization processes with ion-exchange membranes”. *J. Membr. Sci.* 546 (2018). DOI: 10.1016/j.memsci.2017.10.026 (cit. on pp. 22, 121).

[Romm2019] A. Rommerskirchen, A. Kalde, C. J. Linnartz, L. Bongers, G. Linz, and M. Wessling. “Unraveling charge transport in carbon flow-electrodes: Performance prediction for desalination applications”. *Carbon* 145 (2019). DOI: 10.1016/j.carbon.2019.01.053 (cit. on pp. 27, 39).

[Romm2020a] A. Rommerskirchen, M. Alders, F. Wiesner, C. J. Linnartz, A. Kalde, and M. Wessling. “Process model for high salinity flow-electrode capacitive deionization processes with ion-exchange membranes”. *J. Membr. Sci.* 616 (2020). DOI: 10.1016/j.memsci.2020.118614 (cit. on pp. 22, 121).

[Romm2020b] A. Rommerskirchen, C. J. Linnartz, F. Egidi, S. Kendir, and M. Wessling. “Flow-electrode capacitive deionization enables continuous and energy-efficient brine concentration”. *Desalination* 490 (2020). DOI: 10.1016/j.desal.2020.114453 (cit. on pp. 25, 31, 59).

[Romm2021] A. Rommerskirchen, H. Roth, C. J. Linnartz, F. Egidi, C. Kneppeck, F. Roghmans, and M. Wessling. “Mitigating Water Crossover by Crosslinked Coating of Cation-Exchange Membranes for Brine Concentration”. *Adv. Mat. Technol.* 6.10 (2021). DOI: 10.1002/admt.202100202 (cit. on p. 63).

[Sata2000] T. Sata. “Studies on anion exchange membranes having permselectivity for specific anions in electrodialysis — effect of hydrophilicity of anion exchange membranes on permselectivity of anions”. *J. Membr. Sci.* 167.1 (2000). DOI: 10.1016/S0376-7388(99)00277-X (cit. on p. 19).

[Sata2002] T. Sata, T. Sata, and W. Yang. “Studies on cation-exchange membranes having permselectivity between cations in electrodialysis”. *J. Membr. Sci.* 206.1 (2002). DOI: 10.1016/S0376-7388(01)00491-4 (cit. on p. 19).

[Scha1998] J. Schaep, B. Van der Bruggen, C. Vandecasteele, and D. Wilms. “Influence of ion size and charge in nanofiltration”. *Sep. Purif. Technol.* 14.1 (1998). DOI: 10.1016/S1383-5866(98)00070-7 (cit. on p. 14).

[Schm2012] V. M. Schmidt. *Elektrochemische Verfahrenstechnik: Grundlagen, Reaktionstechnik, Prozessoptimierung*. John Wiley & Sons, 2012 (cit. on pp. 35, 36).

[Schu2019] M. S. Schuler, M. Cañedo-Argüelles, W. D. Hintz, B. Dyack, S. Birk, and R. A. Relyea. “Regulations are needed to protect freshwater ecosystems from salinization”. *Philos. Trans. R. Soc. Lond., B, Biol. Sci.* 374.1764 (2019). DOI: 10.1098/rstb.2018.0019 (cit. on p. 1).

[Schw2018] R. Schwantes, K. Chavan, D. Winter, C. Felsmann, and J. Pfafferott. “Techno-economic comparison of membrane distillation and MVC in a zero liquid discharge application”. *Desalination* 428 (2018). DOI: 10.1016/j.desal.2017.11.026 (cit. on p. 11).

[Shan2008] M. A. Shannon, P. W. Bohn, M. Elimelech, J. G. Georgiadis, B. J. Marin, and A. M. Mayes. “Science and technology for water purification in the coming decades”. *Nature* 452 (March 2008). DOI: 10.1038/nature06599 (cit. on p. 1).

[Shi2023] C. Shi, H. Wang, A. Li, G. Zhu, X. Zhao, and F. Wu. “Process model for flow-electrode capacitive deionization for energy consumption estimation and system optimization”. *Water Res.* 230 (2023). DOI: 10.1016/j.watres.2022.119517 (cit. on p. 22).

[Shik2000] I. A. Shiklomanov. “Appraisal and Assessment of World Water Resources”. *Water Int.* 25.1 (2000). DOI: 10.1080/02508060008686794 (cit. on p. 1).

[Shoc2022] A. N. Shocron, R. S. Roth, E. N. Guyes, R. Epsztein, and M. E. Suss. “Comparison of Ion Selectivity in Electrodialysis and Capacitive Deionization”. *Environ. Sci. Technol. Lett.* 9.11 (2022). DOI: 10.1021/acs.estlett.2c00551 (cit. on p. 2).

[Silv2007] M. J. D. Silva, E. Schleicher, and U. Hampel. “Capacitance wire-mesh sensor for fast measurement of phase fraction distributions”. *Meas. Sci. Technol.* 18.7 (2007). DOI: 10.1088/0957-0233/18/7/059 (cit. on p. 41).

[Sing2019] K. Singh, S. Porada, H. de Gier, P. Biesheuvel, and L. de Smet. “Timeline on the application of intercalation materials in Capacitive Deionization”. *Desalination* 455 (2019). DOI: 10.1016/j.desal.2018.12.015 (cit. on p. 27).

[Smal2013] H. Small. *Ion chromatography*. Springer Science & Business Media, 2013 (cit. on p. 35).

[Smit2009] V. H. Smith and D. W. Schindler. “Eutrophication science: where do we go from here?” *Trends Ecol. Evol.* 24.4 (2009). DOI: 10.1016/j.tree.2008.11.009 (cit. on p. 2).

[Stra1995] H. Strathmann. “Chapter 6 Electrodialysis and related processes”. In *Membrane Separations Technology - Principles and Applications*. Vol. 2. Membrane Science and Technology. Elsevier, 1995. Pp. 213–281. (Cit. on pp. 17, 18).

[Stra2004] H. Strathmann. *Ion-exchange membrane separation processes*. Vol. 9. Membrane science and technology series. Amsterdam: Elsevier, 2004 (cit. on pp. 15, 16, 19, 30, 120).

[Sun2021] B. Sun, M. Zhang, S. Huang, J. Wang, and X. Zhang. "Limiting concentration during batch electrodialysis process for concentrating high salinity solutions: A theoretical and experimental study". *Desalination* 498 (2021). DOI: 10.1016/j.desal.2020.114793 (cit. on p. 110).

[Sun2022] B. Sun, M. Zhang, S. Huang, Z. Cao, L. Lu, and X. Zhang. "Study on mass transfer performance and membrane resistance in concentration of high salinity solutions by electrodialysis". *Sep. Purif. Technol.* 281 (2022). DOI: 10.1016/j.seppur.2021.119907 (cit. on pp. 15, 16).

[Sun2023] J. Sun, S. Garg, and T. D. Waite. "A Novel Integrated Flow-Electrode Capacitive Deionization and Flow Cathode System for Nitrate Removal and Ammonia Generation from Simulated Groundwater". *Environ. Sci. Technol.* 57.39 (2023). DOI: 10.1021/acs.est.3c03922 (cit. on p. 32).

[Suss2015] M. E. Suss, S. Porada, X. Sun, P. M. Biesheuvel, J. Yoon, and V. Presser. "Water desalination via capacitive deionization: what is it and what can we expect from it?" *Energy Environ. Sci.* 8.8 (2015). DOI: 10.1039/c5ee00519a (cit. on pp. 16, 32).

[Tang2019] K. Tang, S. Yiacoumi, Y. Li, and C. Tsouris. "Enhanced Water Desalination by Increasing the Electroconductivity of Carbon Powders for High-Performance Flow-Electrode Capacitive Deionization". *ACS Sustain. Chem. Eng.* 7.1 (2019). DOI: 10.1021/acssuschemeng.8b04746 (cit. on p. 27).

[Tang2020] K. Tang, S. Yiacoumi, Y. Li, J. Gabitto, and C. Tsouris. "Optimal conditions for efficient flow-electrode capacitive deionization". *Sep. Purif. Technol.* 240 (2020). DOI: 10.1016/j.seppur.2020.116626 (cit. on p. 80).

[Tong2016] T. Tong and M. Elimelech. "The Global Rise of Zero Liquid Discharge for Wastewater Management: Drivers, Technologies, and Future Directions". *Environ. Sci. Technol.* 50 (13 July 2016). DOI: 10.1021/acs.est.6b01000 (cit. on pp. 11, 13, 17).

[van 2021] P. H. van Langevelde, I. Katsounaros, and M. T. Koper. “Electrocatalytic Nitrate Reduction for Sustainable Ammonia Production”. *Joule* 5.2 (2021). DOI: 10.1016/j.joule.2020.12.025 (cit. on p. 2).

[Vela2015] H. Velasco Peña and O. Rodriguez. “Applications of wire-mesh sensors in multiphase flows”. *Flow Meas. Instrum.* 45 (2015). DOI: 10.1016/j.flowmeasinst.2015.06.024 (cit. on pp. 40, 41, 121, 122).

[Wang2011] H. Wang and L. Pilon. “Accurate Simulations of Electric Double Layer Capacitance of Ultramicroelectrodes”. *J. Phys. Chem. C* 115.33 (2011). DOI: 10.1021/jp204498e (cit. on p. 20).

[Wang2013] W. Wang, Q. Luo, B. Li, X. Wei, L. Li, and Z. Yang. “Recent Progress in Redox Flow Battery Research and Development”. *Adv. Funct. Mater.* 23.8 (2013). DOI: 10.1002/adfm.201200694 (cit. on p. 26).

[Wang2020] L. Wang, C. Zhang, C. He, T. D. Waite, and S. Lin. “Equivalent film-electrode model for flow-electrode capacitive deionization: Experimental validation and performance analysis”. *Water Res.* 181 (2020). DOI: 10.1016/j.watres.2020.115917 (cit. on p. 121).

[Wang2021a] S. Wang, J. Zhang, O. Gharbi, V. Vivier, M. Gao, and M. E. Orazem. “Electrochemical impedance spectroscopy”. *Nat. Rev. Methods Primers* 1.1 (2021). DOI: 10.1038/s43586-021-00039-w (cit. on p. 37).

[Wang2021b] Z. Wang, Y. Hu, Q. Wei, W. Li, X. Liu, and F. Chen. “Enhanced Desalination Performance of a Flow-Electrode Capacitive Deionization System by Adding Vanadium Redox Couples and Carbon Nanotubes”. *J. Phys. Chem. C* 125.2 (2021). DOI: 10.1021/acs.jpcc.0c09058 (cit. on p. 27).

[Wang2022] J. Wang, Z. Shi, J. Fang, B. Chu, N. Li, L. Shui, G. Wang, and F. Chen. “The optimized flow-electrode capacitive deionization (FCDI) performance by ZIF-8 derived nanoporous carbon polyhedron”. *Sep. Purif. Technol.* 281 (2022). DOI: 10.1016/j.seppur.2021.119345 (cit. on p. 27).

[Welg2005] T. Welgemoed and C. Schutte. “Capacitive Deionization Technology™: An alternative desalination solution”. *Desalination* 183.1 (2005). DOI: 10.1016/j.desal.2005.02.054 (cit. on p. 22).

[Wing1953] A. G. Winger, G. W. Bodamer, and R. Kunin. “Some electrochemical properties of new synthetic ion exchange membranes”. *J. Electrochem. Soc.* 100.4 (1953). DOI: 10.1149/1.2781103 (cit. on p. 18).

[Xing2020] W. Xing, J. Liang, W. Tang, D. He, M. Yan, X. Wang, Y. Luo, N. Tang, and M. Huang. “Versatile applications of capacitive deionization (CDI)-based technologies”. *Desalination* 482 (2020). DOI: 10.1016/j.desal.2020.114390 (cit. on pp. 16, 22).

[Xu2002] T. Xu. “Electrodialysis processes with bipolar membranes (EDBM) in environmental protection—a review”. *Resour. Conserv. Recycl.* 37.1 (2002). DOI: 10.1016/S0921-3449(02)00032-0 (cit. on p. 2).

[Xu2005] T. Xu. “Ion exchange membranes: State of their development and perspective”. *J. Membr. Sci.* 263.1 (2005). DOI: 10.1016/j.memsci.2005.05.002 (cit. on p. 18).

[Xu2017] X. Xu, M. Wang, Y. Liu, T. Lu, and L. Pan. “Ultrahigh Desalinization Performance of Asymmetric Flow-Electrode Capacitive Deionization Device with an Improved Operation Voltage of 1.8 V”. *ACS Sustain. Chem. Eng.* 5.1 (2017). DOI: 10.1021/acssuschemeng.6b01212 (cit. on pp. 27, 80).

[Xu2020] D. Xu, W. Wang, M. Zhu, and C. Li. “Recent Advances in Desalination Battery: An Initial Review”. *ACS Appl. Mater. Interfaces.* 12.52 (2020). DOI: 10.1021/acsami.0c15413 (cit. on p. 27).

[Xu2021a] L. Xu, Y. Mao, Y. Zong, S. Peng, X. Zhang, and D. Wu. “Membrane-Current Collector-Based Flow-Electrode Capacitive Deionization System: A Novel Stack Configuration for Scale-Up Desalination”. *Environ. Sci. Technol.* 55 (19 Oct. 2021). DOI: 10.1021/acs.est.1c03829 (cit. on pp. 30, 44).

[Xu2021b] L. Xu, Y. Mao, Y. Zong, and D. Wu. “Scale-up desalination: Membrane-current collector assembly in flow-electrode capacitive deionization system”. *Water Res.* 190 (2021). DOI: 10.1016/j.watres.2020.116782 (cit. on pp. 30, 44).

[Xu2021c] Y. Xu, F. Duan, Y. Li, H. Cao, J. Chang, H. Pang, and J. Chen. “Enhanced desalination performance in asymmetric flow electrode capacitive deionization with nickel hexacyanoferrate and activated carbon electrodes”. *Desalination* 514 (2021). DOI: 10.1016/j.desal.2021.115172 (cit. on p. 27).

[Yan2019] H. Yan, Y. Wang, L. Wu, M. A. Shehzad, C. Jiang, R. Fu, Z. Liu, and T. Xu. “Multistage-batch electrodialysis to concentrate high-salinity solutions: Process optimisation, water transport, and energy consumption”. *J. Membr. Sci.* 570-571 (2019). DOI: 10.1016/j.memsci.2018.10.008 (cit. on p. 16).

[Yan2023] L. Yan, S. Issaka Alhassan, H. Gang, B. Wu, D. Wei, Y. Cao, P. Chen, and H. Wang. “Enhancing charge transfer utilizing ternary composite slurry for high-efficient flow-electrode capacitive deionization”. *Chem. Eng. J.* 468 (2023). DOI: 10.1016/j.cej.2023.143413 (cit. on p. 27).

[Yang2016] S. Yang, S.-i. Jeon, H. Kim, J. Choi, J.-g. Yeo, H.-r. Park, and D. K. Kim. “Stack Design and Operation for Scaling Up the Capacity of Flow-Electrode Capacitive Deionization Technology”. *ACS Sustain. Chem. Eng.* 4.8 (2016). DOI: 10.1021/acssuschemeng.6b00689 (cit. on p. 44).

[Yang2017] S. Yang, H.-r. Park, J. Yoo, H. Kim, J. Choi, M. H. Han, and D. K. Kim. “Plate-shaped graphite for improved performance of flow-electrode capacitive deionization”. *J. Electrochem. Soc.* 164.13 (2017). DOI: 10.1149/2.1551713jes (cit. on p. 27).

[Zago2007] A. A. Zagorodni. *Ion Exchange Materials - Properties and Applications*. Elsevier BV, 2007 (cit. on p. 17).

[Zhan2017] W. Zhang, M. Miao, J. Pan, A. Sotto, J. Shen, C. Gao, and B. V. der Bruggen. “Separation of divalent ions from seawater concentrate to enhance the purity of coarse salt by electrodialysis with monovalent-selective membranes”. *Desalination* 411 (2017). DOI: 10.1016/j.desal.2017.02.008 (cit. on p. 16).

[Zhan2020a] J. Zhang, L. Tang, W. Tang, Y. Zhong, K. Luo, M. Duan, W. Xing, and J. Liang. “Removal and recovery of phosphorus from low-strength wastewaters by flow-electrode capacitive deionization”.

Sep. Purif. Technol. 237 (2020). DOI: 10.1016/j.seppur.2019.116322 (cit. on p. 32).

[Zhan2020b] X. Zhang, F. Yang, J. Ma, and P. Liang. “Effective removal and selective capture of copper from salty solution in flow electrode capacitive deionization”. *Environ. Sci.: Water Res. Technol.* 6 (2 2020). DOI: 10.1039/C9EW00467J (cit. on p. 32).

[Zhan2021] C. Zhang, J. Ma, L. Wu, J. Sun, L. Wang, T. Li, and T. D. Waite. “Flow Electrode Capacitive Deionization (FCDI): Recent Developments, Environmental Applications, and Future Perspectives”. *Environ. Sci. Technol.* 55 (8 Apr. 2021). DOI: 10.1021/acs.est.0c06552 (cit. on pp. 3, 5, 25, 27, 29, 44, 54, 60).

[Zhan2022a] X. Zhang, H. Zhou, Z. He, H. Zhang, and H. Zhao. “Flow-electrode capacitive deionization utilizing three-dimensional foam current collector for real seawater desalination”. *Water Res.* 220 (2022). DOI: 10.1016/j.watres.2022.118642 (cit. on p. 29).

[Zhan2022b] X. Zhang, J. Zhou, H. Zhou, H. Zhang, and H. Zhao. “Enhanced Desalination Performance by a Novel Archimedes Spiral Flow Channel for Flow-Electrode Capacitive Deionization”. *ACS EST Engg.* 2.7 (2022). DOI: 10.1021/acsestengg.1c00445 (cit. on pp. 108, 110).

[Zhan2023] W. Zhang, W. Xue, K. Xiao, C. Visvanathan, J. Tang, and L. Li. “Selection and optimization of carbon-based electrode materials for flow-electrode capacitive deionization”. *Sep. Purif. Technol.* 315 (2023). DOI: 10.1016/j.seppur.2023.123649 (cit. on p. 27).

[Zhan2024] X. Zhang, M. Pang, Y. Wei, F. Liu, H. Zhang, and H. Zhou. “Three-dimensional titanium mesh-based flow electrode capacitive deionization for salt separation and enrichment in high salinity water”. *Water Res.* 251 (2024). DOI: 10.1016/j.watres.2024.121147 (cit. on p. 29).

[Zhao2012] R. Zhao, P. Biesheuvel, and A. Van der Wal. “Energy consumption and constant current operation in membrane capacitive deionization”. *Energy Environ. Sci.* 5.11 (2012). DOI: 10.1039/C2EE21737F (cit. on p. 23).

[Zhu2021] P. Zhu, D. Gastol, J. Marshall, R. Sommerville, V. Goodship, and E. Kendrick. “A review of current collectors for lithium-ion batteries”. *J. Power Sources* 485 (2021). DOI: 10.1016/j.jpowsour.2020.229321 (cit. on p. 28).

[Zour2015] Z. Zourmand, F. Faridirad, N. Kasiri, and T. Mohammadi. “Mass transfer modeling of desalination through an electrodialysis cell”. *Desalination* 359 (2015). DOI: 10.1016/j.desal.2014.12.008 (cit. on p. 120).